

---


Electronic Theses and Dissertations, 2004-2019

---

2016

## Sensing using Specialty Optical Fibers

Amy Van Newkirk  
*University of Central Florida*

 Part of the [Electromagnetics and Photonics Commons](#), and the [Optics Commons](#)  
Find similar works at: <https://stars.library.ucf.edu/etd>  
University of Central Florida Libraries <http://library.ucf.edu>

This Doctoral Dissertation (Open Access) is brought to you for free and open access by STARS. It has been accepted for inclusion in Electronic Theses and Dissertations, 2004-2019 by an authorized administrator of STARS. For more information, please contact [STARS@ucf.edu](mailto:STARS@ucf.edu).

---

### STARS Citation

Van Newkirk, Amy, "Sensing using Specialty Optical Fibers" (2016). *Electronic Theses and Dissertations, 2004-2019*. 5095.  
<https://stars.library.ucf.edu/etd/5095>

# SENSING WITH SPECIALTY OPTICAL FIBERS

by

AMY VAN NEWKIRK  
B.S. Grove City College, 2011  
M.S. University of Central Florida, 2014

A dissertation submitted in partial fulfillment of the requirements  
for the degree of Doctor of Philosophy in Optics  
in CREOL, The College of Optics and Photonics  
at the University of Central Florida  
Orlando, Florida

Summer Term  
2016

Major Professor: Axel Schülzgen

© 2016 Amy Van Newkirk

## **ABSTRACT**

Initially, optical fiber was created as a simple means of transporting information via light for telecommunications. As fiber technology and fabrication methods advanced, alternative applications emerged. Specialty optical fibers, meaning fibers with complex designs and capabilities beyond the simple transmission of light, have many diverse applications. These include lasers, medicine, imaging, nonlinear optics, and more. One of the fastest growing fields for specialty optical fibers is sensing. Fiber optic devices have many benefits over other sensing devices and have been shown to be capable of measuring temperature, strain, bending, pressure, current, refractive index, vibration, rotation, and more. There are currently many fiber designs and devices being explored for various applications in sensing, and several of them are investigated here.

The following is a thesis covering work performed on sensing using specialty optical fibers. The majority of the following results are focused specifically on coupled multicore fibers and their use in multimode interference devices. An introduction to hollow core fibers, their design and characterization, and their potential use in sensing is also included.

Chapter 1 is an introduction to fiber sensing. This chapter includes a very concise introduction to the basic principles of optical fiber guidance, an introduction to the history of optical fiber, the benefits of optical fiber based sensors over other methods, and different types of optical fiber sensors. Additionally, a review of the specific multimode interference based fiber sensor configuration used throughout this dissertation is presented at the end of this chapter. While not exhaustive in its explanation of optical fibers or fiber sensing, this chapter is intended

to be an overview of the subject and give the reader a broad view of the field, into which they can place the following work.

Chapter 2 consists of the bulk of the research performed to date on multicore fiber sensors. This includes the theory of operation and the optimization of the multicore fiber for use in sensing applications. This chapter also contains results from many sensing experiments, including temperature, strain, and bending measurements. Additionally a new fiber design for pressure and acoustic measurements is proposed and initial results are shown. The research performed on multicore fiber has been extensive and makes up the majority of this thesis.

Chapter 3 covers work that has been done on anti-resonant hollow core fibers. This includes an introduction to their operation principal, a potential application in gas sensing, design dependent loss measurements, as well as analysis of the core mode content of fibers that have been fabricated in CREOL. This work is more introductory, but has great potential to be useful in many applications, including fiber sensing.

Chapter 4 is the conclusion of the dissertation, summarizing everything presented thus far. Additionally an outlook on possible future directions for this work is given.

This dissertation contains a comprehensive study of multicore fiber for use in sensing applications, as well as an introduction to several new fiber designs, including hollow core fiber, and their applications. However, other work has been performed on a variety of topics within the field of specialty optical fibers, which is not detailed in this dissertation. For instance, research was done in a partnership between CREOL, Aerospace Engineering at UCF, and the Boeing Company. In this project, research was performed on implementing photo-luminescent alpha

alumina nanoparticles into coatings to be dispersed onto structures to measure strain with high spatial resolution, while fiber Bragg gratings were being used to calibrate the sensitivity. Also, work was done in collaboration with Q-Peak, Inc. on designing a fused fiber wavelength division multiplexer using large mode area fiber for high power laser applications. Another project that I contributed to was developing a high power single frequency fiber laser using highly-doped phosphate glass fiber and femtosecond written gratings.

Included at the end of this dissertation is a full list of my personal journal and conference publications.

## ACKNOWLEDGMENTS

Firstly, I would like to thank Dr. Axel Schülzgen, my PhD advisor. He has lead me through my time as a graduate student and taught me everything I needed to know in order to obtain this degree. With just the right balance of guidance and independence, Axel has steered my research in the right direction, while allowing me to figure things out on my own. This has enabled me to become self-motivated and allowed me to explore the areas of research that interested me. I would not have gotten so far in my research without Axel as an advisor.

Secondly, I would like to thank Dr. Rodrigo Amezcua Correa for not only being a member of my committee, but also for all of the collaboration throughout my time at CREOL. None of my research would have been possible without Rodrigo and his group and the fibers that they were able to fabricate. Rodrigo was also a helpful voice in discussions of my results and possible publications.

I would also like to thank Dr. Peter Delfyett. While not directly involved in my research, he has had an integral role in my career as a PhD student. He has been my professor, recommender, and committee member over the last years, and has been an overall positive influence on my time in CREOL.

Additionally, I would like to thank Dr. Seetha Raghavan. She has been a part of my research since the very beginning, while collaborating on my first sensor project. While serving on my committee, she has been an important outside voice on my work.

I would also like to thank a few of my other colleagues from CREOL. Namely, Enrique Antonio Lopez, who has not only fabricated every single fiber that I've needed for my research,

but has also taught me about fiber fabrication and allowed me to be a part of the process. Additionally, I would like to thank past FOL group members, Dr. Peter Hofmann and Dr. Clemence Jollivet, as well as current group members, Jim Anderson, Naman Mehta, and Burdley Colas, for providing a great environment to work in.

Finally, I would like to thank my friends and family. The friends that I've made in my time at CREOL have made graduate school a more enjoyable experience than I thought possible. Having friends within CREOL who understood everything I was going through, as well as friends outside of CREOL who were able to give me a break from optics, enabled me to get through this PhD program. I'd also like to thank my family who have always supported me, despite not completely understanding what I was doing. My mom, my dad, and my brother have all made it clear that they were proud of me, at that continually motivated me try my hardest and do as well as I possibly could.



## TABLE OF CONTENTS

LIST OF FIGURES .....	x
LIST OF TABLES .....	xvi
LIST OF ACRONYMS .....	xvii
CHAPTER 1: OPTICAL FIBER SENSING .....	1
Basic Principals of Optical Fiber Guidance .....	1
Brief History of Optical Fiber .....	2
Benefits of Optical Fiber Sensing .....	3
Types of Optical Fiber Sensors .....	4
SMS Sensor Review .....	6
CHAPTER 2: MULTICORE FIBERS FOR SENSING.....	8
Supermode Interference of Multicore Fiber.....	8
Multicore Fiber Design .....	10
Sensitivity Measurements .....	22
Temperature.....	22
Strain.....	27
Bending.....	36
Photonic Lantern Experiment .....	37
Direction-Sensitive Measurement with known Orientation .....	47
Summary.....	51
Air Hole Multicore Fiber.....	52
Design.....	52
Sensor Fabrication .....	54
Sensitivity Measurements.....	58
Bending .....	58
Temperature .....	60
Strain .....	61
Pressure .....	62
Summary and Outlook .....	67
CHAPTER 3: HOLLOW CORE FIBER.....	70

Sensing with Hollow Core Fiber .....	70
Loss in Hollow Core Fibers .....	76
Mode Analysis of Hollow Core Fiber .....	82
Summary and Outlook .....	95
CHAPTER 4: CONCLUSION .....	97
APPENDIX: PUBLICATIONS.....	100
Journal Publications .....	101
Conference Presentations .....	101
REFERENCES .....	104

## LIST OF FIGURES

Figure 1. Facet images of a seven and 19 core fiber and a sample of their simulated modes. ....	11
Figure 2. Simulated SMS device, showing MMI in a seven core fiber. ....	12
Figure 3. Transmission spectrum of a seven core fiber SMS device, showing interference of two supermodes. ....	13
Figure 4. Simulated transmission spectra of TE polarized light and TM polarized light for a (a) three core MCF and a (b) seven core MCF.....	14
Figure 5. Measured refractive index profile of a seven core MCF. ....	15
Figure 6. MCF refractive index values measured with a Cauchy fit. ....	15
Figure 7. Simulated and measured transmission spectra of SMS devices with (a) seven and (b) 19 core fiber. ....	16
Figure 8. Comparison of transmission spectrum and excited mode power for a seven core device in simulation.....	17
Figure 9. Facet images of the two tested seven core fibers (a) and (b), and (c) their respected transmission spectra. ....	19
Figure 10. Maximum transmission for various excited mode powers from simulation. ....	20
Figure 11. Transmission spectra of five individual sensors and a single multiplexed chain.....	20
Figure 12. Simulated transmission spectrum of 17 MCF sensors with 2 cm lengths in a single fiber chain. ....	21
Figure 13. Transmission spectra of a 2 cm MCF sensor measured in a high temperature oven up to 1000°C [63]. ....	24

Figure 14. Sensor wavelength shift of seven core fiber device in a high temperature oven. ....	25
Figure 15. Measured wavelength shift and corresponding calculated thermo-optic coefficient. .	26
Figure 16. Wavelength shift measured from an applied strain on a MCF sensor.....	28
Figure 17. Experimental setup for measuring strain sensitivity and comparing MCF and FBG sensors.....	29
Figure 18. Example wavelength shifts caused by applied longitudinal force for a MCF sensor (a) and an FBG (b).....	30
Figure 19. Example wavelength shift of three sensors in a chain.....	31
Figure 20. Summary of all measured sensitivities for MCF and FBG devices as a function of OD. ....	31
Figure 21. Transmission spectra of two MCF devices separate (a) and spliced in a chain (b).....	33
Figure 22. Response of sensor chain to applied longitudinal force. ....	34
Figure 23. Response of sensor chain to applied force and temperature.....	35
Figure 24. Transmission spectra shift of two MCF sensors as a function of bending radius [72]. ....	36
Figure 25. Schematic showing the basic device structure of a photonic lantern [79]. ....	38
Figure 26. Experimental setup for bending test with a PL, showing the MCF cross section as well as the arrangement of SMF in the lantern. ....	40
Figure 27. Simulated modes of each fiber in the bending experiment: SMF, MCF, FMF, GIFs of varying core size, respectively. ....	41

Figure 28. Transmission spectra of the LP11a mode when bent in two directions with a radius of 23 cm, with spectral smoothing applied during the post processing. (a) A nine-point Savitzky–Golay smoothing filter was used showing the multimode interference occurring within the FMF, and (b) with a 65 point filter, more clearly showing the total power difference. ....	42
Figure 29. Relative power shifts of each of the FMF modes measured as a function of the inverse radius of curvature for four different bending directions.....	43
Figure 30. Simulated relative power shifts of all six FMF modes for bending in two directions.	45
Figure 31. Model of six channel mode-selective PL, showing the cross-section of the six core fiber, and the tapered device. ....	46
Figure 32. Simulated modes of a six mode PL in FimmWave. ....	46
Figure 33. Orientation of three core fiber used in simulation.....	48
Figure 34. Transmission spectra of a three core fiber sensor being bent in the (a) y direction and (b) x direction.....	48
Figure 35. Wavelength shift measured for a three core fiber in the y direction [81].....	50
Figure 36. Design of MCF with 15 air holes and (b) its corresponding transmission spectrum from an SMS device.....	53
Figure 37. Cross-sections of drawn air hole MCF of (a) band one and (b) band four.....	54
Figure 38. Images of SMF and air hole MCF before and after splicing with SMF-SMF program of an arc fusion splicer. ....	54
Figure 39. Images of SMF to air hole MCF splices from a CO2 laser splicer after optimization.	55

Figure 40. Cross-section of new air hole MCF model and (b) transmission spectrum of the SMS device for a typical MCF length. ....	56
Figure 41. Example spectra of SMS devices made with band three of the air hole MCF. ....	57
Figure 42. Transmission spectra of an air hole MCF device as it is bent, (a) unsmoothed and (b) smoothed. ....	59
Figure 43. Transmission spectra of (a) solid MCF and (b) air hole MCF devices as they are bent to a radius of 85 cm. ....	59
Figure 44. Air hole MCF sensor response to temperature for two different trials. ....	60
Figure 45. Smoothed transmission spectra of an air hole MCF sensor as strain is applied. ....	61
Figure 46. Measured wavelength shift of an air hole MCF sensor and an FBG. ....	62
Figure 47. Experimental setup for measuring sensitivity of MCF to acoustic waves. ....	63
Figure 48. ESA signal of solid MCF response to acoustic waves tuned from 10-90 kHz. ....	64
Figure 49. Transmission spectra of 10 cm air hole MCF sensor measured flat on the table (a), and in the acoustic mount (b). ....	65
Figure 50. Amplitude signal from the air hole MCF on an oscilloscope when excited by a 14 kHz wave. ....	66
Figure 51. Facet image and transmission spectrum of 18 cm of commercial HCF NKT 580. ....	71
Figure 52. SEM image of a non-touching ring HCF, draw 347, band 2. ....	73
Figure 53. Transmission spectrum of non-touching ring HCF, draw 347, band 2. ....	74
Figure 54. The COMSOL HCF design for Mesa (a) and its loss spectrum (b). ....	75
Figure 55. SEM image of an eight ring, closed boundary ARHCF. ....	78

Figure 56. (a) Transmission spectra of various lengths of the eight ring, closed boundary core ARHCF, (b) calculated loss from the cutback measurement.....	78
Figure 57. (a) SEM image of an eight ring, open boundary core ARHCF, (b) transmission spectra of various lengths, and (c) calculated loss from the cutback measurement.....	79
Figure 58. (a) SEM image of the seven ring, open boundary core ARHCF, (b) transmission spectra of various lengths, and (c), calculated loss form the cutback measurement. ....	80
Figure 59. (a) Design of a nested ARHCF [86], (b) SEM image of a drawn nested ARHCF, (c) transmission spectra measured for various lengths, and (d) the calculated loss from the cutback measurement. ....	81
Figure 60. (a) Transmitted white light spectrum of 4 m of non-touching ring HCF with an SEM facet image. (b) Simulated loss spectrum from COMSOL with the fiber design inset. ....	84
Figure 61. Experimental setup used for $S^2$ measurement. An example near field of the non-touching ring ARHCF is shown above the CCD and an example transmitted light spectrum with multimode interference is shown next to the OSA. ....	85
Figure 62. Fourier spectra of straight and bent non-touching ring HCF, with mode images above the corresponding peaks.....	87
Figure 63. Fourier spectra of two lengths of non-touching ring HCF. (inset) Loss cut back measurements.....	88
Figure 64. Transmitted white light spectrum of 4m of the touching ring HCF. (inset) SEM image of fiber facet.....	90

Figure 65. Fourier spectra of straight and bent touching ring HCF, with mode image above the corresponding peak. (inset) Power in LP11 as a function of bending diameter. ....	91
Figure 66. Fourier spectra of two lengths of touching ring HCF. (inset) Loss cut back measurements.....	92
Figure 67. Comparison of Fourier spectra before and after zeropadding was implemented.....	94



## **LIST OF TABLES**

Table 1. List of gases and their detection wavelengths for Mesa's Raman air sensor. ....	72
--	----

## **LIST OF ACRONYMS**

ARHCF: Anti-Resonant Hollow Core Fiber  
BBS: Broadband Source  
BS: Beam Splitter  
CCD: Charge Coupled Device  
CF: Collection Fiber  
ESA: Electrical Spectrum Analyzer  
FBG: Fiber Bragg grating  
FDM: Finite Difference Method  
FMF: Few Mode Fiber  
GDD: Group Delay Difference  
GIF: Graded Index Fiber  
HCF: Hollow Core Fiber  
HOM: Higher Order Mode  
IS: Integrating Sphere  
L: Lens  
LP: Linearly Polarized  
MCF: Multicore Fiber  
MCVD: Modified Chemical Vapor Deposition  
MFD: Mode Field Diameter  
MMF: Multimode Fiber  
MMI: Multimode Interference  
MO: Microscope Objective  
OBR: Optical Backscatter Reflectometer  
OD: Outer Diameter  
OSA: Optical Spectrum Analyzer  
PCF: Photonic Crystal Fiber  
PL: Photonic Lantern

S<sup>2</sup>: Spatially and Spectrally Resolved

SEM: Scanning Electron Microscope

SLD: Superluminescent Diode

SMF: Single Mode Fiber

SMS: Single mode-Multimode-Single mode

# CHAPTER 1: OPTICAL FIBER SENSING

## Basic Principles of Optical Fiber Guidance

Standard optical fibers guide light on the principle of total internal reflection. A basic optical fiber has a core and a cladding. The core has a slightly higher refractive index,  $n$ , than the cladding, and the ratio of the two indices determines the angle at which light within the core becomes totally internally reflected at the core/cladding boundary and does not transmit into the cladding. This angle is known as the critical angle ( $\theta_c$ ).

$$\sin(\theta_c) = \frac{n_{cladding}}{n_{core}} \quad (1)$$

The totally internally reflected light will then propagate down the core of the fiber. The way that the light is guided within the core, the shape of the light's intensity profile, is referred to as a mode. The modes of a fiber are finite and are determined by the core and cladding refractive indices, the core size, the shape of the refractive index profile, and the wavelength of light. The solutions for the wave equation in optical fiber take the form of Bessel functions. The Bessel functions can then be used to calculate the number of modes that a given fiber will support. The normalized frequency, or V-number, can be used to determine the number of modes that a fiber can guide. For a step-index fiber:

$$V = \frac{2\pi}{\lambda} a \sqrt{n_{core}^2 - n_{cladding}^2} \quad (2)$$

Here  $V$  is the normalized frequency,  $\lambda$  is the wavelength of light, and  $a$  is the radius of the core. When  $V < 2.405$ , only the fundamental mode can be guided, and the fiber is referred to as

single mode. For any value of  $V$  larger than 2.405, multiple modes can be guided and propagate along the fiber together. For multimode fibers that support many modes, the  $V$ -number is approximately equal to the number of guided modes. Therefore, optical fibers can be explicitly designed to support a specified number of modes at a given wavelength by varying the core size and the refractive index of the core and cladding.

While most of the fibers discussed throughout this dissertation are not simple step index fibers, many of these basic guiding principles still apply. For fibers that do not guide according to total internal reflection, a separate introduction will be given.

### Brief History of Optical Fiber

Glass optical fiber was first presented as a potential waveguide for communication by Kao et al. in 1966 [1]. They explored many of the properties of optical fiber, including supported modes, potential losses, power handling, fabrication processes, etc., both in theory and in experiment. While the guidance properties of fiber seemed extremely promising, the main limitation was the high loss of the currently available material. A few years later, Kapron, et al. were able to achieve fiber propagation losses as low as 20 dB/km, making optical fiber a viable technology for many applications [2]. Within 10 years, optical fiber quickly progressed to have losses of only 1 dB/km, 1 GHz bandwidths, tensile strength in the hundreds of kpsi, kilometer lengths, as well as the ability to be spliced, connectorized, and cabled [3].

Since their initial invention, optical fibers have expanded into an ever-growing field of various designs and applications. From the traditional step index single mode fiber (SMF), fibers

have advanced to multimode, few mode, graded index [4], photonic crystal [5], large pitch [6], and hollow core designs [7]. Additionally, with developments in fabrication techniques, such as modified chemical vapor deposition (MCVD) [8], doping the fibers with rare earth elements has enabled the creation of fiber amplifiers and lasers [9,10]. As well as fiber design and material advances, fiber devices have also been an expanding area of research. Fiber Bragg gratings (FBGs) [11], isolators [12], circulators [12], wavelength division multiplexers [13], pump combiners [14], couplers [15], and photonic lanterns [16] are just some of the fiber devices that have been developed for various applications.

Optical fiber and fiber devices have obviously been widely used for telecommunications, which was their initial application. However, they have found use in many other areas as well. One of these areas is medical applications, such as laser scalpels [17] and optical tweezers [18]. Another growing area of research for optical fiber and fiber devices is sensing [19], which is the focus of this dissertation.

### Benefits of Optical Fiber Sensing

Sensing environmental conditions from a remote location is important for industries such as aerospace, oil, civil engineering, etc. There are many obstacles that need to be overcome when sensing in certain extreme conditions; for instance, the ability to measure temperatures over 1000°C, or the need to inexpensively sense the strain in a structure thousands of meters long. There have been many developments in sensors that use resistive elements, i.e. strain gauges and thermocouples. However, these elements are susceptible to electromagnetic influence from the

environment. They are also relatively expensive when considering applications needing hundreds of sensors multiplexed for distributed measurements. Additionally, many current sensors require substantial operating costs and cannot be interrogated from remote distances.

Fiber optic devices for sensing offer solutions to all of these problems. High temperature sensing, low cost devices, multiplexing, long range interrogation, and independence from electromagnetic interference are all possible through new fiber optic technology. Additionally, optical fibers are compact and lightweight, enabling simple integration into existing structures. Many fiber optic devices can be used for sensing strain, temperature, pressure, curvature, liquid levels, etc. Some areas where fiber optic sensors are currently be used are airplane wings, wind turbines, bridges, pipelines, and oil wells.

### Types of Optical Fiber Sensors

There are many types of fiber optic sensors. Fiber Bragg gratings are very common and have been shown to be able to measure strain and temperature, as well as other measurands, with relative simplicity and high sensitivity [19–22]. FBGs are periodic modulations of the refractive index of the core of an optical fiber, generally written through illumination of ultraviolet light through a phase mask [23]. The periodic change in index causes a narrowband reflection at the wavelength satisfying the Bragg condition, which is dependent on the core index of refraction and the period of the modulation. Because the reflected wavelength is a function of the index and the period of modulation, it is sensitive to environmental changes and changes in fiber length. Tracking of the reflected wavelength is a fairly simple interrogation method, and many FBGs

can be multiplexed together for distributed measurement [24]. However, while fiber sensing has been dominated by FBGs, they suffer from degradation at temperatures above a few hundred degrees Celsius, limiting their applications. In order to increase this temperature limitation, FBGs written with femtosecond pulses [25], regenerated FBGs [26], and FBGs in Sapphire fiber [27] have all been developed. Many other optical fiber based sensors can have much higher damage threshold temperatures, allowing for a wider range of sensing applications. Both Rayleigh and Brillouin scattering have been successfully used to measure temperature, strain, and polarization [19,28–33]. Rayleigh scattering is the random scattering of light off of particles that are much smaller than the wavelength. This scattering can be tracked, and changes can be correlated to environmental effects. Brillouin scattering is similar, but here the effect is caused by the interaction of the optical photons with acoustic phonons, caused by the  $\chi^3$  nonlinearity of the material. Again, because of the dependence of this effect on the fiber's refractive index, it is sensitive to environmental changes. Both Rayleigh and Brillouin scattering based sensing have the benefit of being distributed measurements, leading to more information than point sensors, such as FBGs [34]. However, the measurement and characterization of these effects is much more complex and generally requires advanced computation. Interferometric fiber sensors are also relatively common for measuring many parameters in a variety of configurations [19,35–39]. One of the simplest interferometric sensing configurations is the Fabry-Perot resonator [40,41]. A Fabry-Perot cavity is created by two reflecting surfaces, which cause sharp resonances in transmission. These resonances are highly dependent on the distance between the two reflectors, and therefore on strain and pressure. Another type of interferometric fiber sensor



is based on the Sagnac effect [42,43]. This uses the interference of two beams that traverse the same optical path in opposite directions, and is mainly used in measuring orientation and current. In addition to these, many interferometric fiber sensors are based off of the multimode interference (MMI) in multimode fibers (MMF) or few mode fibers (FMF).

### SMS Sensor Review

Multimode interference in fibers is a promising avenue for many sensing needs. The first demonstration of sensing using MMI was in 1979 when Layton et al. showed that sound could be sensed by looking at the phase change between two interfering spatial core modes in a fiber [44]. MMI can also use the interference of core-cladding modes, as well as polarimetric modes [45]. The transmission characteristics of MMF spliced between two SMFs, known as SMS structures, were first investigated in 2003 [46]. Later that year, Mehta et al. showed for the first time that a displacement sensor could be formed with a single mode fiber-multimode fiber-mirror configuration [47]. In 2006, Li et al. demonstrated a temperature sensor working up to 800°C [48] using the interference of several higher order linearly polarized (LP) modes in a single mode fiber-multimode fiber-cleaved facet configuration. However, these configurations do not offer the possibility of multiplexing, due to their reflective design. A transmissive SMS structure can be multiplexed by simply splicing multiple devices together. Zhang et al. showed a transmissive refractive index sensor in 2010 using a SMS structure [49].

The previously mentioned SMS devices all used either no core or large core step index fiber as the fiber supporting multiple modes. However, it is also possible to use MMI for sensing

with graded index fiber [50], photonic crystal fiber [51], and multicore fiber (MCF) [52]. These special fiber designs lead to greater control over the modes that are interfering. Specifically, MCFs have shown great promise in sensing temperature [53], strain [54], and refractive index [55].

Unfortunately, the geometry of the aforementioned multicore devices is fairly complex, using suspended core fiber or etching of the fiber cladding. A simpler fiber design will increase the applicability of the sensors, primarily when high levels of multiplexing are needed. Also, using multiple cores instead of large cores or graded index cores allows for greater mode-matching to the SMF fiber. By designing the cores of the MCF to match the mode field of the fundamental mode from the SMF, very low splice losses can be achieved. This makes multiplexing many sensors into one fiber with low overall transmission loss possible.

## CHAPTER 2: MULTICORE FIBERS FOR SENSING

### Supermode Interference of Multicore Fiber

In a multicore fiber, modes involving multiple numbers of cores are called supermodes. Supermodes are the superposition of the individual LP modes of each of the cores, and are only supported by MCF with cores close enough together that the light can evanescently couple between them [56]. If more than one supermode is excited in a MCF, multimode interference, similar to that observed in MMF, will occur [57]. The origin and various characteristics of MMI in an SMS structure has been outlined by Kumar et al. [46]. Because each mode has a different propagation constant, a phase difference develops between them as they propagate down the MMF, as shown in Eqn. 3, where  $\phi$  is the phase difference,  $\beta$  is the propagation constant of each mode,  $m$  is the mode number, and  $L$  is the length of fiber.

$$\Delta\phi = (\beta_m - \beta_{m+1})L \quad (3)$$

This phase difference was then expanded by Kumar to be the following:

$$\Delta\phi = \frac{2\sqrt{2\Delta}}{a}L + \frac{4(m+1)\Delta}{\pi a^2 n}L\lambda \quad (4)$$

where  $\Delta$  is the refractive index difference of the core and cladding,  $a$  is the core radius, and  $n$  is the core refractive index of the MMF. This shows that the phase difference is linearly dependent on the wavelength, which shows that it will produce a periodic modulation of power in spectrum when the light from the MMF is coupled into a SMF. The periodicity of the modulation was also derived by Kumar to be:

$$\Delta\lambda_{2\pi} = \frac{\pi^2 a^2 n}{2\Delta L} \quad (5)$$

While the fiber investigated above was a standard MMF and not a MCF, the basic periodically wavelength dependent transmission spectrum they derived also applies to the MCF devices. However, while the MMI produced from supermodes is similar to that produced by standard MMF or FMF, MCFs have a distinct advantage over these fibers. The advantage is the large number of degrees of freedom one has when designing a MCF vs. a MMF. In a MMF, you only have the choice of core size, refractive index difference, and possibly the refractive index profile. In a MCF you can vary the number of cores, size of the cores, placement of the cores, index profiles of the cores, and the pitch of the cores, in order to achieve the desired supermodes. This allows for much greater control over the coupling from an excitation fiber to the MCF, as well as control over which supermodes and how many supermodes propagate along the MCF, as will be shown in the following section.

Assuming each core only supports the fundamental  $LP_{01}$  mode, the multi-supermode interference created in the MCF is stable and predictable, unlike other MMFs which can support thousands of modes. Also, the cores and the corresponding supermodes of the MCF can be mode matched to SMF, resulting in very low loss coupling between the two fibers. This makes it attractive for sensor devices utilizing the SMS design.

The operation of the MCF as a sensor is fairly straightforward. The power in the MCF will be distributed throughout multiple supermodes, which will interfere throughout propagation down the MCF. When the light is coupled into the second single mode fiber in an SMS device, the power transmitted will be highly dependent on the distribution of light in the cores of the

MCF. Due to the wavelength dependency of the interference, the transmission spectrum will have a periodic modulation, as previously mentioned.

This transmission spectrum can then be used for sensing. Both the length and the refractive index of a fiber are sensitive to temperature, stress, pressure, etc. Thus, a change in the fiber's environment will cause an overall shift of the spectrum, which can then be tracked and used to measure the environmental changes. This sensitivity is based on the properties of the glass, namely the photo-elastic coefficient and the thermo-optic coefficient, which determine the change in refractive index for an applied strain and temperature, respectively, as well as Young's Modulus and the thermal expansion coefficient, which determine the dimensional changes for an applied force and temperature, respectively.

### Multicore Fiber Design

The design of the multicore fiber is an integral part of creating an optimal sensor. Several different designs have been explored in both simulation and experiment in order to determine the desired sensing parameters [58]. The most critical aspect of the design is the coupling from the SMF to the MCF, and the MMI this coupling produces in transmission. This was studied for MCF with three, seven, and 19 cores in both experiment and simulation. A finite difference method (FDM) mode solver in a commercial software package (FimmWave by Photon Design) was used to design the various MCF and measure their coupling and transmissive properties.

The number of supermodes in the MCF is determined by the number of cores and how many modes each core supports. Assuming each core is single mode, the number of supermodes equals the number of cores, times two for polarization degeneracy [59].

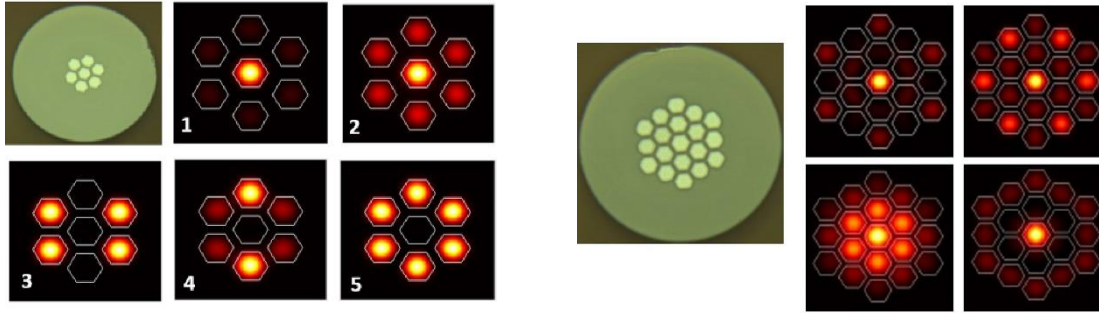


Figure 1. Facet images of a seven and 19 core fiber and a sample of their simulated modes.

Five of the supermodes supported by a seven core fiber and four of those supported by a 19 core fiber are shown in Fig. 1, along with the facet image of the fabricated fiber (made in CREOL). All of the supported supermodes are not always excited, and the percentage of light in each of the modes varies greatly with the excitation condition. For instance, for a SMS sensor configuration, the MCF will be excited by the fundamental mode of the SMF. In this case, only supermodes that are circularly symmetric with intensity in the central core will be excited. For the three and seven core fibers, two supermodes will be excited, and for the 19 core fiber, four supermodes will be excited. In Fig. 1, these are modes one and two for the seven core fiber, and the four modes shown for the 19 core fiber. The number of excited modes leads to drastically different transmission spectra. For the seven core fiber, the interference of modes one and two causes the intensity to oscillate between the central and the outer cores, resulting in a sinusoidal

transmission spectrum when the light is collected with a second SMF. The spectral periodicity is determined by the difference in propagation constants of the supermodes, as shown in Eqn. 3.

Figure 2 shows an example simulated SMS device with a seven core fiber. The interference within the MCF is clear, shown by the light coupling back and forth from the central to the outer cores as modes one and two are interfering. Figure 2 shows the interference for just one wavelength, but as mentioned previously this interference is wavelength dependent. As the physical origin of this interference is the difference in the propagation constants of the supermodes, and the difference in propagation constants varies with wavelength, the power distribution across the cores at the facet of the second SMF will vary periodically in the spectral domain, and the amount of light collected by the second SMF will vary accordingly.

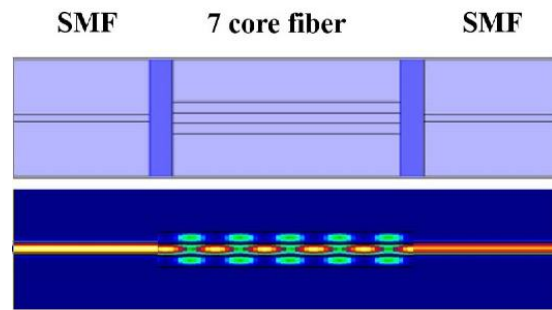


Figure 2. Simulated SMS device, showing MMI in a seven core fiber.

The transmission modulation period and modulation depth are highly dependent on several MCF design parameters, such as number of cores, core size, and core-to-core spacing. For a seven core fiber, the transmission spectrum is clearly periodic with sharp spectral features due to the interference of only two supermodes. Figure 3 shows an example transmission spectrum of a seven core fiber SMS device.

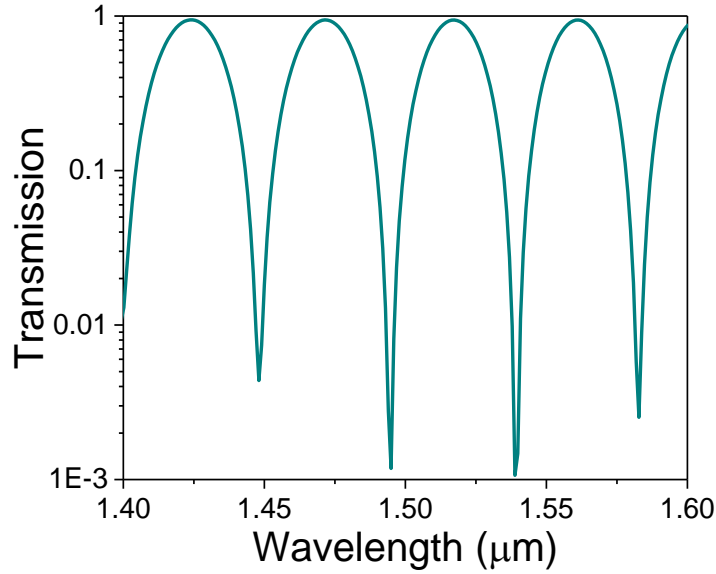


Figure 3. Transmission spectrum of a seven core fiber SMS device, showing interference of two supermodes.

A three core MCF also produces a sinusoidal transmission spectrum, as two supermodes are also excited in this fiber by a SMF. While both the three and seven core fibers have sinusoidal transmission spectra, the seven core fiber has a distinct advantage over the three core fiber in that it is symmetric. The symmetry of the seven core fiber will cause it to be much less sensitive to polarization than the asymmetric, birefringent three core fiber. This is shown in Fig. 4, where the MMI minima shifts in wavelength 10x more in the three core fiber than the seven core fiber when switching the polarization of the input light from the SMF in simulation. This makes the seven core fiber more attractive due to its simple periodic MMI and rigidity to polarization changes within the sensing setup.



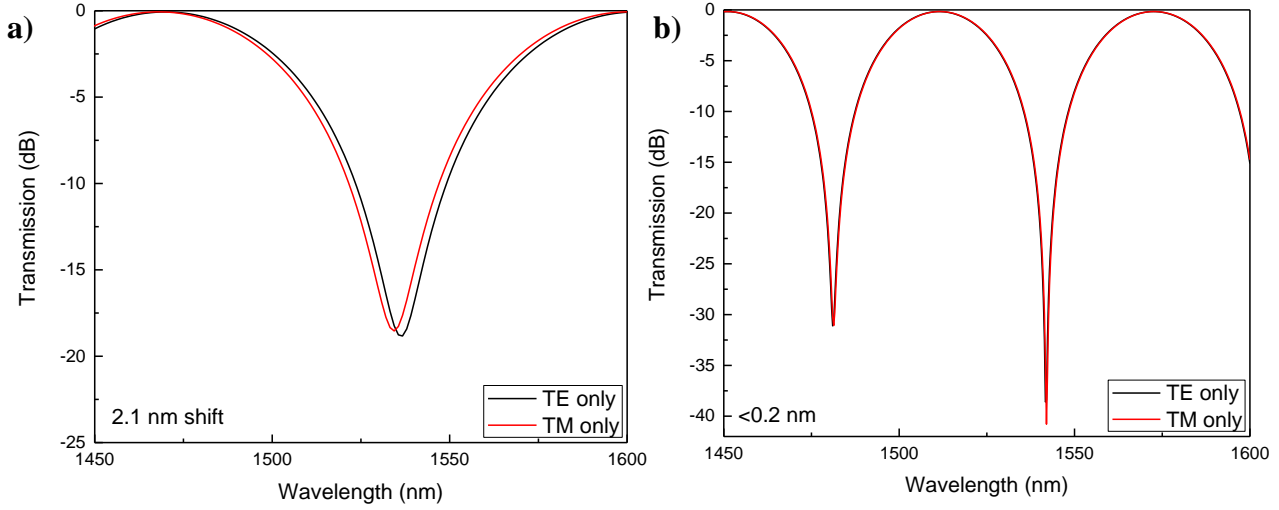


Figure 4. Simulated transmission spectra of TE polarized light and TM polarized light for a (a) three core MCF and a (b) seven core MCF.

The seven and 19 core fibers were fabricated using the stack and draw method with Ge-doped silica [5]. The refractive index profile of the drawn fiber was measured using a refractive index profilometer from Interfiber Analysis (IFA-100). The measured profile is shown in Fig. 5. The refractive index was measured for several different wavelengths, and was then fit to a Cauchy equation, Fig. 6. The dispersion relation was then included in the simulation. Small deformations and asymmetries in the drawn fibers were attempted to be matched in the simulation in order to obtain the most accurate spectra possible.

SMS devices were then created by splicing short lengths of the MCF between two SMFs (SMF28 from Corning). The splicing was performed with the SMF-SMF program of an Ericsson Splicer (FSU 995 PM). Four cm of seven core fiber and 12 cm of 19 core fiber were used in order to obtain several modulation periods in our wavelength region of interest, as the period of interference is dependent on the MCF length [47,60].

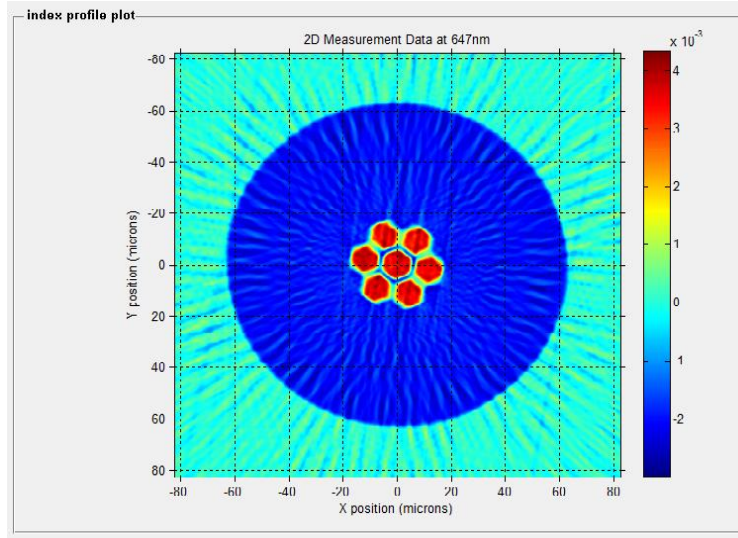


Figure 5. Measured refractive index profile of a seven core MCF.

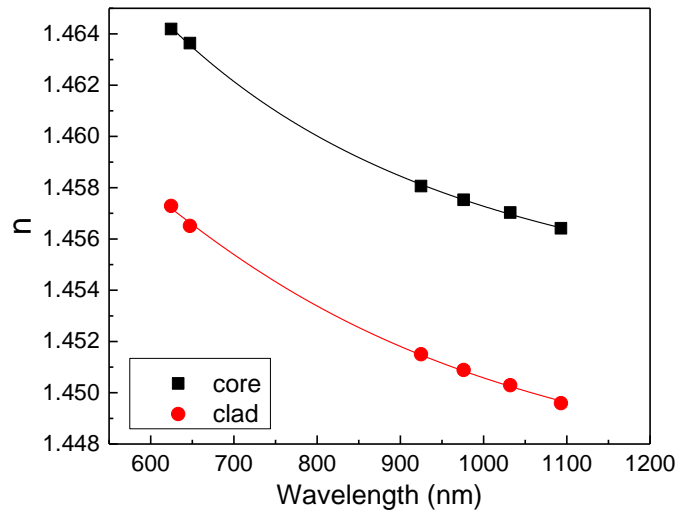


Figure 6. MCF refractive index values measured with a Cauchy fit.

A comparison between the simulated and experimentally measured transmission spectra is shown in Fig. 7. The small variations between the simulation and experiment are attributed to the margin of error in measuring the fiber geometry and refractive index of the drawn fiber.

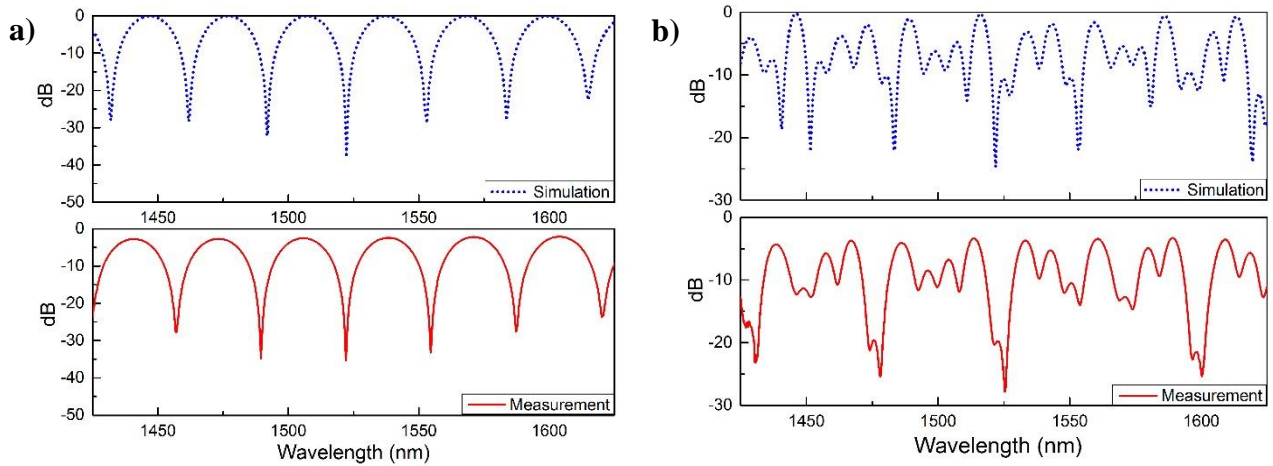


Figure 7. Simulated and measured transmission spectra of SMS devices with (a) seven and (b) 19 core fiber.

As previously mentioned, the SMF excites four supermodes in the 19 core fiber because of their central core intensity and radially symmetry. With four supermodes interfering within this MCF, a much more complicated transmission spectrum is produced. The periodicity is less clear, and the minima are not as sharp as with the three and seven core fibers.

As it has been determined that seven is the optimal number of cores for an SMS sensor utilizing MCF due to its predictable periodicity and symmetry, the exact geometry of these seven cores, including core size and spacing, was further investigated. The desired parameters of the SMS sensor are low transmission loss and sharp spectral features. This will allow several sensors to be connected in a chain for multiplexed measurements along the length of fiber.

In simulation it was found that the maximum depth of modulation occurred when equal amounts of the two interfering supermodes were excited by the SMF, because only when the two modes are equal in amplitude can complete destructive interference in the center core occur. This is demonstrated in Fig. 8, where the fraction of light excited in each mode (red and blue lines) is compared to the transmission spectrum of the SMS device (black line).

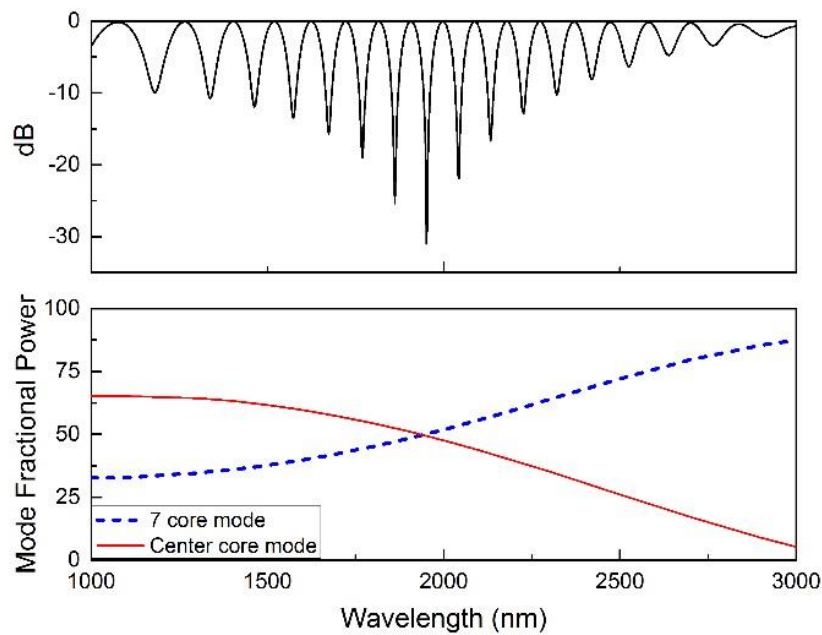


Figure 8. Comparison of transmission spectrum and excited mode power for a seven core device in simulation.

The fractional power excited in the supermodes is wavelength dependent because of the dependence of the mode field diameter (MFD) of both the SMF and MCF on the core and cladding refractive indices, which are wavelength dependent due to dispersion. Clearly the sharpest spectral features are observed when the mode fractional power is equally divided between the two interfering supermodes. Therefore, the mode field overlap between the SMF

and the seven core fiber at a given wavelength is a critical aspect in the design of the MCF for sensing applications.

This was experimentally verified by comparing two fabricated seven core fibers with slightly different core geometries. The first fiber has 9.5  $\mu\text{m}$  diameter cores, 13.6  $\mu\text{m}$  pitch, and 125  $\mu\text{m}$  outer diameter, as shown in Fig. 9 (a). The overlap between SMF and this fiber leads to 61% excitation of the center-only mode, and 38% excitation of the all-core mode. With this unequal excitation, a maximum modulation depth of 12 dB was measured, as shown in Fig. 9 (c). Alternatively, the second fiber has 9.2  $\mu\text{m}$  diameter cores, an 11  $\mu\text{m}$  pitch, and 125  $\mu\text{m}$  cladding (Fig. 9 (b)). With this small change in geometry, the excitation is now split almost equally between the two supermodes, and the maximum modulation depth reached 35 dB, also shown in Fig. 9(c). The second fiber design was optimized to have the maximum modulation depth near 1550 nm, but the wavelength can be tuned for other applications by changing the MCF geometry or the SMF input.

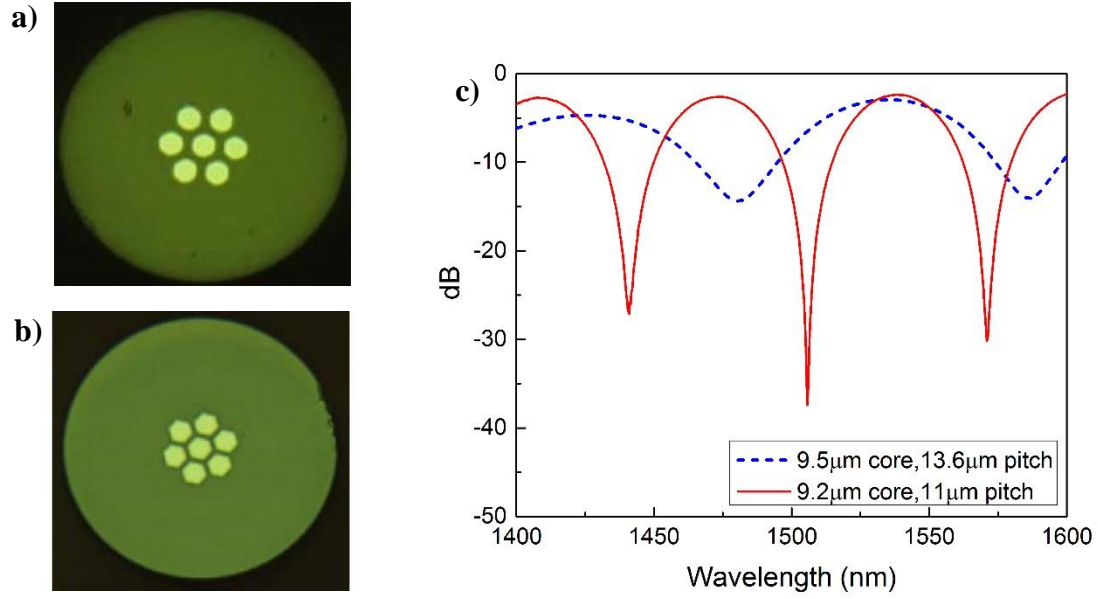


Figure 9. Facet images of the two tested seven core fibers (a) and (b), and (c) their respected transmission spectra.

In addition to sharp spectral features, high overall transmission is also important for an optimal sensor design. Low loss devices enable splicing multiple sensors together in a chain for multiplexed measurements along the length of the fiber. 100% transmission of the device can only occur when the fundamental mode of the SMF can be perfectly represented by the combination of supermodes of the MCF. As the total power excited in the two interfering supermodes of the MCF approaches 100%, the maximum transmission of the device also approaches 100%, as shown in Fig. 10.

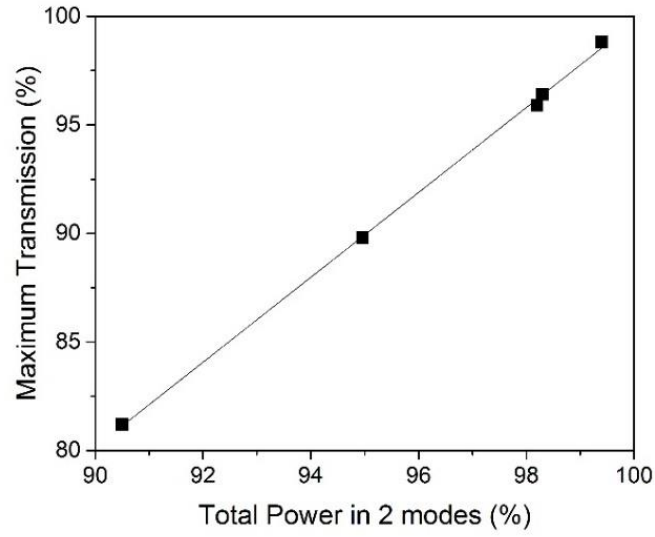


Figure 10. Maximum transmission for various excited mode powers from simulation.

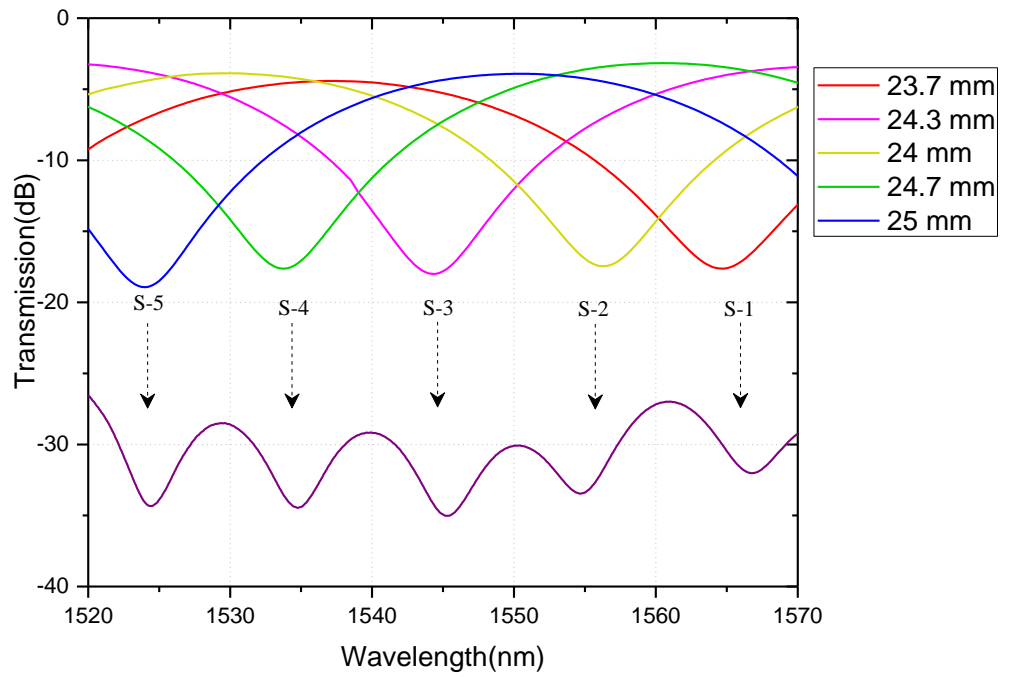


Figure 11. Transmission spectra of five individual sensors and a single multiplexed chain.

The loss of the spliced device with the optimal seven core design was measured to be less than 0.05 dB experimentally, showing both good mode field overlap as well as low splice loss between the SMF and the MCF.

Because of the high overall transmission obtained, multiple sensors were able to be multiplexed into a single chain. An example chain with five sensors is shown in Fig. 11. Here, slightly different lengths of MCF were used in order to space out the locations of the MMI minima, so each sensor can be individually monitored with a single transmission measurement. In simulation, the maximum number of MCF sensors that could be multiplexed within the C-band (1530-1565 nm) was investigated. Using the optimal seven core fiber design with very sharp spectral features, it was possible to multiplex 17 total sensors, with 11 within 35 nm (the same bandwidth as the C-band), as shown in Fig. 12.

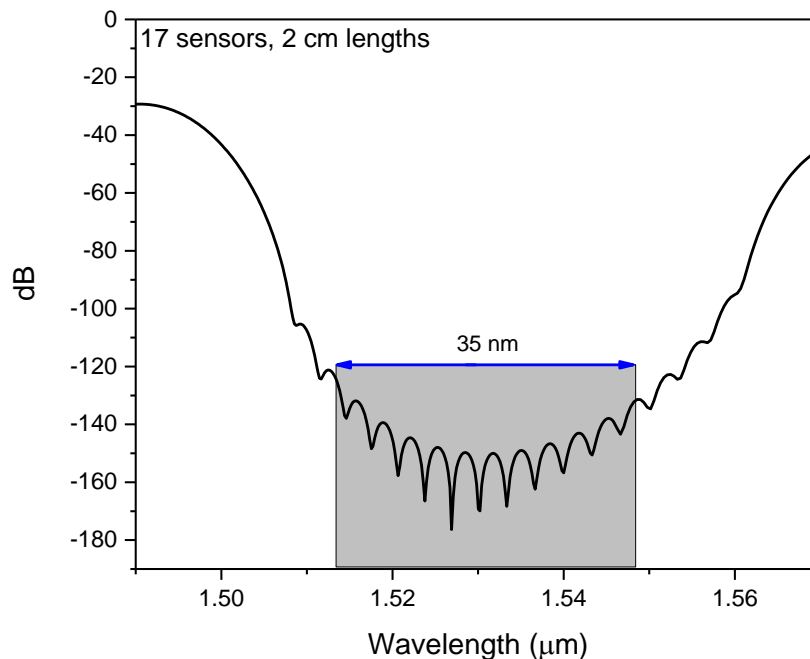


Figure 12. Simulated transmission spectrum of 17 MCF sensors with 2 cm lengths in a single fiber chain.



The sensor minima within this range all were still fairly sharp, with at least 10 dB depth and about 3 nm spacing between them. However, the level of transmitted light dropped extremely low, down to about 160 dB, which is below the noise floor of many spectral analysis instruments. If high levels of multiplexing are needed, larger spectral windows would need to be used in order to increase the spacing between each sensor's minima and increase the transmission level between the minima.

The design of the MCF has been optimized, with the final design being seven cores, approximately 9  $\mu\text{m}$  core diameters and an 11  $\mu\text{m}$  pitch, and a numerical aperture of 0.13. When using SMF28 as the input/output fiber, this causes a mode field excitation close to 50%:50% for the two interfering supermodes at the wavelength of 1550 nm, leading to high overall transmission and very sharp spectral features, enabling multiplexing as well as high resolution sensing.

### Sensitivity Measurements

#### Temperature

One of the most unique and advantageous aspects of this MCF sensor is its ability to withstand high temperatures. As previously mentioned, FBGs can only withstand temperatures up to 200-300°C, and there are many applications that require much higher temperatures. Industries such as oil drilling and nuclear power plants require sensors that can withstand harsh environments as well as temperatures well above a few hundred degrees Celsius.

Recently there have been many attempts to increase the maximum operational temperature with various fiber sensor designs. An SMS sensor utilizing photonic crystal fiber (PCF) was shown to be capable of measuring 500°C [61]. This required selectively collapsing regions of the PCF, as well as precise offset splicing. Demas et al. showed a fiber-optic sensor capable of measuring up to 1000°C with a device utilizing a PCF and a CO<sub>2</sub> laser-written long-period grating [62]. Also, alternative methods for writing FBGs have been developed in order to increase their ability to withstand high temperatures. Femtosecond written gratings [25] and regenerated FBGs [22] have both been reported to withstand temperatures up to 1000°C. However, these gratings have more complicated fabrication processes, and regenerated gratings have significantly reduced reflectivities.

The MCF device, as previously mentioned, has a very simple design and fabrication process. As it consists of only two standard splices, two people were able to fabricate over 120 sensors in less than two days. In addition to being very simple and inexpensive to fabricate, this device has a much higher temperature limit than most standard fiber sensors.

The temperature sensitivity of the MCF sensor has been measured up to 1000°C with a very stable response [63]. This was measured in a high temperature oven with a superluminescent diode (SLD) and an optical spectrum analyzer (OSA) and is shown in Fig. 13.

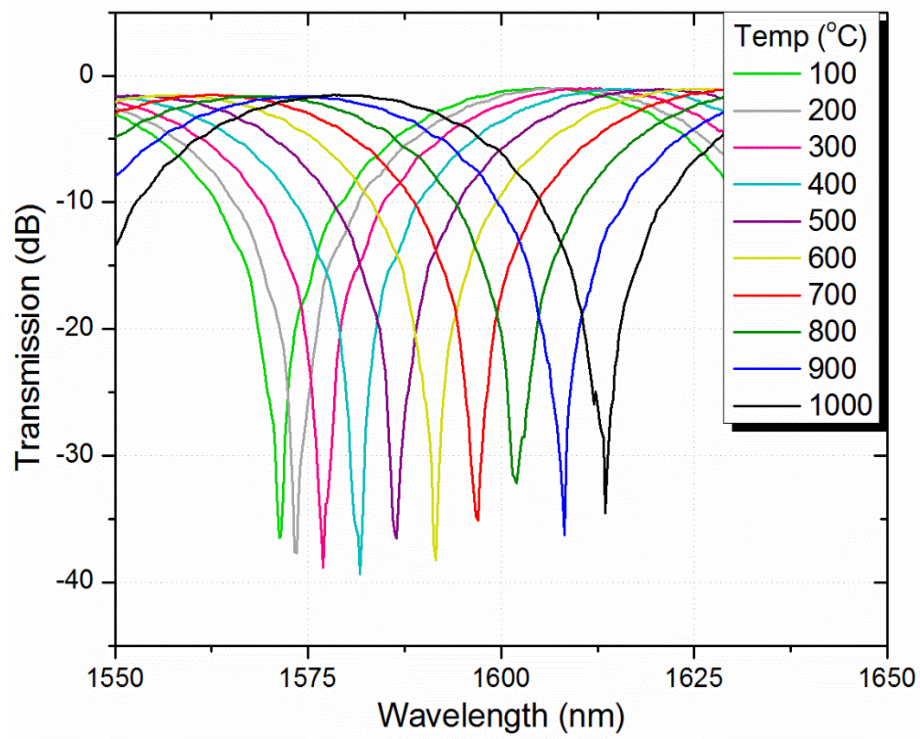


Figure 13. Transmission spectra of a 2 cm MCF sensor measured in a high temperature oven up to 1000°C [63].

The wavelength shift with temperature was observed from room temperature to 1000°C, held for five hours, and then cooled back to room temperature. The sensor's response is shown in Fig. 14. This cycle was repeated five times, and no hysteresis or degradation of the spectrum was observed, making them extremely useful for harsh environment applications.

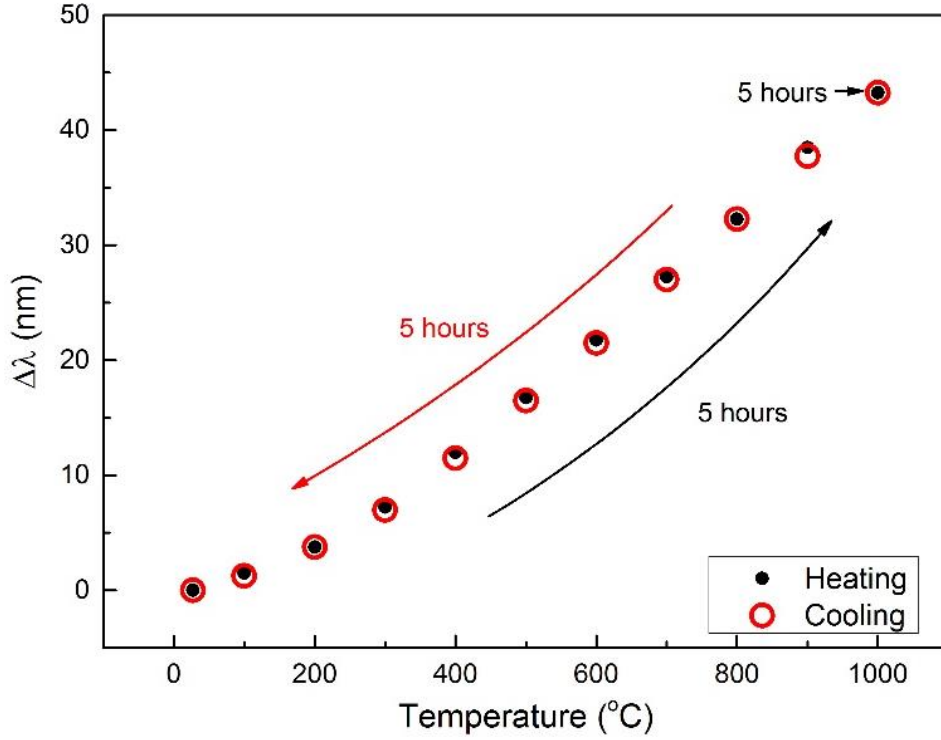


Figure 14. Sensor wavelength shift of seven core fiber device in a high temperature oven.

It was observed that the wavelength shift with temperature was not linear throughout the entire temperature range measured. The assumed reason for this is a variation in the thermo-optic coefficient with increasing temperature, which has been previously studied for cryogenic temperatures [64]. The experimental result was used in combination with simulation in order to determine the thermo-optic coefficient of the MCF as a function of temperature. The thermo-optic coefficient is what determines the shift of the refractive index of a material with change in temperature and is given by Eqn. 6:

$$n(T + \Delta T) = n(T) + \alpha \Delta T \quad (6)$$

where  $n$  is the index of refraction,  $T$  is the initial temperature,  $\Delta T$  is the change in temperature, and  $\alpha$  is the thermo-optic coefficient.

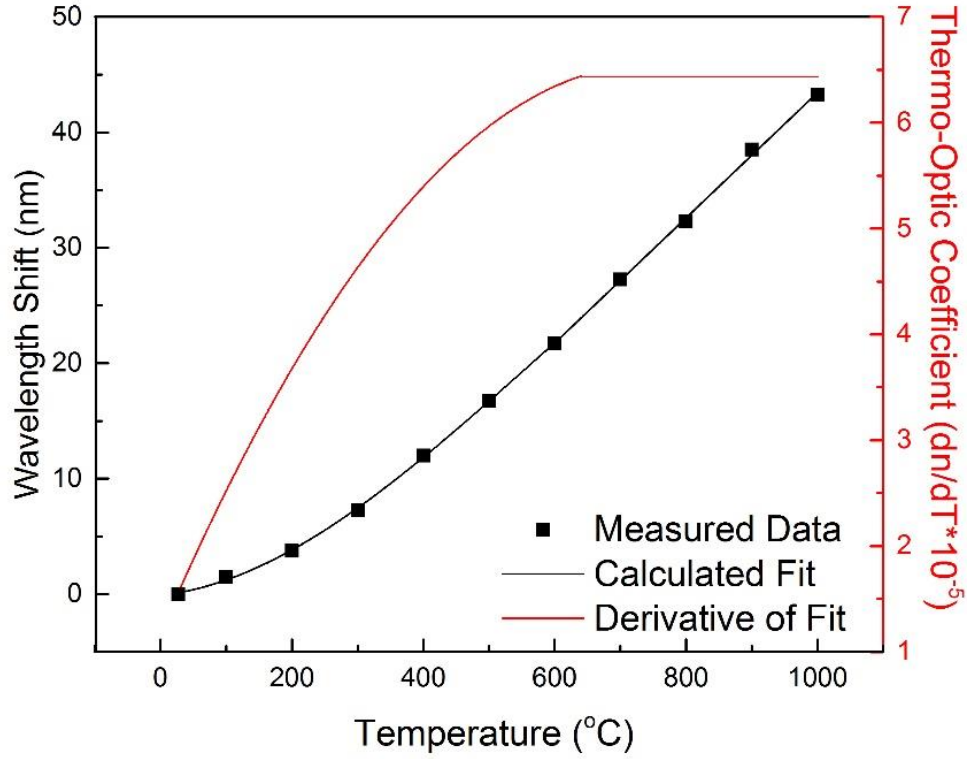


Figure 15. Measured wavelength shift and corresponding calculated thermo-optic coefficient.

While the length of the fiber also changes with temperature due to the thermal expansion coefficient, this effect is negligible when compared to the index change. By comparing the experimentally measured wavelength shift to that produced in simulation by adjusting the refractive index, a thermo-optic coefficient was calculated and fit to a cubic function from 0-600°C and a linear function from 600-1000°C, as shown in Fig. 15. The calculated value of the thermo-optic coefficient as a function of temperature was found to be:

$$\frac{dn}{dT} = 1.2 + 0.01T - 9.4 \times 10^{-6}T^2 - 2.3 \times 10^{-10}T^3 \quad 20^\circ\text{C} < T < 600^\circ\text{C} \quad (7)$$

$$\frac{dn}{dT} = 6.43 \quad 600^\circ\text{C} < T < 1000^\circ\text{C} \quad (8)$$

## Strain

While high temperature measurements are the primary application, the multicore sensor can also be used to sense alternative parameters, such as strain or longitudinal force [65]. As the fiber is pulled along its axis, the refractive index of the glass changes and the fiber elongates. The longitudinal force applied causes a strain,  $\varepsilon$ , in the fiber which leads to a change in its length,  $L$ , shown in Eqn. 9.

$$\varepsilon = \frac{\Delta L}{L} \quad (9)$$

Also, the refractive change is dependent on the applied strain as shown in Eqn. 10, where  $\rho$  is the photo-elastic coefficient of the material.

$$n(\varepsilon + \Delta\varepsilon) = n(\varepsilon) + \rho\Delta\varepsilon \quad (10)$$

These effects will shift the MMI pattern in a similar way to temperature. An example of a shift in the MMI of the transmission spectrum is shown in Fig. 16. Here, the spectrum shifts negatively in wavelength with an applied strain.

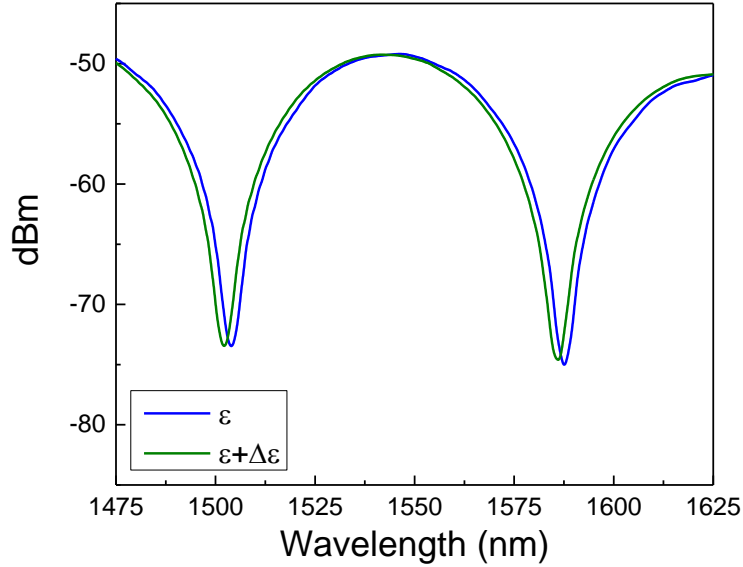


Figure 16. Wavelength shift measured from an applied strain on a MCF sensor.

Fiber optic sensors have been used to measure strain in a variety of configurations, and the sensitivity has been increased through methods such as inflating long period fiber Bragg gratings using a CO<sub>2</sub> laser [66] and reducing the cladding diameter of a fiber containing an FBG [67]. Reducing cladding diameter was shown to be a much simpler and more effective approach, so its effect on the MCF sensors was investigated.

An experimental setup to measure the force and strain sensitivity of the MCF sensor was developed, and is shown in Fig. 17. A fiber chain was created with a standard FBG with 125 μm outer diameter (OD) to be used as a reference, a second FBG with an etched cladding, and a section of MCF with an etched cladding, in order to compare the sensitivities of the MCF and the FBG, as well as understand the relationship between sensitivity and cladding diameter. The ends

of the fiber chain were then wound around posts to ensure they didn't slip as the fiber was pulled.

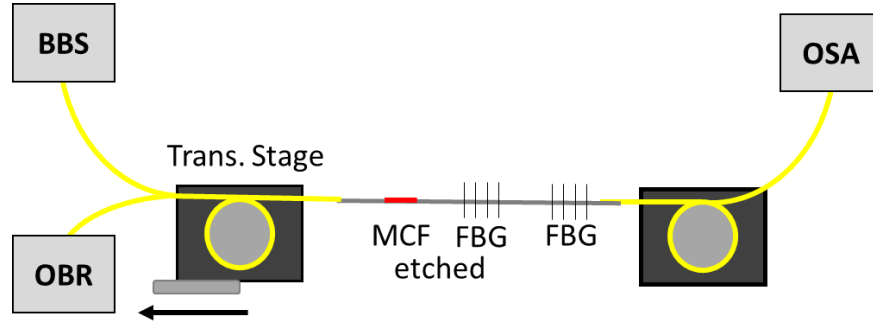


Figure 17. Experimental setup for measuring strain sensitivity and comparing MCF and FBG sensors.

One post was fixed, while the other was placed on a translation stage, applying longitudinal force to the fiber as it moved out along its axis. A broadband source (BBS) was used with an OSA to measure the MCF spectra, and simultaneously, an Optical Backscatter Reflectometer (OBR) was used to measure the FBG's reflections.

The refractive index change and elongation of the fiber caused by the applied force according to the photo-elastic coefficient and Young's Modulus, shifts the interference pattern of the transmission spectrum. A comparison of wavelength shifts is shown for three sensors, an MCF sensor in Fig. 18 (a) and two FBGs in Fig. 18 (b). As all three sensors are in a single fiber chain, the applied force is consistent for each sensor, but the stress experienced by each one is dependent on the fiber's outer diameter because stress is equal to force/area. A smaller cross sectional area of the fiber produces a higher stress, which leads to a higher strain, according to Young's modulus as shown here:

$$E = \sigma \varepsilon = \frac{F/A}{\Delta l/l} \quad (11)$$



where  $E$  is Young's Modulus, which is 73 GPa for fused silica,  $\sigma$  is stress,  $\epsilon$  is strain,  $F$  is force,  $A$  is cross-sectional area,  $l$  is the fiber length, and  $\Delta l$  its change due to the applied force.

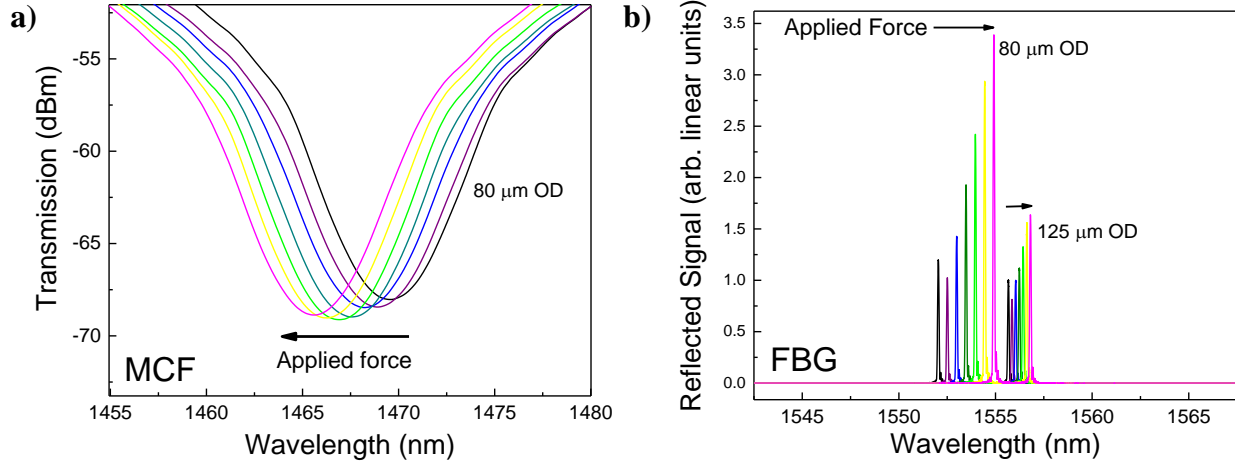


Figure 18. Example wavelength shifts caused by applied longitudinal force for a MCF sensor (a) and an FBG (b).

A smaller outer diameter therefore leads to a higher strain for a given applied force, which in turn leads to a larger wavelength shift in transmission. A plot of the wavelength shift for both the MCF sensor and the FBGs as a function of applied force is shown in Fig. 19. The strain sensitivity of each device is constant, while the force sensitivity increases with decreasing outer diameter. A summary of all devices tested as a function of fiber outer diameter is shown with a parabolic fit in Fig. 20, which agrees with the dependence of the strain on the cross-sectional area of the fibers.

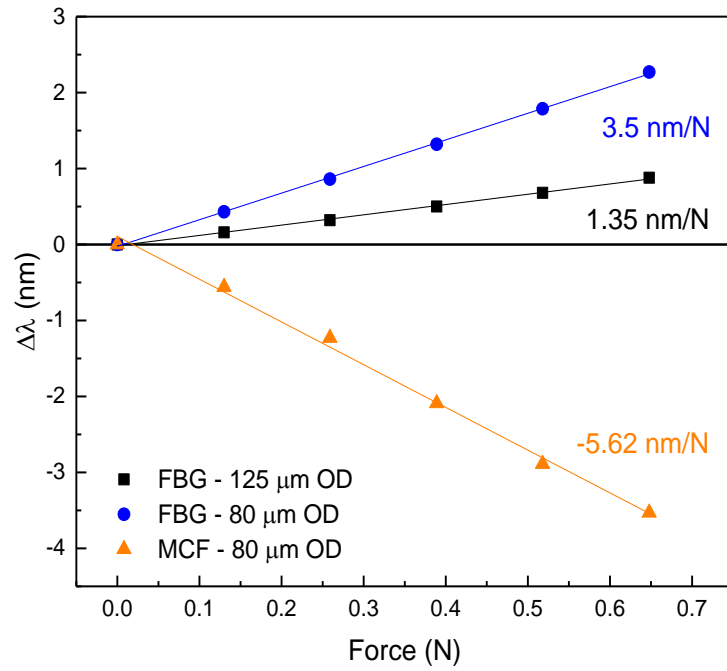


Figure 19. Example wavelength shift of three sensors in a chain.

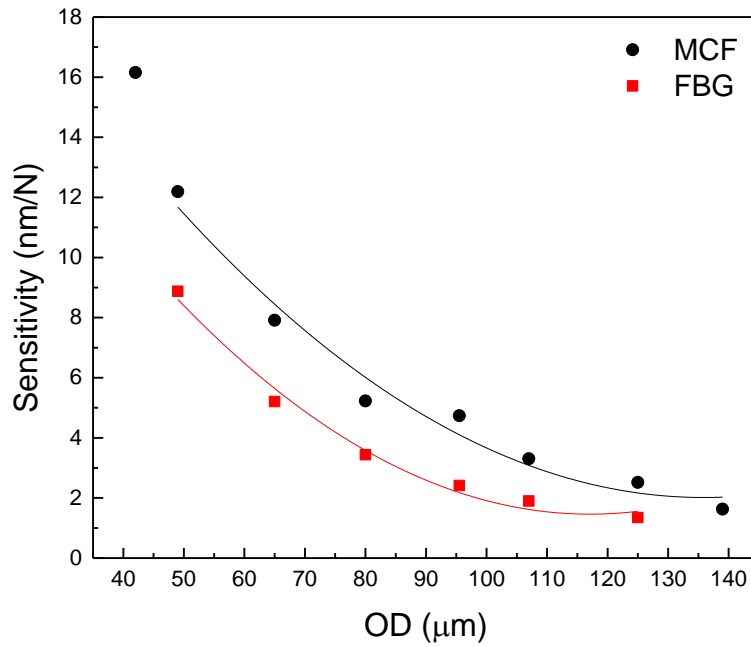


Figure 20. Summary of all measured sensitivities for MCF and FBG devices as a function of OD.

Decreasing the OD of the MCF is a simple way to increase the sensitivity of the sensor to force, and can be done through fiber etching or initially fabricating a MCF with a smaller cladding. The 42  $\mu\text{m}$  MCF sensor had an overall sensitivity increase of 7x that of a 125  $\mu\text{m}$  MCF device, and 12x that of a standard FBG. Etched FBGs showed a similar increase in sensitivity, also following a  $(1/\text{OD}^2)$  dependence, but were consistently about 40% less sensitive than the MCF devices with the same OD.

In addition to measuring strain individually, a method for simultaneous measurement of strain and temperature was developed by combining two multicore sensors with different outer diameters. FBGs have been used in configurations for decoupling simultaneous strain and temperature measurements [68,69], as well as fiber optic sensors operating on the principle of MMI [50,70]. Because the sensitivity of the MCF device to longitudinal force can be easily tuned through the OD, two devices can be used in combination to decouple force and temperature measurements. This experiment was performed with a fiber chain now consisting of a standard 125  $\mu\text{m}$  OD FBG for reference again, a 125  $\mu\text{m}$  OD section of MCF, and an 80  $\mu\text{m}$  OD section of MCF. The two MCF segments were suspended in glass capillaries over hot plates for temperature tuning, and the whole chain was placed in the same force application setup as Fig. 17. The transmission spectra of the two MCF devices is shown in Fig. 21 (a). Splicing the two devices together into a chain creates the transmission spectrum shown in Fig. 21 (b).

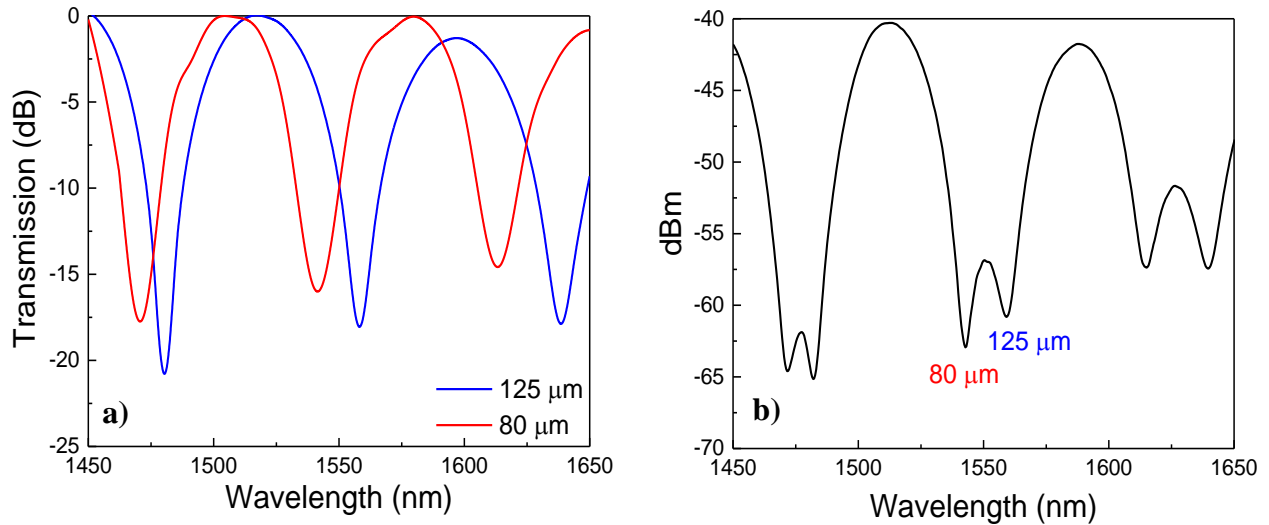


Figure 21. Transmission spectra of two MCF devices separate (a) and spliced in a chain (b).

While both sensors are still clearly visible when spliced together, better definition could be achieved by selecting sensors whose minima were further spaced out in wavelength. The location of the minima is easily tuned by fiber length, as shown here [60]. With both MCF devices now in a single chain, their responses to various changes can be monitored simultaneously with one transmission spectrum.

As force is applied to the fiber chain, both minima shift in wavelength, but by varying amounts as shown in Fig. 22. This is due to the difference in fiber outer diameter of the two sensors.

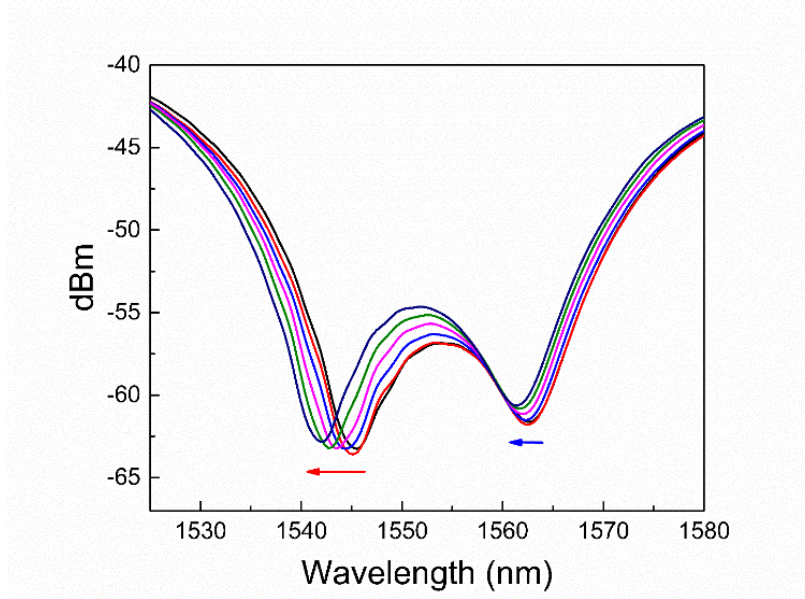


Figure 22. Response of sensor chain to applied longitudinal force.

The temperature sensitivity of each device was also measured using hot plates and was found to be 29 pm/°C, equal for both devices because outer diameter has no effect on the temperature sensitivity. The response of the MCF devices to both an application of longitudinal force as well as a temperature increase is shown in Fig. 23. To determine the strain and the temperature experienced by the MCF devices, the following equations can be used:

$$\Delta\lambda_{80} = a\Delta F + c\Delta T \quad (12)$$

$$\Delta\lambda_{125} = b\Delta F + c\Delta T \quad (13)$$

where  $a$  and  $b$  are the force sensitivities shown in Fig. 19, and  $c$  is the temperature sensitivity listed above.

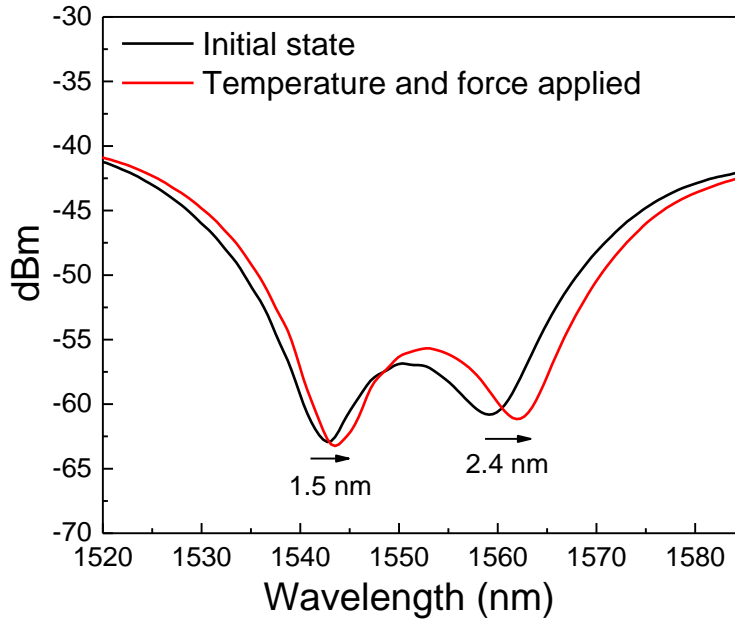


Figure 23. Response of sensor chain to applied force and temperature.

The experimental results were found to be very accurate. Using the measured shift with these equations, the temperature was calculated to be 134°C, while a thermal camera image of the hot plates gave a value of 133°C, which is within 1% of the experimental measurement. The measured force was 0.33 N, corresponding to a strain of 0.905 mε for an OD of 80 μm, and 0.371 for 125 μm. The measured strain from the 125 μm OD reference FBG was 0.381 mε, with is within 3% of the calculated value.

Next, the MCF sensors were strength tested to know their maximum measureable strength before breaking. Using 125 μm OD fiber, MCF to SMF splices were stressed in a similar setup to Fig. 17, until the splice breaking point. This test was repeated several times and compared to SMF to SMF splices in the same setup. It was found that the MCF-SMF splices survived to an average strain of 7.11 mε, and SMF-SMF splices survived to 7.55 mε. This shows

that the MCF-SMF splices are just as strong as typical SMF-SMF splices, and they are robust enough to withstand environments with up to several millistrain applied. It is important to note that decreasing the outer diameter may in turn decrease the strength of the fiber, as the 42  $\mu\text{m}$  OD sensor only withstood up to 3 me before failure, but this has not been fully investigated.

### Bending

In addition to temperature and strain, the MCF sensors are also sensitive to bending. The ability to measure the curvature of an object is extremely important in applications such as mechanical and aerospace engineering, and structural health monitoring. The bending sensitivity was investigated with a simple experiment using the seven core fiber [71]. However, this experiment only gives information about the radius of curvature of the fiber, without any directional dependence. An example plot of the wavelength shift for various radii of curvature is shown in Fig. 24.

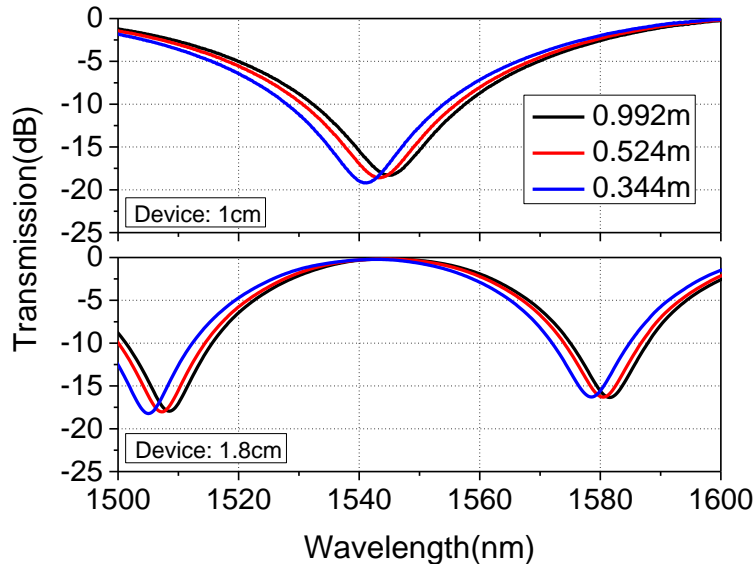


Figure 24. Transmission spectra shift of two MCF sensors as a function of bending radius [72].

Knowing both the radius of curvature and the direction of the bending can be very useful in evaluating structural integrity, as these parameters help in identifying deformations and stresses in structures. Many fiber sensing systems have been investigated for applications as direction-sensitive bending sensors. The majority of these sensor systems employ some form of fiber grating, including long period gratings [73], cladding waveguide gratings [74], and FBGs in MCF [75]. While grating based systems such as these have been able to successfully measure bending while distinguishing multiple directions, the fabrication of the gratings is a fairly complicated process. In addition to grating-based systems, a commercial shape sensing system based on Rayleigh scattering was developed by Luna Technologies. This system has high accuracy and requires a MCF, but does not need any type of grating. However, the optical frequency domain reflectometry method used is computationally complex and requires the sweeping of a tunable laser source, resulting in high cost instrumentation [76]. The MCF sensors based on the MMI from coupled cores are generally much simpler to fabricate, however, they still rely on spectral analysis instrumentation, such as an OSA. By combining the MCF with a Photonic Lantern (PL), the need for spectral analysis can be eliminated and replaced by simple power measurements [77].

### Photonic Lantern Experiment

A PL is an all-fiber device consisting of a number of SMFs that are fused together and tapered down to form a single MMF or FMF [16], and a representation of a PL is shown in Fig. 25. This device is reciprocal, in that either the MMF or the SMFs can be used as the input,



depending on the application. Generally, there is no direct correlation between the SMF and the modes of the MMF, as the initial applications of the PL only required transfer between single mode and multimode systems. One example of this application is astronomical instrumentation [78], where light collected into a MMF via a telescope needs to be transferred into SMF in order to utilize narrow bandwidth FBGs.

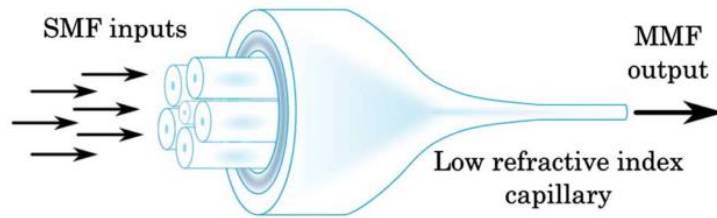


Figure 25. Schematic showing the basic device structure of a photonic lantern [79].

More recently, mode-selective PLs have been developed, where the SMFs are mapped to the modes of the MMF [80]. This is a developing technology with the main application being spatial division multiplexing in telecommunications [16,79]. When a mode-selective PL is used with the SMF end as the input, each SMF excites a different LP mode in the output MMF, with low cross-talk between the modes.

In the following experiment, the PL is used in the opposite direction, with the power in the various modes of a FMMF being measured through its corresponding SMF output. This ability to measure the power in each mode of a MMF using an all-fiber device leads to new possibilities for the field of fiber sensing.

In order to get both radius of curvature and bending direction information, a three core fiber is used in conjunction with a mode-selective PL. The MCF has strongly coupled cores, similar to the seven core fiber that was previously demonstrated as being bend-sensitive [71].

This combination of all-fiber devices has several benefits over the previous experiment. The PL allows for the interrogation to be done with a power meter, as opposed to a spectrum analyzer, lowering the cost of the instrumentation as well as increasing the measurement sensitivity. Additionally, the amount of information gained from one experiment is multiplied by the number of channels of the PL, as each mode will have its own response to bending. Finally, using a three core fiber instead of the seven core fiber adds asymmetry into the system which makes it direction sensitive.

The MCF used was fabricated in-house using the stack and draw method. The three cores are 9  $\mu\text{m}$  in diameter, with a pitch of 11  $\mu\text{m}$ , and the fiber outer diameter is 120  $\mu\text{m}$ . The fiber was fabricated from Ge-doped silica, with a  $\Delta n$  of  $7 \times 10^{-3}$  and each core had an NA of 0.14. The cross section of the MCF is shown in Fig. 26. The mode-selective PL was also fabricated in-house by first drawing four Ge-doped graded-index fibers (GIF) with a  $\Delta n$  of  $16 \times 10^{-3}$  and core sizes of 20, 18, 15, and 6  $\mu\text{m}$ . The GIFs are spliced to SMF ensuring the excitation of only the  $\text{LP}_{01}$  mode. The various core sizes will excite different LP modes in the FMF ( $\text{LP}_{01}$ ,  $\text{LP}_{11a;b}$ ,  $\text{LP}_{21a;b}$ , and  $\text{LP}_{02}$ , respectively [79]. Six GIFs (one each of the 20 and 6  $\mu\text{m}$  and two each of the 18 and 15  $\mu\text{m}$  diameter) are then inserted into a low index capillary made of fluorine-doped glass with a  $\Delta n$  of  $-9 \times 10^{-3}$  relative to fused silica in the arrangement shown in Fig. 26. A  $\text{CO}_2$  laser tapering station (LZM-100 by AFL) is then used to taper the filled capillary. As the device is tapered to a final taper ratio of 15.9:1 over a 50 mm length, the individual cores become negligible and the light is guided in the cladding of the GIFs, which in the tapered section, form a FMF with a core size of 18  $\mu\text{m}$ . This end of the lantern is spliced to a FMF with a core size of 15

$\mu\text{m}$  and a  $\Delta n$  of  $11 \times 10^{-3}$  that supports only the six LP modes previously mentioned. The experimental setup used is shown in Fig. 26.

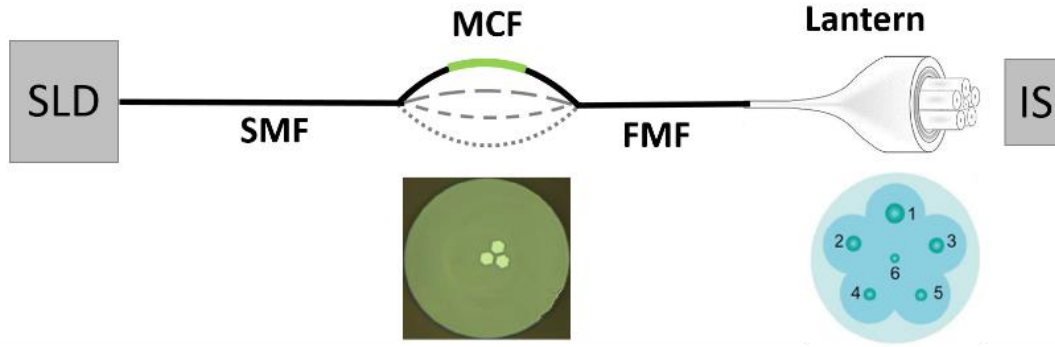


Figure 26. Experimental setup for bending test with a PL, showing the MCF cross section as well as the arrangement of SMF in the lantern.

The light source used was a SLD centered at 1550 nm coupled into a SMF, which then was used to excite the three core fiber, with one of the three cores being centrally aligned with the core of the SMF. The MCF supports three polarization degenerate supermodes, as shown in Fig. 27. As previously described, there will be supermode interference within the MCF [58]; however, by using a very short section of MCF, the spectral period of the interference pattern will be hundreds of nanometers, and the interference fringes will be outside of the SLD bandwidth. In order to obtain a smooth transmission spectrum throughout the  $\sim 40$  nm bandwidth of the SLD, a 0.5 cm section of three core fiber was used. The MCF is then spliced to the FMF end of the PL that supports the six LP modes shown in Fig. 27. The output power from the SMF outputs of the lantern is then measured with an integrating sphere (IS). The MCF section is bent by fixing the fiber inside of a plastic tube and forcing it to bend through the inward movement of

a translation stage in a similar setup to [71], which allows for complete control over the bending radius and direction.

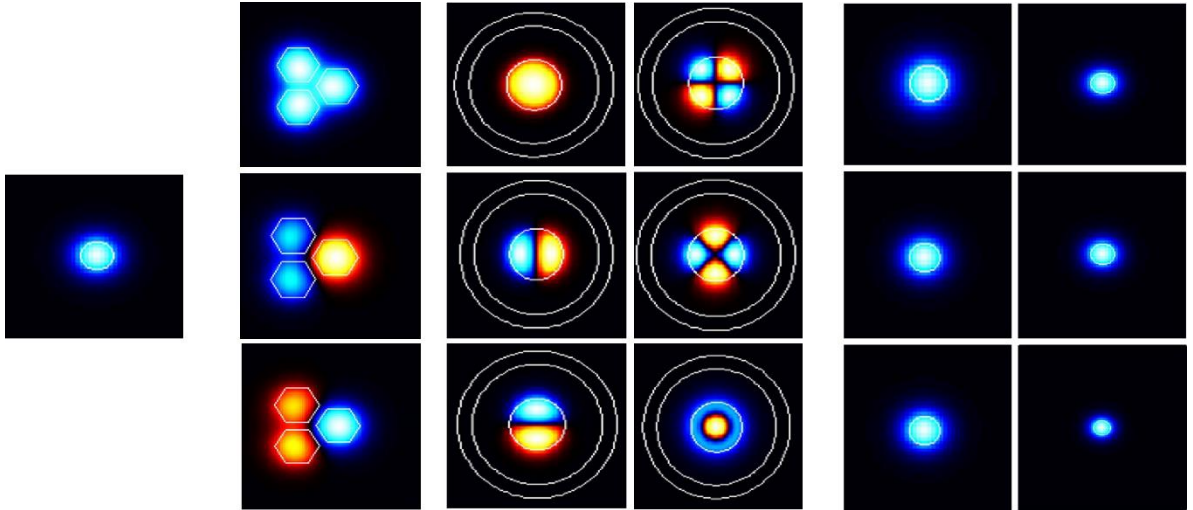


Figure 27. Simulated modes of each fiber in the bending experiment: SMF, MCF, FMF, GIFs of varying core size, respectively.

Bending the MCF changes the refractive index profile, and therefore changes the supermodes, their excitation from the SMF, and their propagation. Altering the supermodes of the MCF then changes the excitation of the FMF modes. The power in each of the FMF modes is measured from the SMF outputs of the PL, and the change in relative power of each mode is measured as a function of radius of curvature of the MCF bending, which is then repeated for multiple bending directions. Before discussing the relative power measurements, it was verified that a change of the excited power of the FMF modes was being observed and the power changes were not caused by a spectral shift due to multimode interference. To do this, the transmission spectrum of the entire experimental fiber chain was recorded as the MCF was bent. As shown in Fig. 28, the total power of mode  $LP_{11a}$  transmitted through the PL does in fact increase and decrease with bending, with no noticeable spectral shift. Figure 28 (a) shows small interference

fringes caused by the multiple excited modes of the FMF which do not shift as the MCF is bent in either direction by a radius of 23 cm. Figure 28 (b) shows the same spectra, smoothed by a Savitzky-Golay filter, clearly showing the total change in power for this mode, which for the same bending radius is dependent on the bending direction.

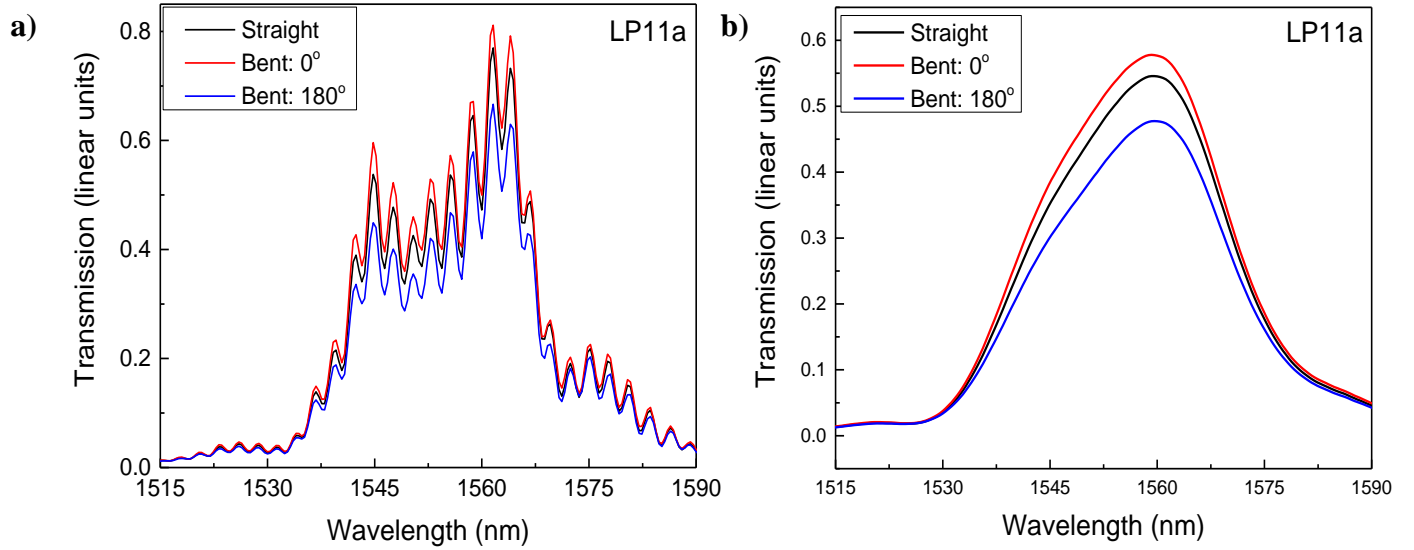


Figure 28. Transmission spectra of the LP11a mode when bent in two directions with a radius of 23 cm, with spectral smoothing applied during the post processing. (a) A nine-point Savitzky-Golay smoothing filter was used showing the multimode interference occurring within the FMF, and (b) with a 65 point filter, more clearly showing the total power difference.

The relative power shift (change in power/initial power or  $\Delta P/P_0$ ) measured for each of the six lantern modes for four bending directions is shown in Fig. 29. Each mode power responds differently to bending, and this response changes with bending direction. For some modes, the relative power change was as high as 80%, showing exceptional sensitivity. As shown in Fig. 29, the change in relative power can be either linear or curved with respect to the inverse radius of curvature, depending on the mode and the direction of bending. The highest sensitivity observed

experimentally was in the direction of  $270^\circ$  for the LP<sub>21a</sub> mode, with  $20.2\%/m^{-1}$  with respect to the inverse radius over the region from  $0.01$  to  $0.04\text{ cm}^{-1}$ , or  $2.3\%/cm$  with respect to the radius of curvature from  $20$  to  $40\text{ cm}$ .

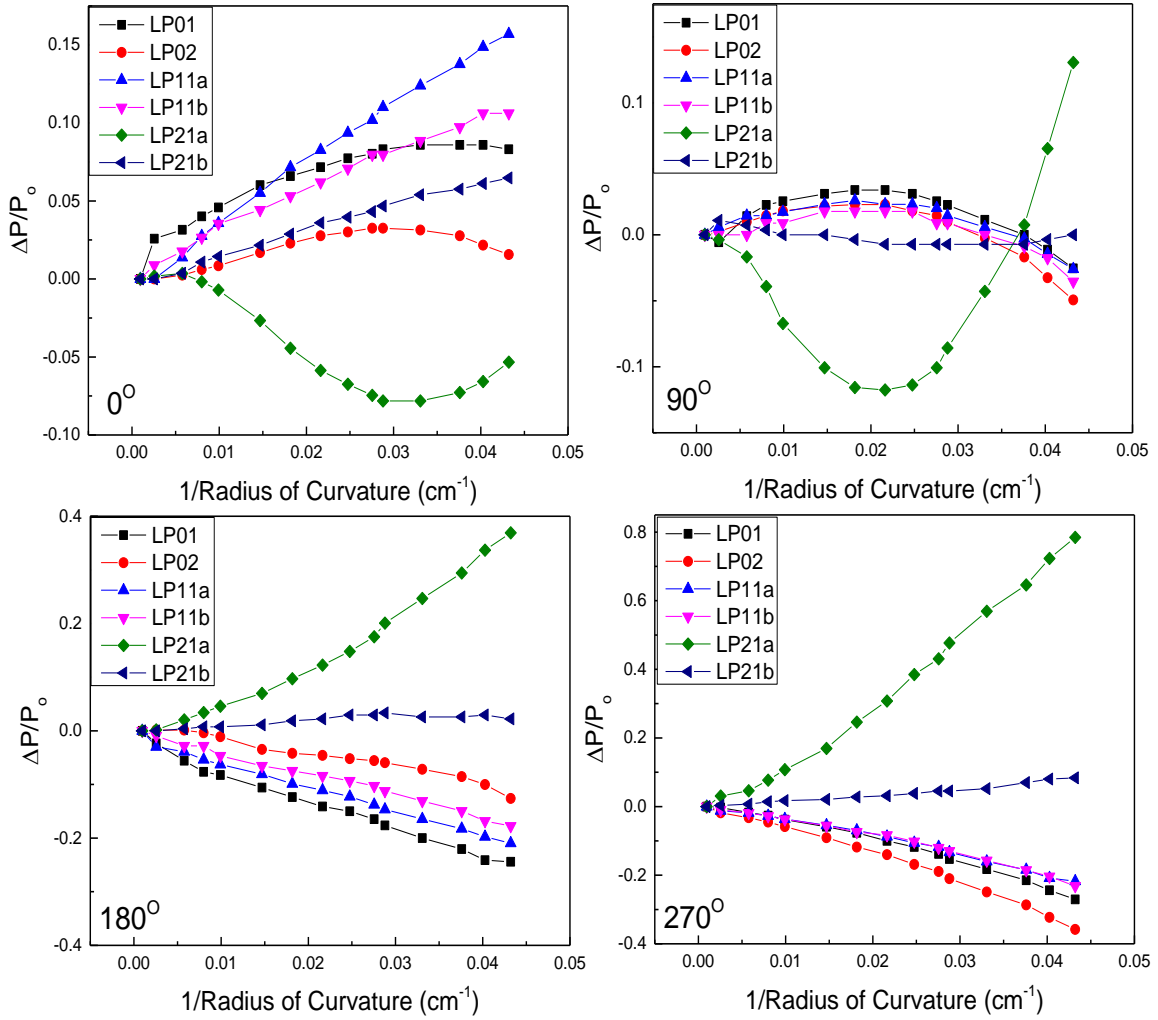


Figure 29. Relative power shifts of each of the FMF modes measured as a function of the inverse radius of curvature for four different bending directions

The variations in sensitivity with bending direction could be understood if the experiments were designed in such a way that enabled knowledge of the MCF orientation within

the bending setup; however, this experiment was not done with that knowledge. Using a PL with six modes, each mode having different responses to bending, enough information can be obtained in order to fully measure the angle and the radius of curvature of the bend simultaneously.

To verify the necessity of the MCF as the bend sensitive element, the experiment was repeated with the previous setup, but with a section of the FMF being bent while the MCF was kept straight. Bending the FMF resulted in very small changes in the power of the modes. For a bending radius of 27 cm, the total relative power shift was less than 4% for all modes and bending directions, with the average being only 1.6%. This measured sensitivity is clearly significantly lower than that measured while bending the MCF section, showing that the high sensitivity of this system is dependent on the strong coupling of the supermodes in the MCF.

To gain more understanding as well as predictive capabilities in designing a 3D fiber optic bending sensor with MCF, the device was simulated using commercial waveguide software FimmWave. The SMF–MCF–FMF fiber chain was created, and bending was applied to the MCF segment with full control over both the radius of curvature and the direction of the bend. The power in each of the FMF modes was calculated as a function of inverse bend radius for several different bending directions, two of which as shown in Fig. 30. Very similar slopes and total relative power changes to those measured experimentally were observed in simulation, giving confidence to the accuracy of the sensing system. The simulations also show a large directional dependency. Figure 30 (a) was calculated for a bending direction of  $90^\circ$  and Fig. 30 (b) was

calculated for  $180^\circ$ . As the orientation of the three MCF cores was not known experimentally, an exact match between the measured mode power shifts and those in simulation was not obtained.

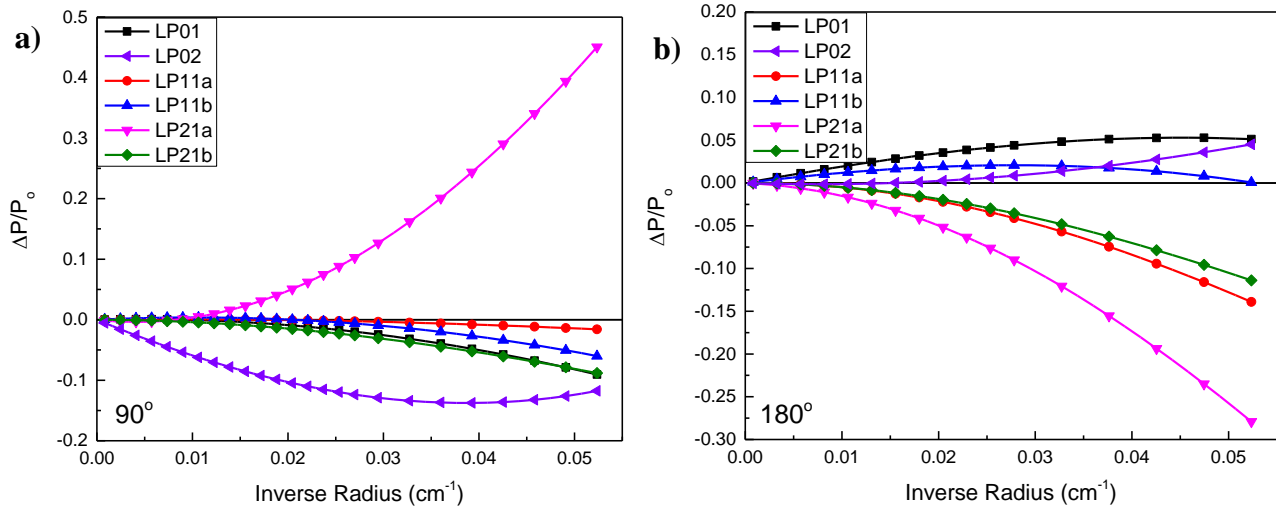


Figure 30. Simulated relative power shifts of all six FMF modes for bending in two directions.

In addition to simulating the SMF-MCF-FMF chain, the simulation of the photonic lantern was also done. The photonic lantern device made in FimmWave consists of a six core fiber with differently sized cores, which is tapered down into a single FMF, as shown in Fig. 31. While the real PL will be made with six separate fibers being fused together as opposed to a six core fiber, the differences in the resulting modes should be small.



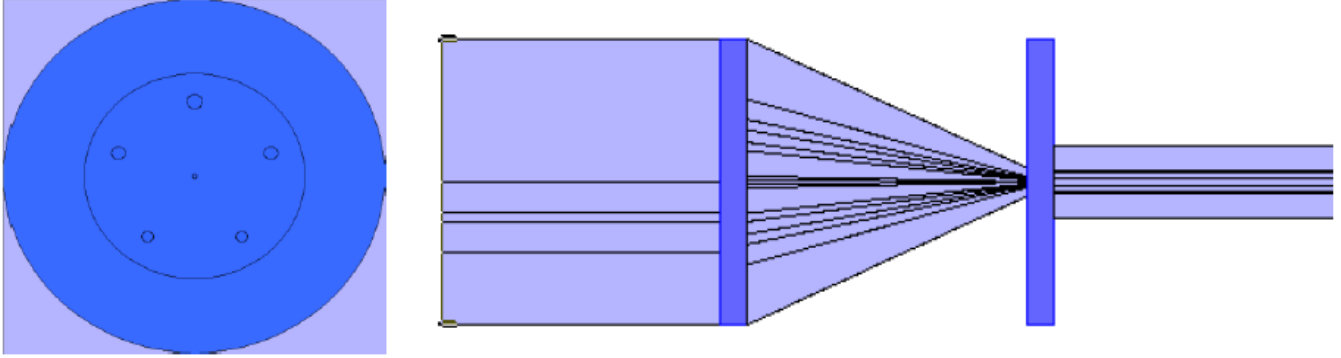


Figure 31. Model of six channel mode-selective PL, showing the cross-section of the six core fiber, and the tapered device.

Six different LP modes are then generated at the input of the FMF when exciting the six input fibers with SMF. Shown in Fig. 32 are the simulated modes from FimmWave obtained by exciting each SMF individually, clearly showing each of the expected LP modes of the FMF. Now that this PL has been simulated, it will be relatively simple to change the core sizes, tapering ratio, etc. in order to design new PLs in the future for sensing or other applications.

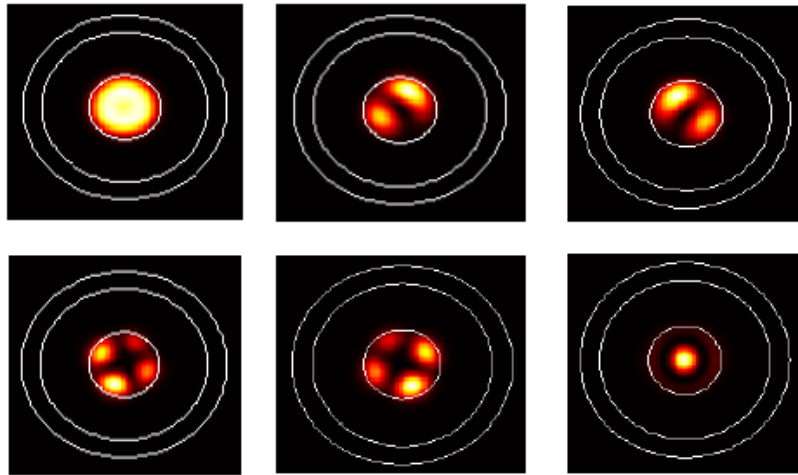


Figure 32. Simulated modes of a six mode PL in FimmWave.

One potential application of this combined MCF and PL device is multiplexing for multiple point measurements. This could be done by connecting the  $LP_{01}$  output SMF of one

device to the next input SMF in a chain, enabling the reconstruction of the full 3D shape of the fiber by using the remaining five modes of each device. A similar multiplexing technique was recently used with FBGs in cladding waveguides of a fiber [74]. That method requires a spectrometer, whereas the MCF with PL approach requires only a power meter as the interrogation system. In addition, it also has orders of magnitude higher sensitivity than the grating approach. This is the first time, to our knowledge, that a PL has been used for shape sensing applications. Our results show high sensitivity to bending over a wide range of radii of curvature, as large as 10 m, making this approach useful for applications requiring knowledge of the curvature and direction of bending for small curvature applications.

#### Direction-Sensitive Measurement with known Orientation

In the previous experiment, the orientation of the three core fiber was unknown. This limited our understanding of the direction-sensitive measurements and our ability to fully characterize the sensor. In order to improve understanding, the bending sensitivity of the three core fiber was explored in several directions in simulation in FimmWave.

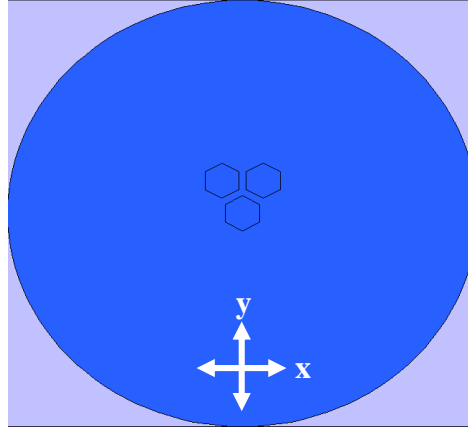


Figure 33. Orientation of three core fiber used in simulation.

The three core fiber was oriented so that the cores were symmetric about the vertical axis, as shown in Fig. 33. A 1.6 cm section of MCF between two SMFs was then bent by  $1^\circ$ , or a radius of curvature of about 0.9 m, in the  $\pm x$  and  $\pm y$  directions which are shown in Fig. 33. The transmission spectra obtained from this simulation are shown in Fig. 34.

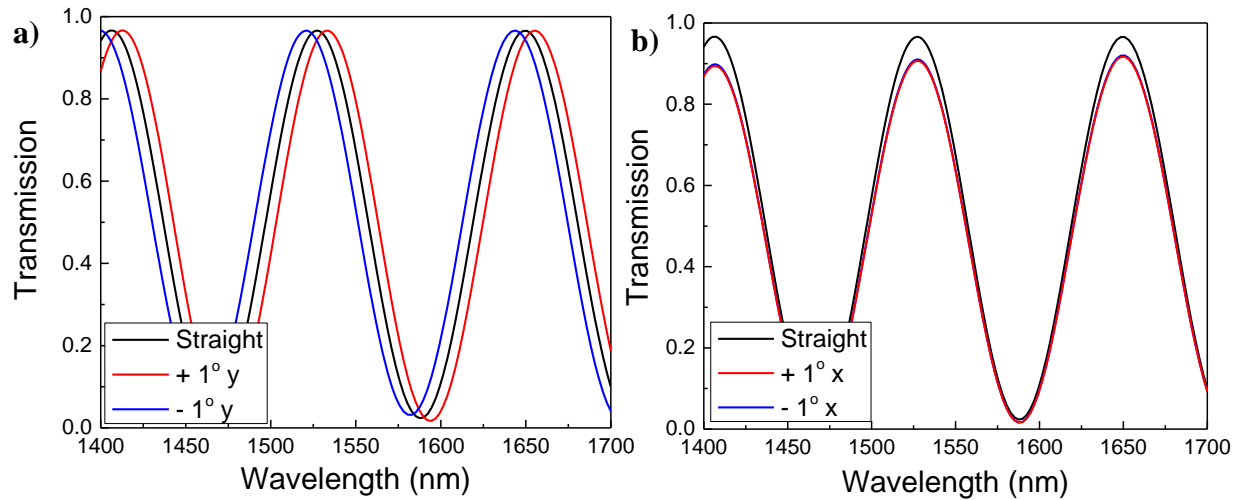


Figure 34. Transmission spectra of a three core fiber sensor being bent in the (a) y direction and (b) x direction.

These spectra show that when the three core fiber is bent in the y direction, the wavelength shifts with a sensitivity of about 6 nm/degree, and the shift is positive in the positive y direction, and negative in the negative y direction. In the x direction, there is no wavelength shift and only a decrease in total power for both directions. These results can be explained by looking at the supermodes of the three core fiber, shown in Fig. 27. When bent in the y direction, two of the supermodes will be directly affected by the induced refractive index change. When bent in the positive y direction, the upper two cores will be compressed, leading to an increase in the refractive index. When bent in the negative y direction, the upper cores will experience a strain and therefore a decrease in the refractive index. This is the cause for the opposite directions of the wavelength shift in transmission. When bent in the x direction, the index change is symmetric, meaning one of the upper cores will experience an index increase and the other a decrease. This averages out to no effective index change, and therefore no wavelength shift in transmission. The decrease in total power is attributed to simply the loss of some of the core light into the cladding of the fiber.

This measurement was performed in experiment by a colleague [81]. They made one major change to the setup, in that instead of splicing a second SMF to the end of the 3 core fiber, a flat cleave was used to reflect a small percentage of the light back through the MCF and input SMF, and the transmission spectra was then measured in reflection. This was done so that the facet of the MCF was exposed, and a camera could then be used to determine the orientation of the three cores.

The cores were arranged to match that shown in Fig. 33. The MCF was then bent in the same four directions, and the reflected spectra were measured. The results agreed fairly well with the simulation. For the y direction, there was a positive wavelength shift for the positive direction, and an equal and opposite negative shift for the negative direction. The sensitivity measured was less than that calculated in FimmWave, about 4 nm/degree as compared to 6 nm/degree, shown in Fig. 35. The most probable reason for this is the orientation of the cores. If the three core fiber was not exactly vertical, the asymmetry of the location of the two upper cores would cause a variation in the sensitivity.

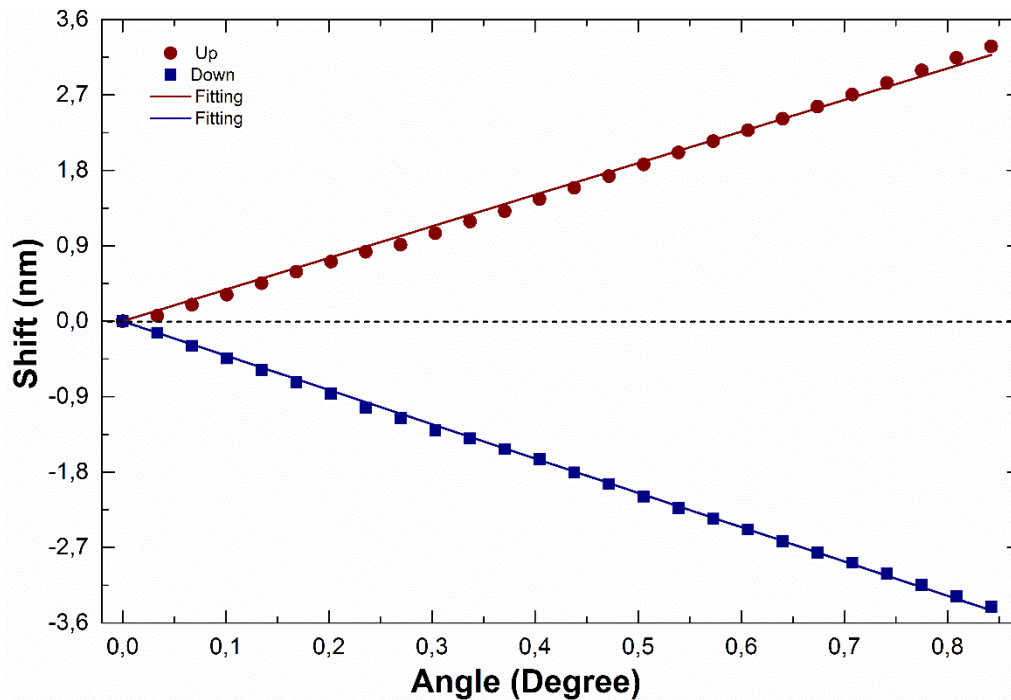


Figure 35. Wavelength shift measured for a three core fiber in the y direction [81].

For the x direction, minimal wavelength shift and a decrease in intensity was observed for the negative direction, similar to that found in simulation. In the positive x direction, the results differed and the intensity increased slightly, unlike the simulation. The assumed reason

for this is again the orientation of the three core fiber, or possible some other asymmetry in the experimental system, such as asymmetry in the drawn three core fiber or an offset in the SMF-MCF splice.

These results show a clearly direction-sensitive three core fiber sensor that can be easily understood and characterized. The stark differences between the changes in the transmission spectra for the four bending directions will enable simple measurements and calculations for both the bending radius and direction of curvature.

### Summary

The sensitivity of the MCF sensors has now been measured with respect to temperature, strain, and bending. From the many experiments, it was found that the MCF sensors can stably withstand temperatures of up to 1000°C and have higher temperature sensitivity than FBGs. It was also found that the MCF are more sensitive to strain than FBGs and that the sensitivity to an applied longitudinal force can be tuned through decreasing the MCF cladding diameter. Using two sensors with two different ODs enables the decoupling of temperature and longitudinal force measurements with a single transmission spectrum. Additionally, a mode-selective photonic lantern was integrated into the sensing setup, enabling high sensitivity direction-sensitive bending measurements, without the need for expensive spectral analysis equipment. A simpler bending experiment with the three core fiber showed clear directional dependence that can be easily understood and characterized.

### Air Hole Multicore Fiber

After optimizing the design of MCF for sensing, and characterizing the sensitivity of the sensors for several sensing applications, work has begun on designing a new fiber for increased sensitivity to pressure and acoustic waves. The new fiber will still be a MCF operating on the principle of supermode interference, however, it will also contain large air holes. Large air holes have been previously shown to increase the sensitivity of fiber sensors to pressure, as they allow for more deformation of the fiber than solid silica fibers [82–84].

### Design

Several initial designs were first tested in simulation using FimmWave. The designs use the hexagonal structure of the seven core fiber, but replace some of the cores with air holes. For instance, replacing three of the outer cores with air holes leaves four coupled cores to generate supermode interference, similar to the seven core fiber. Additional rings of air holes can be added around the cores as well. This design is shown in Fig. 36 (a). The supermode interference

was shown to be very similar to that of the seven core fiber, with two main supermodes excited, and a sinusoidal interference pattern in transmission, as shown in Fig. 36 (b).

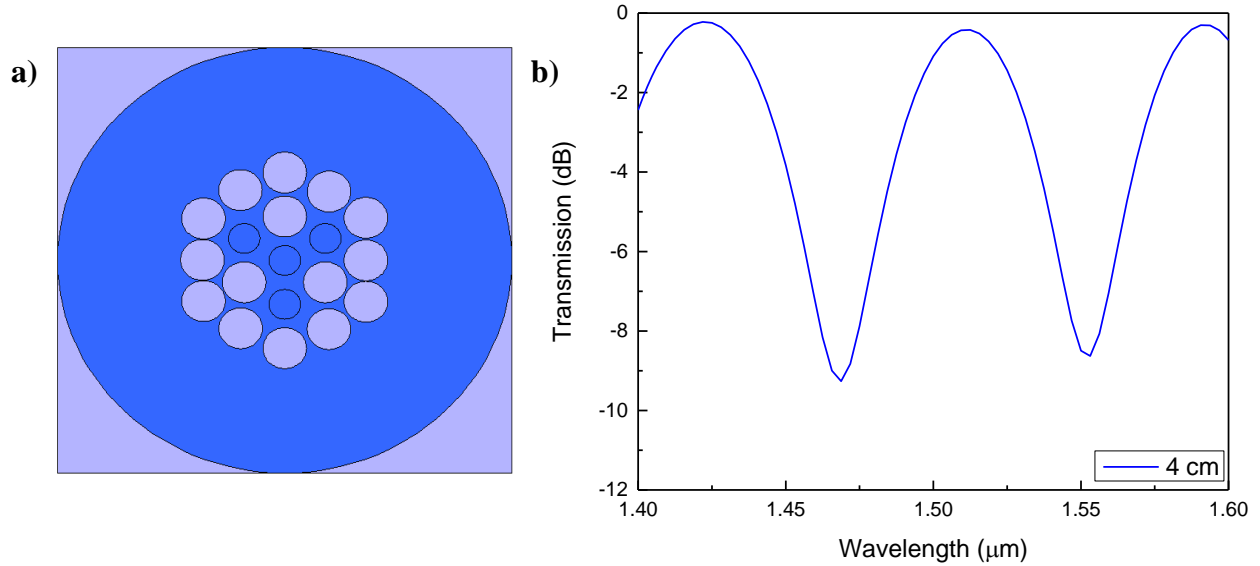


Figure 36. Design of MCF with 15 air holes and (b) its corresponding transmission spectrum from an SMS device.

The design with 15 air holes and four cores shown above was then stacked and drawn. The drawing parameters, namely the pressure applied to the air holes, was varied as the fiber was drawn in order to adjust the amount that the air holes were inflated. Four different bands of fiber were drawn with slightly different parameters: (1) 122μm OD, low pressure; (2) 128μm OD, high pressure; (3) 110μm OD, high pressure; and (4) 100μm OD, high pressure. The cross section of two of the bands are shown in Fig. 37. The higher pressure bands have a higher air to silica ratio, but also more deformed cores.



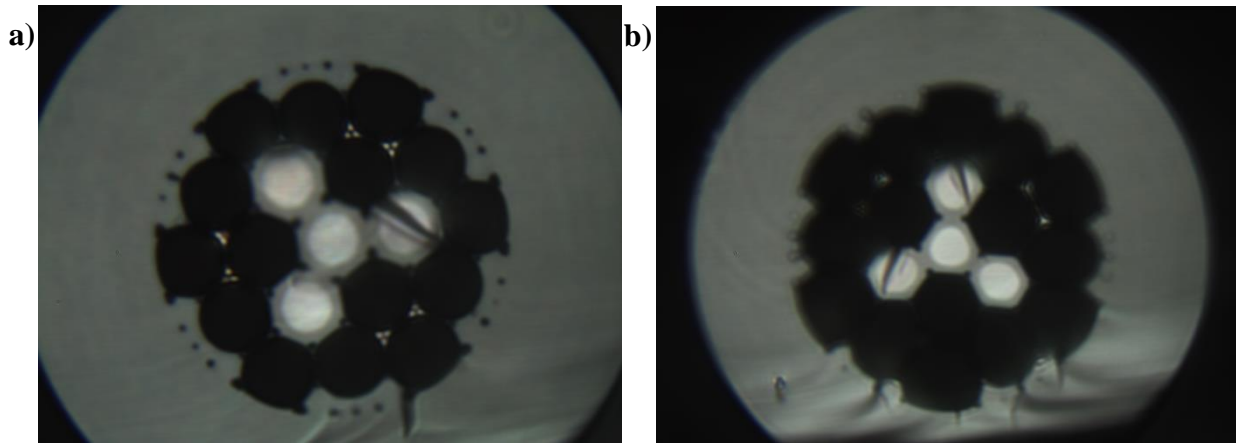


Figure 37. Cross-sections of drawn air hole MCF of (a) band one and (b) band four.

### Sensor Fabrication

After fabricating the fiber, splicing it to SMF was attempted in order to form SMS devices. First, the standard SMF-SMF program of an arc fusion splicer was used. However, because of the air holes, the alignment had to be done manually. Also, the temperature of the arc was too high, and the air holes of the MCF collapsed over several hundred microns, as shown in Fig. 38.

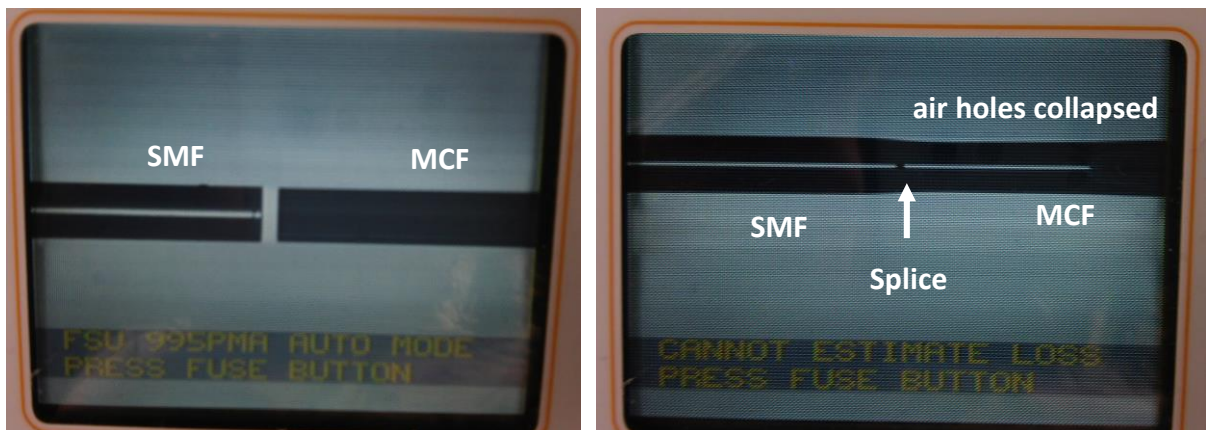


Figure 38. Images of SMF and air hole MCF before and after splicing with SMF-SMF program of an arc fusion splicer.

Splicing was then attempted using a CO<sub>2</sub> laser splicer. This splicer allowed for full control of the program parameters, as well as automatic alignment. In order to keep the air holes from collapsing, the power of the laser was decreased from the standard SMF program level, until the air holes appeared to be unaffected. Splices shown in Fig. 39 were obtained, showing relatively strong fusion, without any collapse.

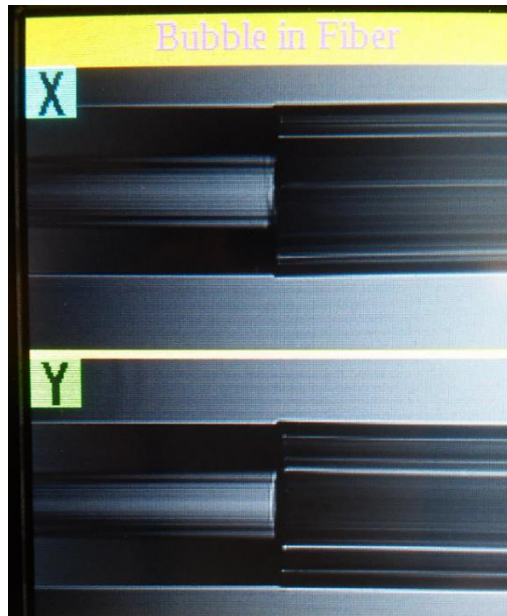


Figure 39. Images of SMF to air hole MCF splices from a CO<sub>2</sub> laser splicer after optimization.

However, while the splices appeared to be optimized, the MMI of the devices was very inconsistent, and most of the time there was almost no interference observed in transmission. As is clear from comparing Fig. 36 to Fig. 37, the model in FimmWave does not exactly match the drawn fiber. This is because the initial model was based on the design of the fiber stack, and not on the drawn cross-section. During drawing, the air holes were significantly inflated, leaving only a small ring of cladding around each of the four cores. The model was adjusted to more closely approximate the drawn fiber. As shown in Fig. 40 (a), each core has a small ring of

cladding around it, while the area surrounding the cores is air. The SMF-MCF-SMF chain was then created and the transmission spectrum is shown in Fig. 40 (b). While it still shows the expected sinusoidal transmission spectrum from the interference of two supermodes, the period of the interference is much wider than that obtained from the previous model. This is due to the air separating the cores, which decreases the coupling between them. Figure 40 (b) shows the spectrum of a typical device length, 2 cm, which has a period of about 400 nm. When testing the spliced devices, the wavelength range measured is usually narrower than this, which explains why the expected MMI was not observed.

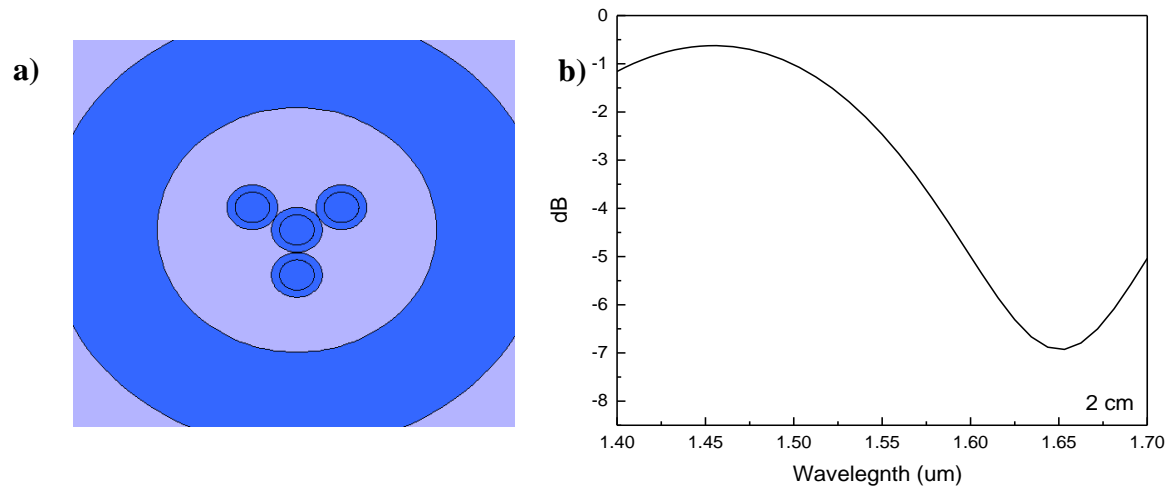


Figure 40. Cross-section of new air hole MCF model and (b) transmission spectrum of the SMS device for a typical MCF length.

When splicing longer sections of the air hole MCF between SMF, decreasing the MMI period [63], the MMI became clear within the spectral region being measured. With band one of the fiber, very long device lengths, on the order of 20 cm, were needed in order to have several interference minima within the spectral range measured (1450-1650 nm). Band three, with higher

pressure and a smaller OD, had stronger coupling between the cores, and showed several minima with the spectral range of interest with lengths of 5-10 cm. This device length is more compact and simpler to implement as a sensor, so band three was selected for making the initial devices. Figure 41 shows some example spectra obtained from the SMS devices using band three of the air hole MCF. The supermode interference is clear and sinusoidal, but is much less strong than the all-solid MCF, with minima depths on the order of 5 dB.

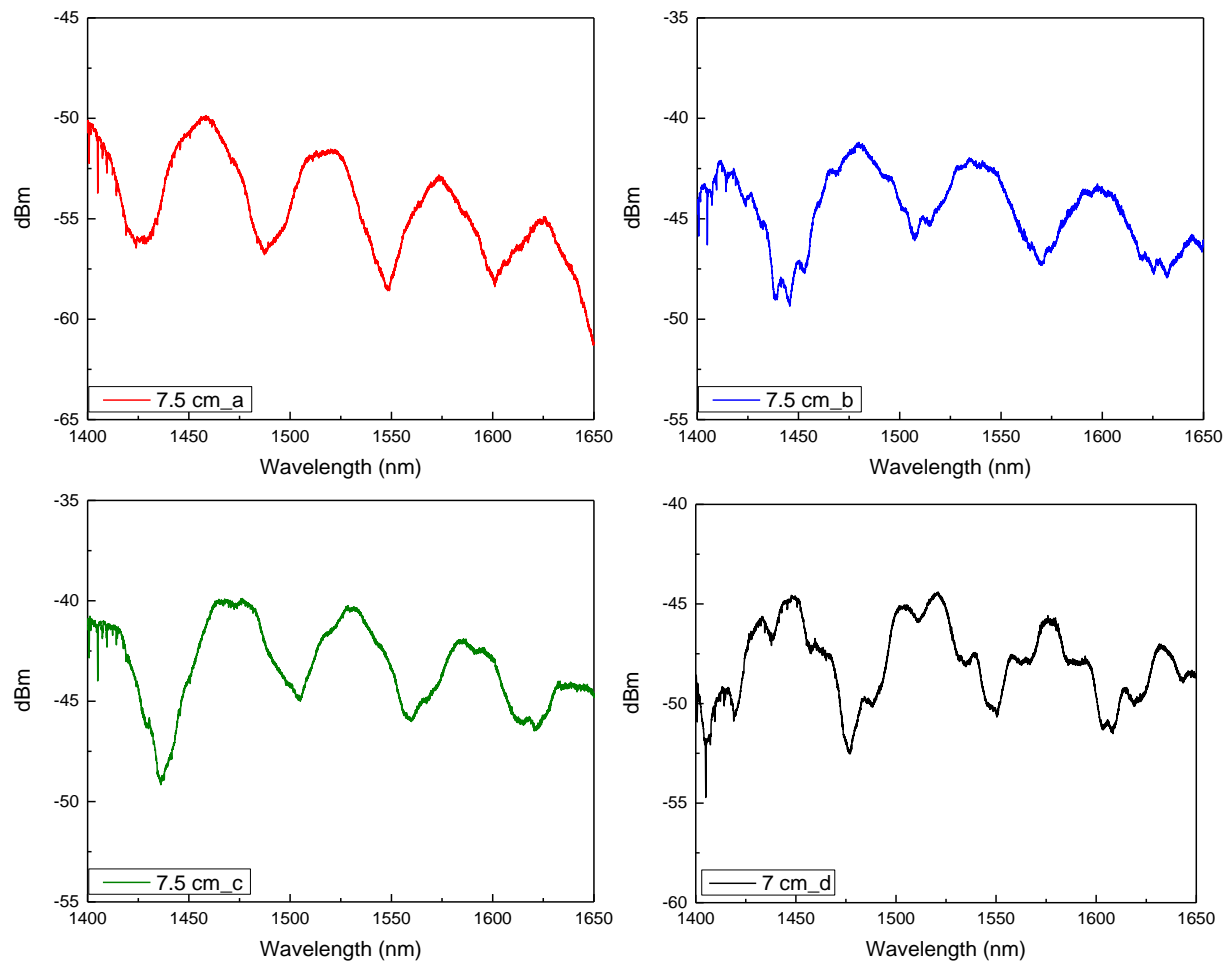


Figure 41. Example spectra of SMS devices made with band three of the air hole MCF.

The splice loss was measured for three of the band three devices and the average loss per splice was measured to be 1.4 dB. While not as low as the solid MCF, this loss is still suitable for an SMS device being used as a sensor.

## Sensitivity Measurements

### Bending

While the main purpose of the air holes in the MCF is to increase the sensitivity to pressure, other sensing experiments were attempted with the band three devices to compare their sensitivity to the solid MCF. First, the sensitivity of the air hole MCF to bending was tested. The same plastic tube and translation stage setup from the previous bending tests was used. The first observation made was that the MMI of the air hole MCF devices is extremely sensitive to any small changes. When bent to the same radius of curvature as previous tests with solid MCF, the MMI changed completely and could not be tracked. Very large bending radii were measured, and smoothing was applied to the measured spectra in Origin in order to be able to accurately track the MMI as the MCF was bent. Shown in Fig. 42 is the shifting spectra, unsmoothed and smoothed. As shown, the MMI did in fact shift with bending, but was impossible to track without significant smoothing.

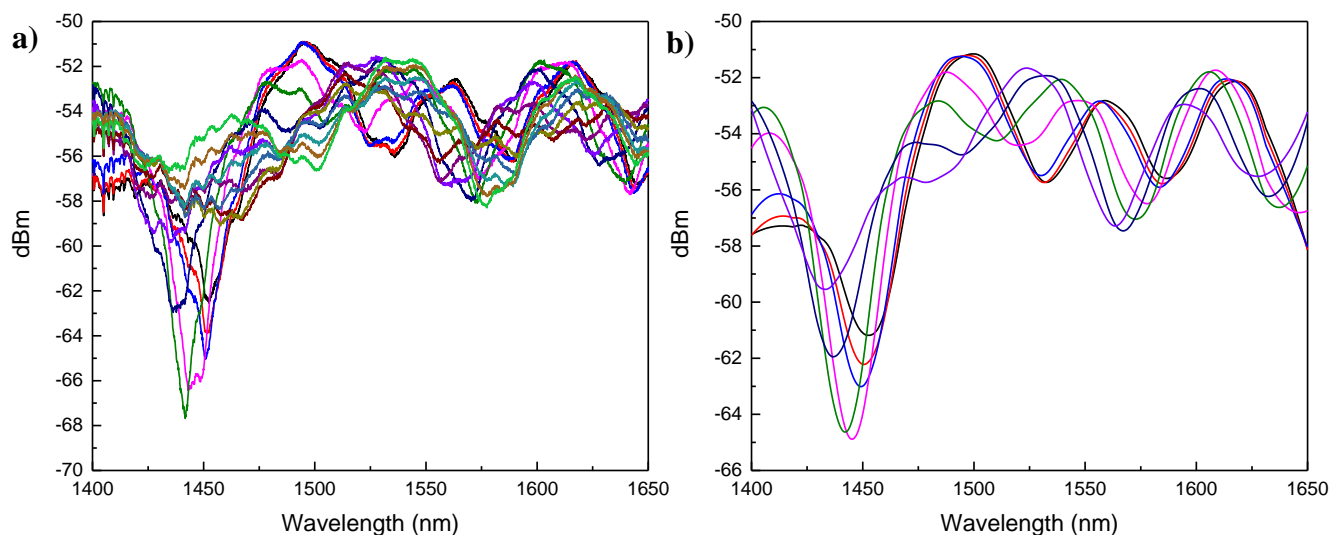


Figure 42. Transmission spectra of an air hole MCF device as it is bent, (a) unsmoothed and (b) smoothed.

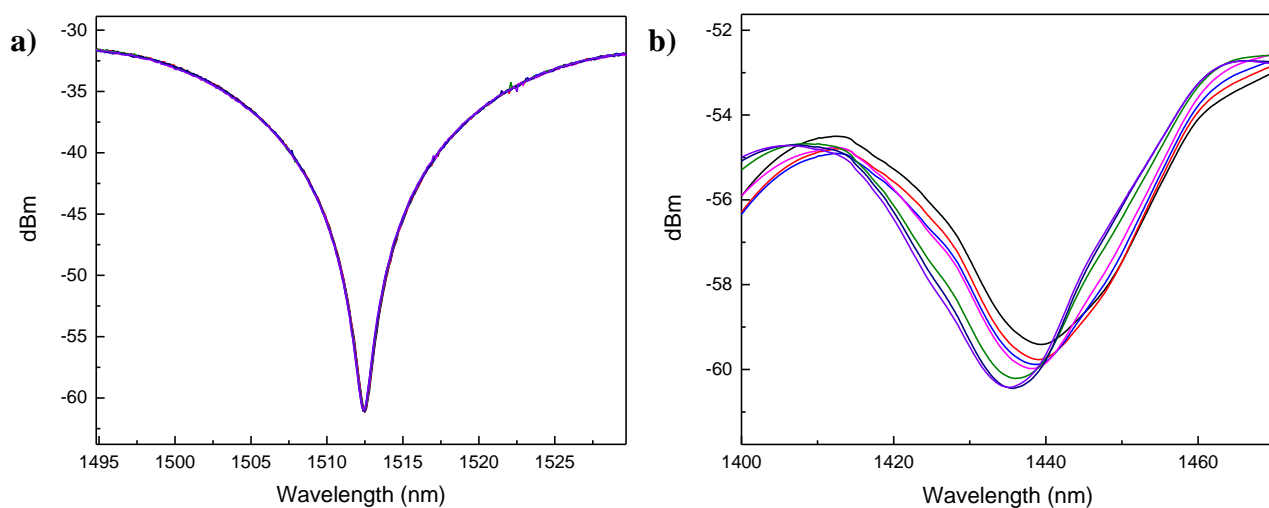


Figure 43. Transmission spectra of (a) solid MCF and (b) air hole MCF devices as they are bent to a radius of 85 cm.

In order to directly compare the sensitivity of the solid and the air hole MCF to bending, two sensors were tested together over the same range of bending radii. Figure 43 shows a focus on one MMI minima for each sensor as they are bent from straight to a radius of 85 cm.

While the spectrum of the solid MCF is much clearer than the air hole MCF, the sensitivity of the air hole MCF is about 50 times higher than the solid MCF.

## Temperature

Next, the sensitivity of the air hole MCF to temperature was measured using a hot plate. The main difficulty of this experiment was the relatively long length of the sensor. The hot plate does not have a uniform surface temperature, so the whole length of the 8 cm sensor was most likely not experiencing the same temperature. To help with the temperature disparities across the hot plate surface, the sensor was placed in a glass tube, which was then held between metal plates on the hot plate surface. A temperature sensitivity was measured, but was not repeatable or linear. The sensitivity measured is approximately the same as that of the solid MCF in this temperature regime,  $\sim 20$  pm/ $^{\circ}$ C, as shown in Fig. 44.

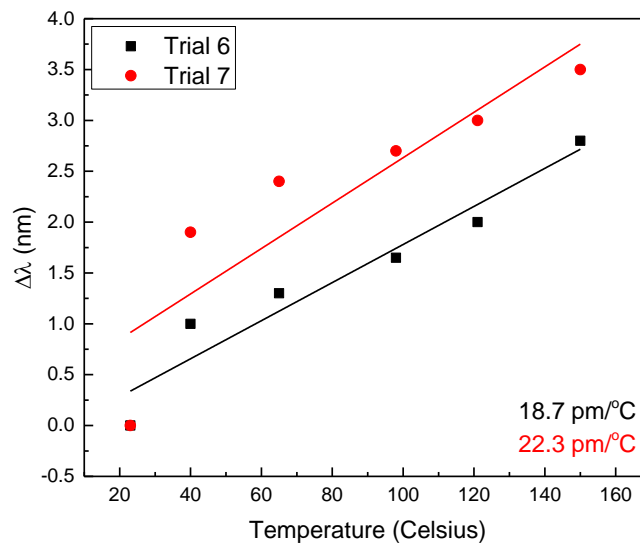


Figure 44. Air hole MCF sensor response to temperature for two different trials.

## Strain

In addition to temperature and bending, the sensitivity of the air hole MCF was tested with respect to strain. In a setup similar to that shown in Fig. 17, one of the air hole MCF sensors was tested in comparison to an FBG. Similarly to the bending measurement, the spectra needed to be smoothed in order to be tracked in wavelength. The smoothed spectra measured as strain was applied to the air hole MCF is shown in Fig. 45. The measured sensitivity compared to the standard FBG is shown in Fig. 46. The sensitivity of the air hole MCF is about three times higher than the FBG. However, the solid seven core fiber previously measured had a sensitivity of a about  $-2.24 \text{ nm/m}\epsilon$ , so the addition of the air holes in the MCF only increased the strain sensitivity by about 50% over the solid fiber.

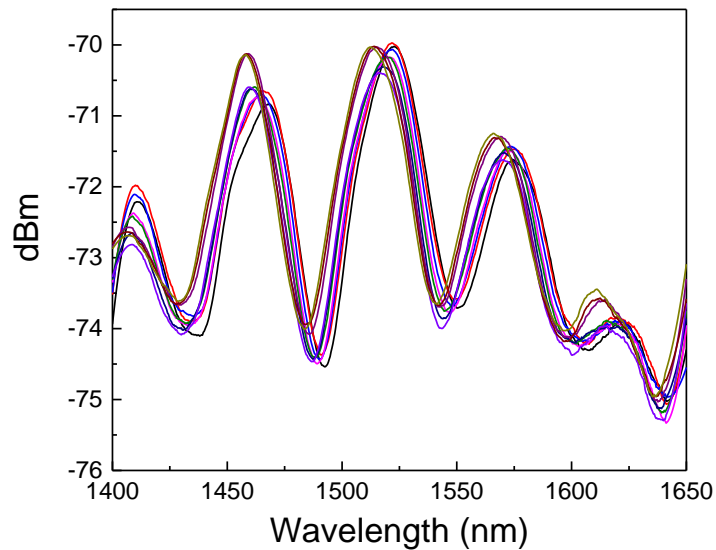


Figure 45. Smoothed transmission spectra of an air hole MCF sensor as strain is applied.



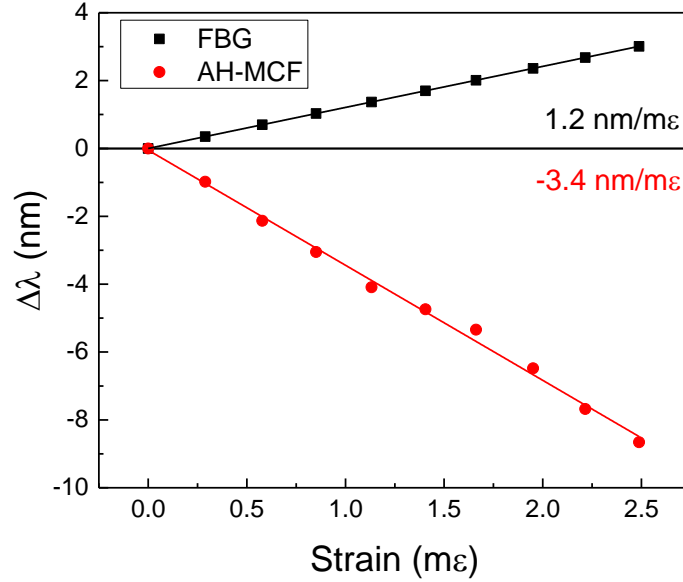


Figure 46. Measured wavelength shift of an air hole MCF sensor and an FBG.

## Pressure

As mentioned initially, the main goal for this fiber is to increase the sensitivity of the MCF to pressure, so the next step for these sensors is to test their response to pressure and acoustic waves. A controlled pressure setup is currently being developed. The sensitivity of the air hole MCF will be compared to that of the solid MCF. If the sensitivity of the air hole MCF is in fact significantly higher than the solid fiber, as it is expected to be, new designs with increased air/silica ratios may be tested in order to maximize the sensitivity of the device to pressure.

Additionally, these devices are being tested in an acoustic tank. A sound wave is a periodic change in pressure. This pressure applied to the MCF device will cause the spectrum to shift, due to changes in the refractive index and length of the MCF. If a narrow wavelength light

source is used, the amount of light that is transmitted will modulate along with the acoustic wave. This is because the laser wavelength is stable, while the transmission spectrum from the MCF will be modulated in wavelength. Therefore, if the laser light that is transmitted by the MCF is observed on an oscilloscope or an electrical spectrum analyzer (ESA), the amplitude will be modulated with the frequency of the sound wave.

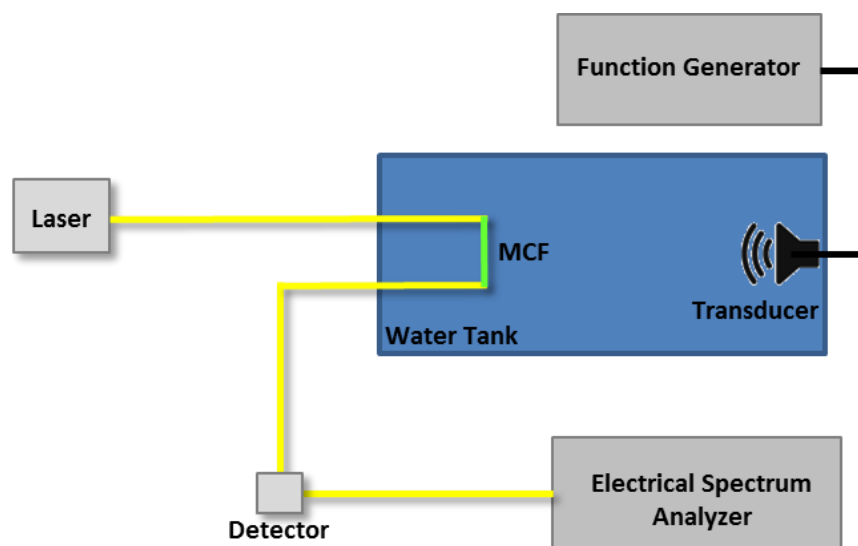


Figure 47. Experimental setup for measuring sensitivity of MCF to acoustic waves.

A setup for measuring acoustic sensitivity of the MCF has been developed and initial testing has begun. The current setup is shown in Fig. 47. A tunable laser (1525-1610 nm) is used as the source, enabling different points along the sensor's interference pattern to be chosen and compared. The sensor is submerged in a water tank whose inner walls are covered in a sound absorbing material in order to minimize reflections of the sound waves. A function generator is connected to a transducer that is placed in the tank. The transmitted power through the sensor is measured with a photodetector that goes into an ESA.

Initial results with this setup and the solid seven core fiber have shown strong acoustic sensitivity, but with low stability and repeatability. Shown in Fig. 48 is the signal amplitude from the ESA, as the function generator is tuned from 10-90 kHz. Up to 45 dB signal to noise ratio is observed, however, these results varied drastically from sensor to sensor, and also with the position of the MCF in the tank.

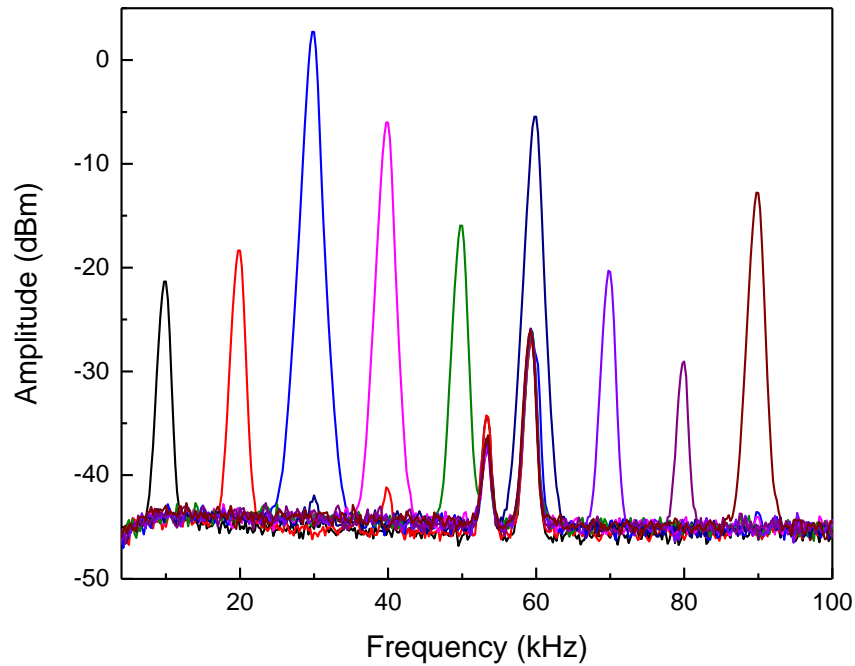


Figure 48. ESA signal of solid MCF response to acoustic waves tuned from 10-90 kHz.

Initial measurements have also been performed on an air hole MCF sensor. The sensor used was made from band three of the fiber with a 10 cm length. The spectra of the sensor when measured flat on the table as well as when in was mounted in the acoustic setup are shown in Fig. 49. Clearly, the high bend sensitivity of this sensor caused the spectrum to change when placed in the mount, however, there is still sufficient MMI present for testing the acoustic sensitivity.

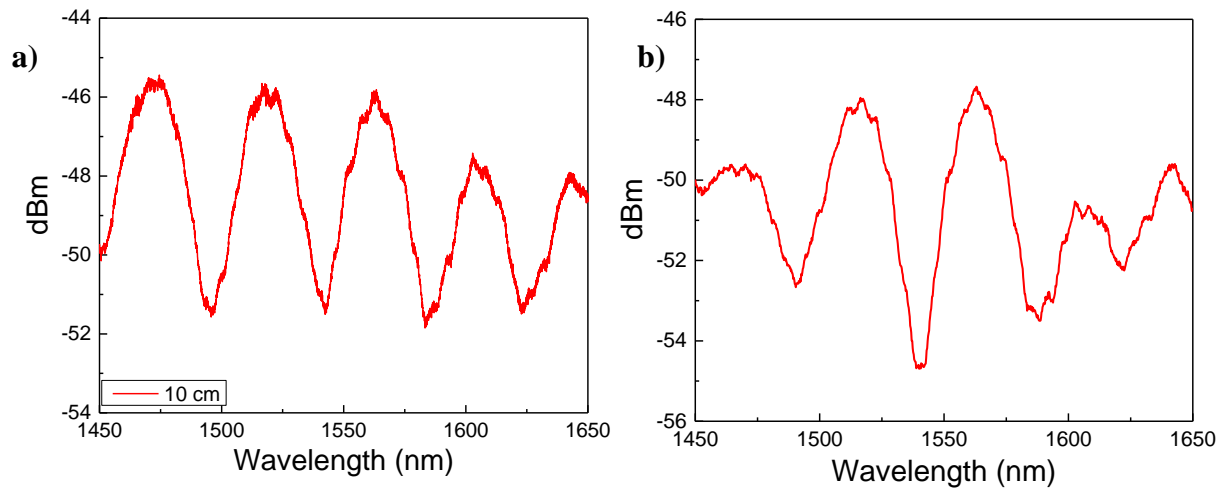


Figure 49. Transmission spectra of 10 cm air hole MCF sensor measured flat on the table (a), and in the acoustic mount (b).

Tests were performed on this sensor as the frequency was scanned throughout the range of the transducer, and the wavelength was scanned throughout the range of the OBR. When reading the signal on an oscilloscope, a high amplitude signal was measured at the frequency of 14 kHz. 96 mV peak to peak, as shown in Fig. 50 is approximately seven times higher than any signal ever measured with the solid seven core fiber sensors. This is an extremely promising result, as the amplitude of the MMI slope of the air hole MCF is about five times lower than that

of a solid MCF sensor. If the air hole MCF was optimized in design and splicing so that the MMI was comparable to that of the seven core fiber, the sensitivity would be expected to be one to two orders of magnitude higher for acoustic measurements.

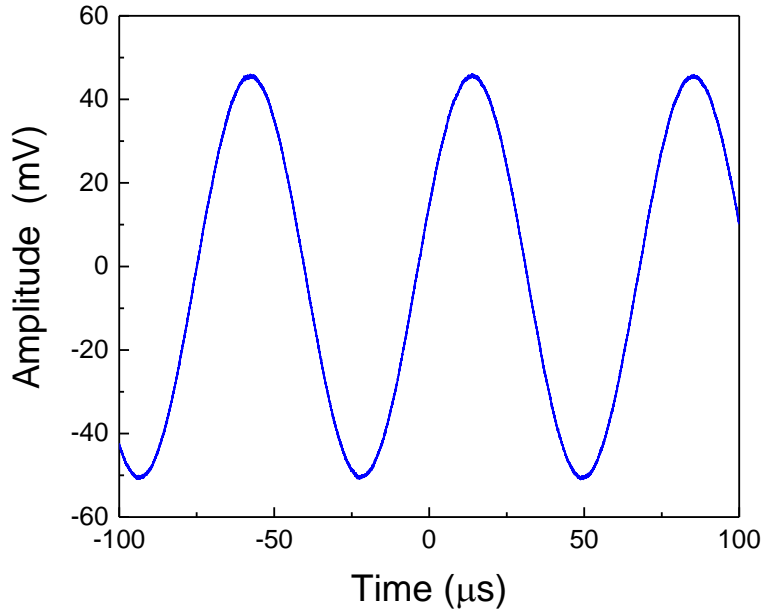


Figure 50. Amplitude signal from the air hole MCF on an oscilloscope when excited by a 14 kHz wave.

The tank setup, as well as the sensor mount, need to be further investigated in order to understand the inconsistencies previously observed. With a more robust setup, the solid and air hole MCF sensors can be more directly compared, and the sensitivity improvement caused by the addition of the air holes could be better understood. Additionally, the dependence of the ratio of silica to air in the air hole MCF can be explored with various designs of MCF.

### Summary and Outlook

As shown, MCFs in SMS sensors have been extensively explored. The design of the MCF was analyzed in depth in simulation, and the optimal design for mode matching to standard SMF was developed. Varying the number of cores in the MCF allowed for better understanding of the MMI and polarization effects. The critical aspects of the design for high overall transmission and sharp spectral features for a given wavelength range are now understood, and can be tuned for different wavelengths or for different SMFs for other applications. It was also determined that the sensors can be fabricated simply, inexpensively, and reproducibly when two students fabricated and characterized 126 sensors in two days, as part of a contract deliverable.

In addition to optimizing the design of the sensors, their sensitivity to various measurands was also explored in depth. It was found that the MCF sensors could stably measure temperatures up to 1000°C and had a higher temperature sensitivity than standard FBGs. This, coupled with their inexpensive fabrication and compact size, make the sensors very attractive for industries with harsh environments.

The MCF sensors were tested for their sensitivity to strain, and directly compared to FBGs. They were found to be 40% more sensitive to strain than FBGs. It was also found that the sensitivity to applied longitudinal force was dependent on the MCFs OD, and a sensitivity increase of a factor of seven was achieved through etching away some of the cladding of the MCF. Decoupling of temperature and longitudinal force measurements was achieved by using two MCF sensors with two different ODs and a single transmission spectrum.

The MCF fiber was also found to be sensitive to bending. In order to be able to measure both the radius of curvature of the bend and its direction, a three core fiber replaced the seven core fiber because of its asymmetry. A developing fused fiber device, mode-selective photonic lantern, was used in conjunction with the MCF sensor in order to eliminate the need for expensive spectral analysis equipment in the interrogation of the sensor. These tests showed both high bending sensitivity as well as direction sensitivity, only using a power meter as the interrogation instrument. A simple experiment with the same three core fiber was able to show clear and easy to characterize direction sensitive bending measurements, with good agreement to simulation.

Finally, a new design of MCF was explored for potential applications of pressure and acoustic sensing. This fiber, in addition to four coupled cores, has many large air holes surrounding the cores. This increases the deformability of the fiber and should increase the sensitivity of the MCF to pressure. Fiber was designed and drawn, and initial sensors were made. Bending experiments showed extremely high sensitivity when compared to the solid seven core fiber, but with much less clear MMI. An initial acoustic test also showed significantly higher sensitivity when compared to the solid MCF, but instabilities in the current setup haven't allowed for reproducible direct comparisons between the two sensors.

In conclusion, an inexpensive and simple to fabricate sensor based on MCF has been developed and extensively tested. This sensor has similar operation to standard FBGs, but with higher sensitivity and a much higher temperature limit, making it suitable for many applications. A new design has shown strong potential for greatly increasing the MCF sensitivity and may be

able to further expand its possible applications. Because of the great potential demonstrated here, this fiber sensor design has been patented by UCF [85]. Also, a start-up company, Multicore Photonics, is in the process of commercializing the sensor, which includes making packaged prototypes and introducing the MCF devices to industries where they could potentially have a large market.



## **CHAPTER 3: HOLLOW CORE FIBER**

Hollow core fibers (HCF) are optical fibers that guide light in an air core, as opposed to a solid material, such as glass. Instead of total internal reflection, HCF uses alternate guiding mechanisms such as the anti-resonant [86–90] or photonic bandgap effects [91,92]. HCFs based on the anti-resonant effect are quickly gaining attention for their excellent guiding properties, such as low loss and wide transmission windows [89]. While the first generation of HCFs were based on band-gap supported light guidance [92], anti-resonant HCFs (ARHCFs) achieve low propagation losses due to the strong suppression of coupling between the core modes and any available mode in the surrounding of the core [89]. Only around specific resonance wavelengths, strong coupling to outside modes leads to significant propagation losses of the core modes. Various ARHCF designs have been investigated in both simulation and experiment in an attempt to reduce the overall attenuation and bend-induced losses as well as to shift the resonance wavelengths and provide customized ranges of high transmission [86–88,90,93,94].

### Sensing with Hollow Core Fiber

In addition to a wide variety of other applications, HCF can also be used for sensing. Specifically, gas sensing is possible within these fibers' cores. We are currently involved in a project with Mesa Photonics, LLC, who are working to make a compact Raman air sensor for NASA to be used in future astronaut suits. HCF will be used to measure the gases present in the suits. Current commercial HCFs based on the photonic bandgap effect have small core sizes on

the order of 5  $\mu\text{m}$  and limited transmission window bandwidth. Our goal is to first fully characterize and optimize Mesa's current system, and then to design a new HCF that will better meet their needs.

Currently, Mesa is using a commercial HCF from NKT Photonics, which has a small core size of 6.6  $\mu\text{m}$  and a small transmission window around 580 nm. The facet image and measured transmission spectrum of this fiber are shown in Fig. 51.

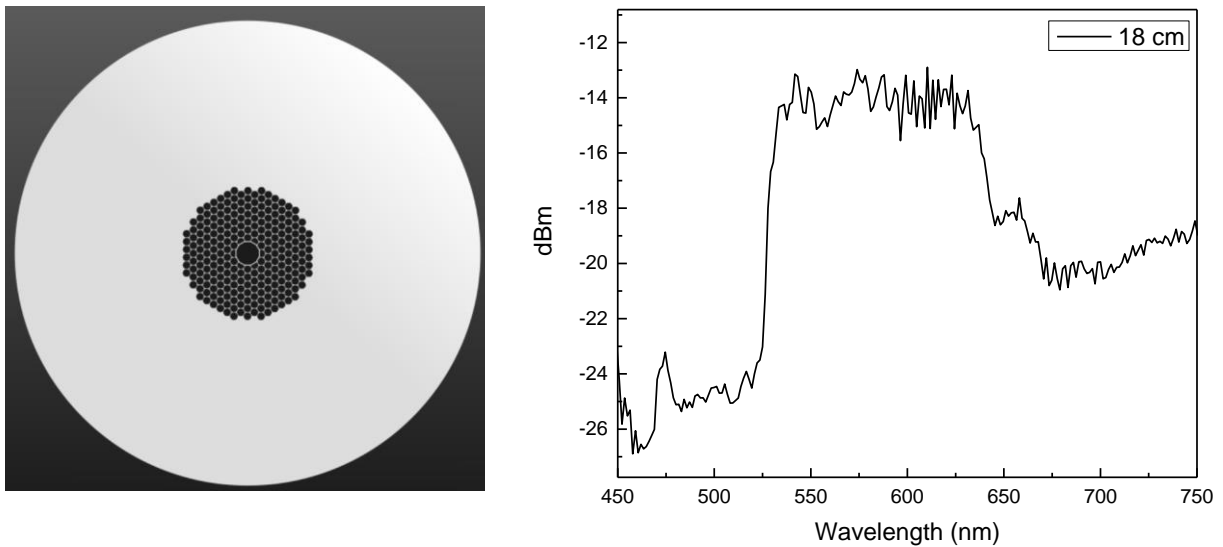


Figure 51. Facet image and transmission spectrum of 18 cm of commercial HCF NKT 580.

Mesa is currently using a 532 nm diode laser and is attempting to measure several common gases with detection wavelengths ranging from 570-660 nm, as shown in Table 1. The commercial fiber being used only has high transmission in the window from about 530-630 nm, limiting the range of gases that can be measured.

Table 1. List of gases and their detection wavelengths for Mesa's Raman air sensor.

Species	Stokes shift (cm-1)	Detection wavelength (nm)
Carbon dioxide (CO <sub>2</sub> )	1285.5 & 1388.3	571.1 & 574.4
Oxygen (O <sub>2</sub> )	1554.7	580.0
Nitrogen (N <sub>2</sub> )	2330.7	607.3
Methane (CH <sub>4</sub> )	2914	629.6
Ammonia (NH <sub>3</sub> )	3334	646.7
Water vapor (H <sub>2</sub> O)	3651.7	660.3

We recently began fabricating and characterizing HCF in-house at CREOL. This HCF is based on the anti-resonant effect, meaning there are specific wavelengths where the light is resonant with the silica structure and does not propagate in the core. These wavelengths are determined by the thickness of the silica boundaries, shown in Eqn. 14:

$$\lambda_m = \frac{2t}{m} \sqrt{n^2 - 1} \quad (14)$$

where  $\lambda_m$  is the resonance wavelength,  $t$  is the silica thickness,  $m$  is the order of the resonance, and  $n$  is the index of refraction of the silica. Several different designs have been fabricated and the characterization is ongoing. For example, Fig. 52 shows a scanning electron microscope (SEM) image of a HCF with eight non-touching rings, each about 19  $\mu\text{m}$  in diameter, and a large air core of 70  $\mu\text{m}$ . The thickness of the rings is 1  $\mu\text{m}$ .

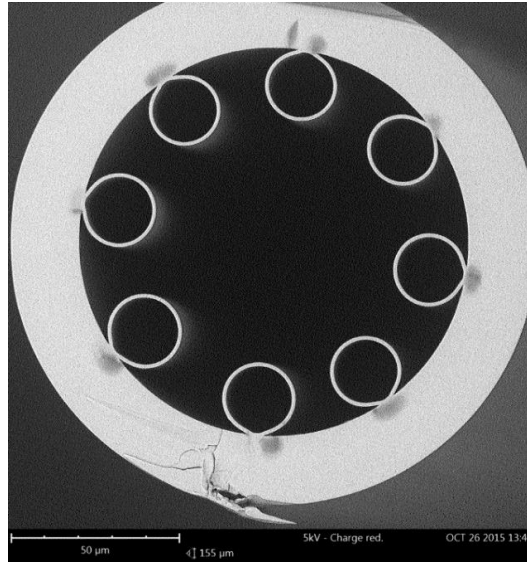


Figure 52. SEM image of a non-touching ring HCF, draw 347, band 2

The expected resonances from Eqn. 14 are approximately 2220 nm, 1120 nm, 750 nm, and 560 nm. The measured spectrum is shown in Fig. 53 and resonances matching approximately 1120 nm, 750 nm, and 560 nm are clearly visible. This fiber has a broad flat transmission window in the near infrared region, but little to no guidance in the visible. For the Mesa project, guidance around 500-700 nm is required, so the design will have to be altered in order to be able to use this HCF for that application. However, assuming the required silica thickness can be achieved, the transmission window should be much broader than that of the commercial HCF currently being used.

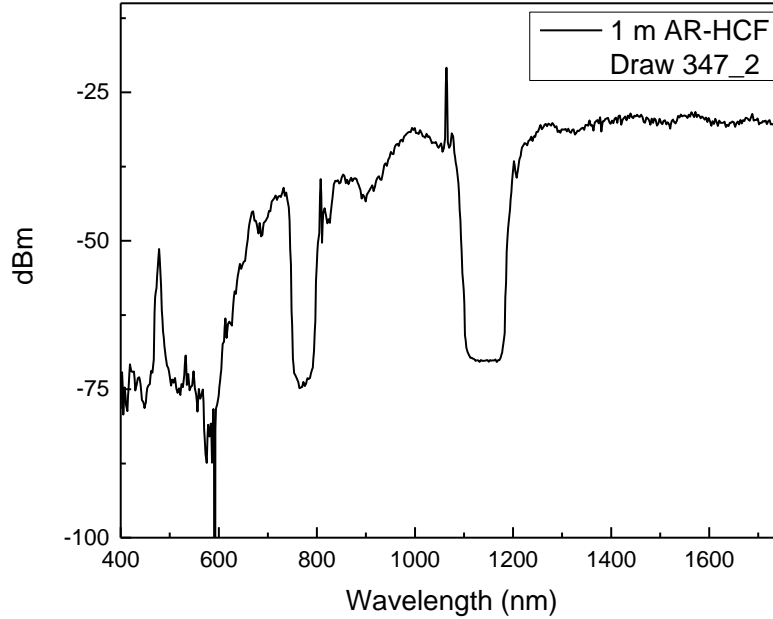


Figure 53. Transmission spectrum of non-touching ring HCF, draw 347, band 2.

In order to determine the optimal design of HCF for Mesa's application, COMSOL Multiphysics was used to model various HCF and their loss spectra. COMSOL was used in place of FimmWave due to the need for a highly adaptable mesh for this fiber, because of the contrast of the large core size compared to the very small feature size of the cladding elements. It had previously been found that an element size of  $\lambda/4$  was needed in the thin silica cladding elements in order to obtain an accurate simulation [90]. Additionally perfectly matched boundary layers were used in order to eliminate modes in the outer tube, and focus only on the core and cladding modes. The eight non-touching ring design was kept as the starting point, and the size of the rings and their thickness was varied until an optimal design was found. The final design for the Mesa HCF was 150  $\mu\text{m}$  outer diameter, 19.1  $\mu\text{m}$  ring diameters, 980 nm ring thickness, and a 70

$\mu\text{m}$  core size (measured between inner edges of two opposing rings). The fiber design and the loss spectra of this fiber are shown in Fig. 54.

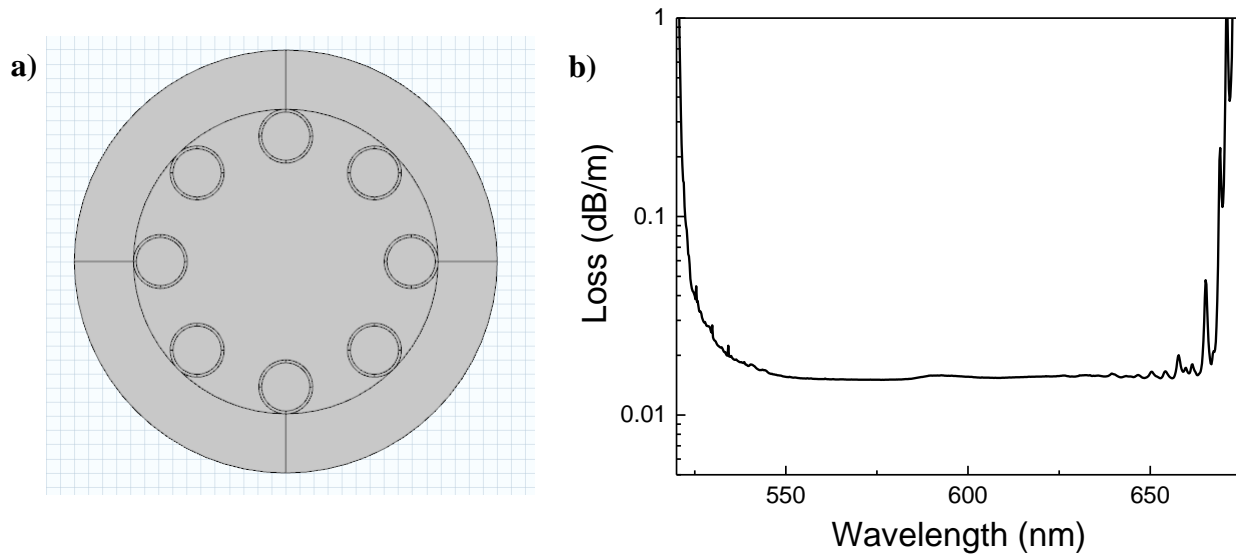


Figure 54. The COMSOL HCF design for Mesa (a) and its loss spectrum (b).

As shown in Fig. 54, the loss in the range from 530 nm – 660 nm is very low, less than 0.02 dB/m. The third and fourth resonances are located just outside of this range. While this design is clearly well-suited for the range required by Mesa, a different design with thinner rings would increase the fabrication tolerance. With thinner rings, for example 400 nm, the first resonance would be located at approximately 840 nm, and the second at 420 nm. This gives a wider transmission window around the required wavelength range, and therefore more tolerance on the thickness in fabrication.

### Loss in Hollow Core Fibers

The propagation loss of the HCF was measured in order to better understand and improve the fabrication processes. There are several causes of loss in ARHCF [89]. At the resonances, light is coupled from the core into the cladding, so the loss is extremely high at these wavelengths and gradually decreases as you move away in wavelength. Apart from the resonances, the theoretical fundamental cause of the core attenuation is leakage loss. Additionally, material absorption can also lead to loss, though the core light generally has very little overlap with the glass (as low as 0.01% [7]) so the effect of the material on the loss is generally low. In fabrication, however, imperfection loss is the dominating cause of the fundamental mode propagation loss. Imperfections refer to the non-uniformity of the structure, variation in the structure along the fiber, large nodes or flattened edges caused by too much fusion, or any other deformity in the fiber structure.

As ARHCF designs are currently being investigated, one of the main goals of new designs is to minimize the attenuation of the light in the fiber core. The first HCF to guide by the anti-resonant effect were Kagome fibers [102,103], which extended the transmission bandwidth and reduced the field overlap with the glass structure when compared to photonic bandgap fibers [104]. These fibers achieve low propagation losses due to strong suppression of coupling between the core modes and cladding modes. In order to increase the inhibited coupling between the core and cladding, a negative curvature, or hypocycloid, HCF fiber was developed in both simplified designs [105] and full lattice Kagome designs [106]. It was found that the core boundary shape has a strong influence on the guidance properties of all HCF, and its accurate

control is required in order to achieve low propagation losses [87,107–110]. In ARHCF, strong coupling to outside modes occurs around specific resonance wavelengths, and as these resonances are dependent on the thickness of the core wall, open boundary ARHCF were proposed in order to maintain constant core wall thickness and increase the transmission bandwidth over closed boundary designs [95].

In order to measure the propagation loss of the ARHCF, cutback measurements were performed. These measurements were performed with a supercontinuum source and an OSA. The HCF was excited through butt-coupling of the SMF of the light source to the HCF. While there is a large mismatch in core sizes of these fibers, the coupling loss was relatively low, and the signal to noise levels measured were more than sufficient for these measurements. The output of the HCF was then imaged on a charge-coupled device (CCD) in order to optimize the alignment. After aligning the input, the output light was then butt-coupled to the collection fiber (105/125) and connected to the OSA.

The transmission spectra were then measured as the ARHCF was cut down to shorter lengths. The power transmitted can be measured as a function of fiber length and a linear fit can then be applied to the data to calculate the loss at various wavelengths.

First is an example cut back measurement for an ARHCF with touching capillaries, forming a closed boundary core. The core is 48  $\mu\text{m}$  in diameter (measured between the inner edges of two opposing capillaries), the capillaries are 30  $\mu\text{m}$  along the long axis, the thickness of the capillaries is 770 nm, and the outer diameter of the fiber is 150  $\mu\text{m}$ , shown in Fig. 55.



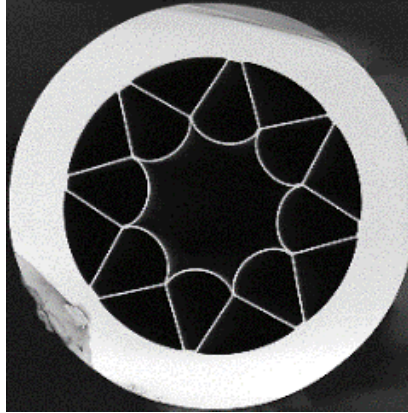


Figure 55. SEM image of an eight ring, closed boundary ARHCF.

Figure 56 (a) shows the transmission spectra measured for various fiber lengths. The loss at 1300 nm is shown in Fig. 56 (b) to be about 1.4 dB/m. This loss is fairly high and limits possible applications of this fiber that would need lengths longer than a few meters.

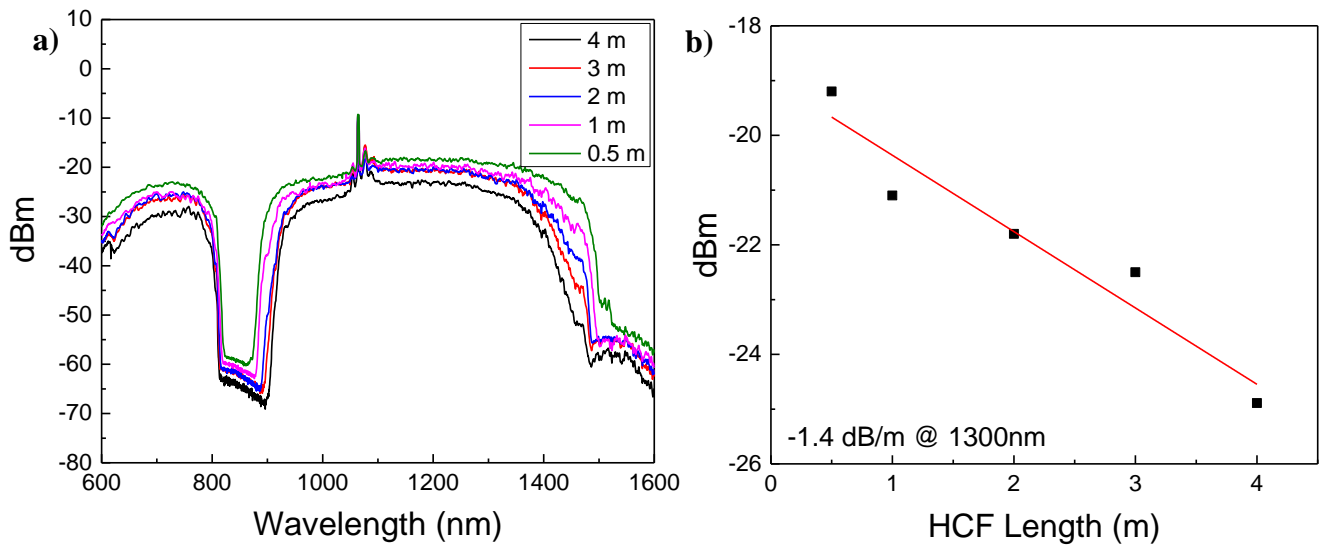


Figure 56. (a) Transmission spectra of various lengths of the eight ring, closed boundary core ARHCF, (b) calculated loss from the cutback measurement.

A second example cut back measurement is shown for an ARHCF with eight non-touching rings. As previously mentioned, the open boundary core leads to more uniformity and

control over the core wall thickness, which should lead to lower loss and narrower resonances. The fiber shown here, in Fig. 57, had a core of  $70\text{ }\mu\text{m}$  in diameter (measured between the inner edges of two opposing rings), rings with  $19\text{ }\mu\text{m}$  inner diameter and a  $1.2\text{ }\mu\text{m}$  glass wall thickness, and an OD of  $150\text{ }\mu\text{m}$ . The measured loss was approximately  $0.7\text{ dB/m}$  at  $1500\text{ nm}$ . This is half that of the closed boundary ARHCF. While the fusion at the boundary is not the only difference in the fiber geometries, it can be assumed that the improvement in the attenuation can be partially attributed to the change in boundary.

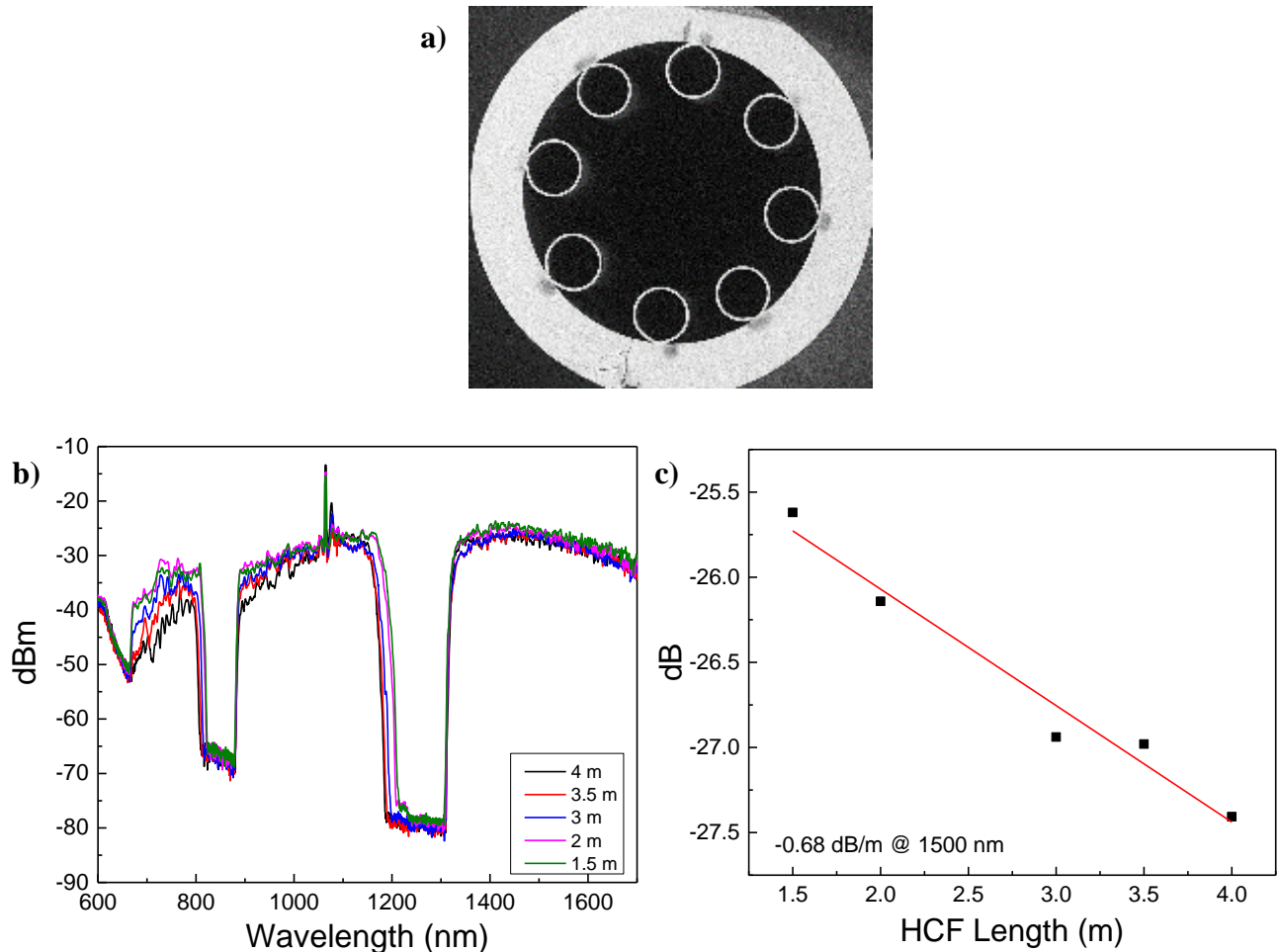


Figure 57. (a) SEM image of an eight ring, open boundary core ARHCF, (b) transmission spectra of various lengths, and (c) calculated loss from the cutback measurement.

Thirdly, an ARHCF with seven non-touching rings, with 150  $\mu\text{m}$  OD, 45  $\mu\text{m}$  core diameter, 18  $\mu\text{m}$  ring diameter, and 420 nm ring thickness was measured. The number of rings was reduced from eight to seven in order to increase the coupling of the higher order core modes into the cladding. The SEM image of this fiber is shown in Fig. 58, along with the measured transmission spectra, and the transmitted power as a function of length for two wavelengths, 750 nm and 1500 nm. The loss measured here, 0.4 dB/m and 0.6 dB/m, respectively, is again lower than the previous design, which may be attributed to the change in the number of rings.

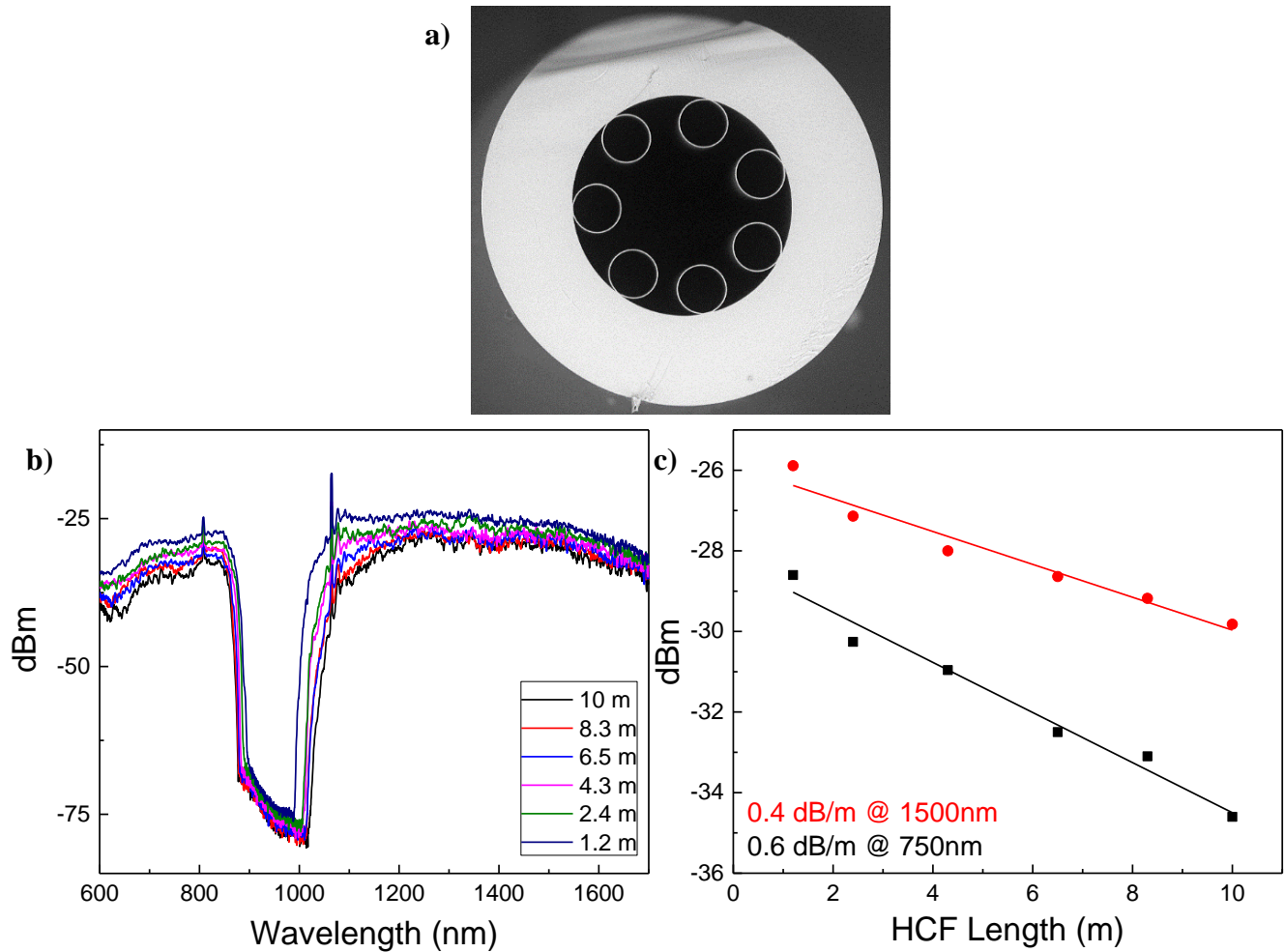


Figure 58. (a) SEM image of the seven ring, open boundary core ARHCF, (b) transmission spectra of various lengths, and (c), calculated loss from the cutback measurement.

Finally, a new design was fabricated and tested which has a nested structure. This refers to secondary capillaries within each of the cladding capillaries. An example design is shown in Fig. 59 (a) [86], and the SEM image of the fabricated fiber is shown in Fig. 59 (b). Obviously, the obtained fiber structure varies from the original design, but this fiber was still characterized for propagation loss. The measured spectra and corresponding loss is shown in Fig. 59 (c) and (d).

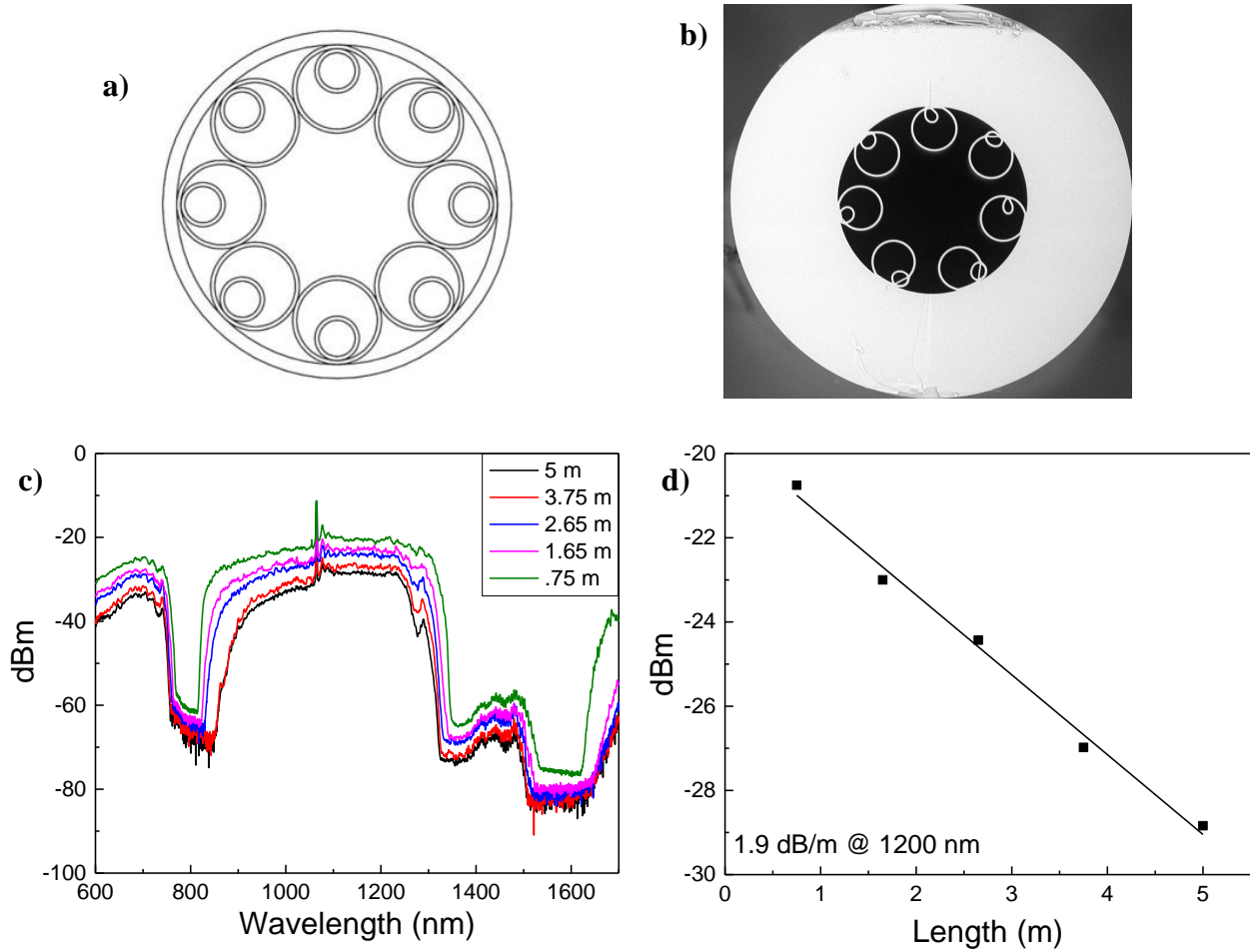


Figure 59. (a) Design of a nested ARHCF [86], (b) SEM image of a drawn nested ARHCF, (c) transmission spectra measured for various lengths, and (d) the calculated loss from the cutback measurement.

Due to the variation in structure, the loss measured was significantly higher than that measured for the previous non-nested structures, most likely due to the non-uniformity of the cladding elements.

In addition to variations in the design of the ARHCF, another factor in decreasing the propagation loss is the material used. All ARHCFs shown here have been fabricated with Quartz glass. This glass is inexpensive and low quality, and was used with the purpose of obtaining all necessary drawing parameters needed for fabrication of these different designs of ARHCF. Now that the fabrications steps and drawing parameters have been optimized, we will begin using a more expensive, higher quality glass material for all future draws. The increase in the quality of the glass material should reduce the attenuation that has been measured. A first draw with higher quality fused silica glass (F300 from Heraeus) showed an approximate loss of less than 0.1 dB/m over several hundred nanometers, but the length of fiber drawn was not enough to do an accurate cutback measurement.

### Mode Analysis of Hollow Core Fiber

While many of the ARHCFs' guidance characteristics have been studied in detail, the higher order mode (HOM) content has not been looked at in depth experimentally. They are generally assumed to be approximately single mode, mostly determined from camera images of the near field [95,96] or recently, through selective excitation of the HOMs [97]. Understanding the mode content of ARHCFs is crucial for their applications, which include high power delivery [98], UV and mid-IR transmission [95,96], sensing [99], nonlinear fiber optics [100],

and in-fiber gas lasers. Recently, a mid-IR gas laser around 3.1  $\mu\text{m}$  operating in both continuous wave and pulsed modes was demonstrated using two different ARHCFs inside the laser cavity [101].

Here we show an analysis on the mode content of two geometric designs of ARHCF. Using spatially and spectrally resolved imaging ( $S^2$ ), the number of guided modes as well as the distribution of power between them can be accurately measured [111,112].  $S^2$  uses both the spatial and the spectral interference produced by the propagation of multiple modes in FMFs to simultaneously image all of the supported modes and measure their relative intensities. This method has been used to measure passive and rare-earth doped large mode area fibers, few-mode fibers for space division multiplexing, photonic band-gap fibers, and more [113–116].

First, we examined a fiber with eight non-touching rings surrounding the air core. The core of the fiber is 70  $\mu\text{m}$  in diameter (measured between the inner edges of two opposing rings), the rings have a 19  $\mu\text{m}$  inner diameter with a 1.2  $\mu\text{m}$  glass wall thickness, and the OD is 150  $\mu\text{m}$ . The transmission spectra of 4 m of this fiber is shown in Fig. 60 (a), along with an SEM image of the fiber facet. Two resonances located at 850 nm and 1250 nm are clearly visible, corresponding to Eqn. 14.

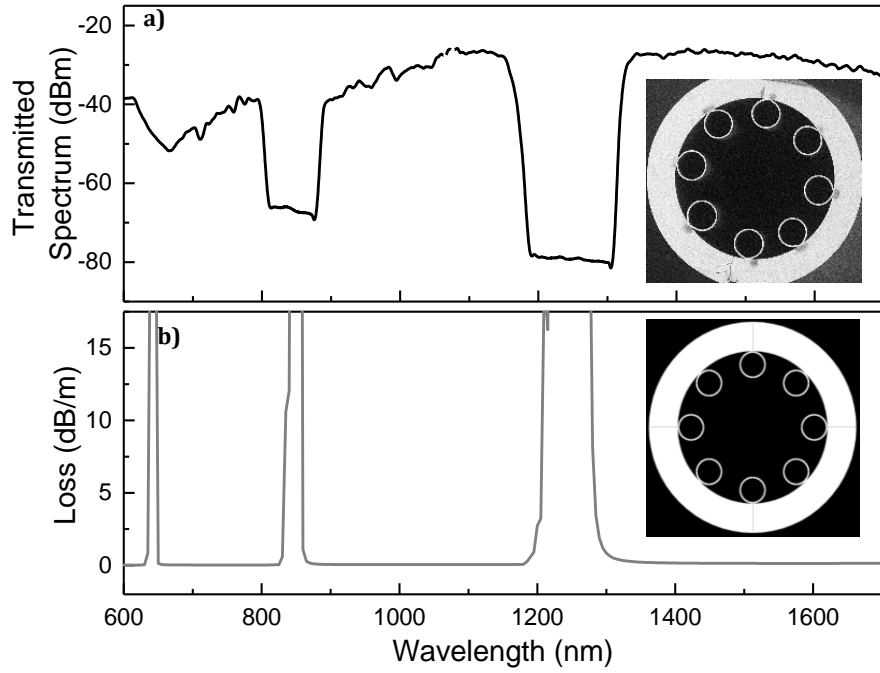


Figure 60. (a) Transmitted white light spectrum of 4 m of non-touching ring HCF with an SEM facet image. (b) Simulated loss spectrum from COMSOL with the fiber design inset.

Using a cut back measurement, a propagation loss of 0.68 dB/m was measured around 1500 nm. In order to verify the experimental results and gain predictive capabilities, simulations were performed using COMSOL Multiphysics. The non-touching ring fiber was created, shown in the inset of Fig. 60 (b), and the loss spectrum of its fundamental mode was calculated. The calculated loss spectrum is presented in Fig. 60 (b), beneath the measured transmission spectrum of the fiber. Clearly, the resonances appear at the same locations, corresponding to the wall thickness of the rings.

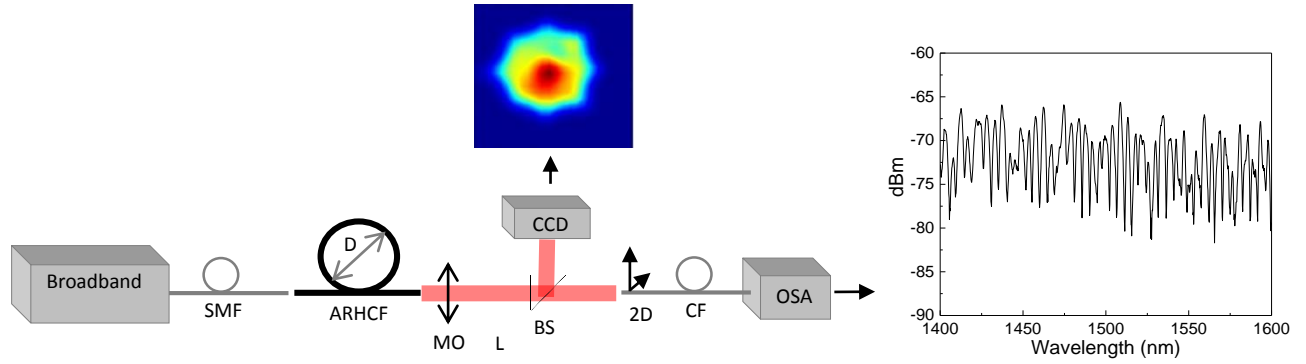


Figure 61. Experimental setup used for  $S^2$  measurement. An example near field of the non-touching ring ARHCF is shown above the CCD and an example transmitted light spectrum with multimode interference is shown next to the OSA.

The  $S^2$  measurement setup is illustrated in Fig. 61. A supercontinuum source (NKT Photonics SuperK Compact) is used as the broad band light source, SMF is used as the excitation fiber, a microscope objective (MO) and lens (L) are used in a 4-f configuration to image the near field of the ARHCFs on a CCD as well as on the facet of the  $S^2$  collection fiber (CF, a 50  $\mu\text{m}$  GIF), using a 50/50 beam splitter (BS). This enables a visual check on the input alignment conditions, e.g., the verification that most of the light is launched into the fundamental mode. An example fiber mode from an ARHCF is shown above the setup in Fig. 61. The  $S^2$  measurement is then performed as the collection fiber scans across the image of the ARHCFs facet on a 2D translation stage while the OSA measures the spectral interference at each location. All  $S^2$  measurements shown for this fiber were measured for 1400 nm - 1600 nm, as this range is spectrally flat and far from the fiber's resonances. The spectral interference pattern shown in Fig. 61 clearly shows a periodic modulation, indicating there are at least two modes present in the core of the fiber.



The HOMs present after propagation through various lengths of the non-touching ring HCF and their dependence on bending were investigated using this method. Figure 62 shows the combined Fourier spectrum from all of the measurements taken after propagating through 3.35 m of this fiber straight and bent to a diameter of 55 cm. The straight fiber clearly shows three peaks in the Fourier spectrum. These peaks correspond to the group delay difference (GDD) between the fundamental mode and the respective HOM with intensity distributions shown above them. Asymmetry in the drawn fiber is the assumed reason for the difference in effective index of the two  $LP_{02}$ -like modes. The power in each of these three modes is less than 1%, with about 0.7% in  $LP_{11}$  and 0.3% in each of the  $LP_{02}$  modes, calculated with the method described by Nicholson et al. [16]. Using the approximation that almost all of the light is in the fundamental mode, Otto et. al [117] simplified the calculation to simply:

$$I_{HOM} \approx \frac{T_{HOM}^2}{4} I_{FM} \quad ( 15 )$$

where  $I_{HOM}$  is the intensity in the HOM,  $T_{HOM}$  is the height of the peak in the Fourier transform, and  $I_{FM}$  is the intensity of the fundamental mode.

As the ARHCF is bent, the first two higher order mode peaks drop into the noise, and the third shifts in GDD. This shows that the bending caused the power in the first two HOMs to be coupled out of the core, while the effective refractive index difference between the fundamental mode and the second  $LP_{02}$  mode decreased.

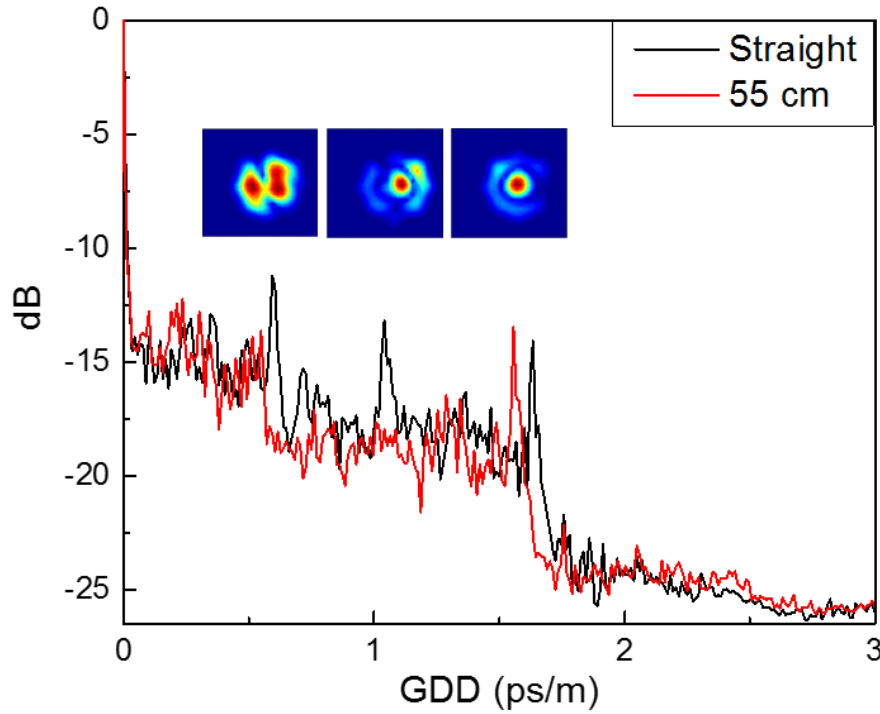


Figure 62. Fourier spectra of straight and bent non-touching ring HCF, with mode images above the corresponding peaks.

A dependence of the HOM content on the fiber length of the non-touching ring fiber was then investigated by analyzing the  $S^2$  measurements. Figure 63 shows the Fourier spectra of two of these measurements, taken as the length of the fiber was cut from 3.2 m down to 2 m. The same three HOM peaks are clearly visible, but a notable change in the peak height of the  $LP_{02}$  modes can be seen as the HCF was cut to 2 m. The height of the  $LP_{11}$  peak did not change significantly, indicating that the propagation loss of this mode is similar to the propagation loss of the fundamental mode. The loss measured from a cut back of this fiber was 0.68 dB/m in the region from 1400-1600 nm, and is shown as the black squares in the inset of Fig. 63. The loss of the combined  $LP_{02}$  modes was found to be approximately 4.2 dB/m from the  $S^2$  measurement, corresponding to the red circles in the inset.

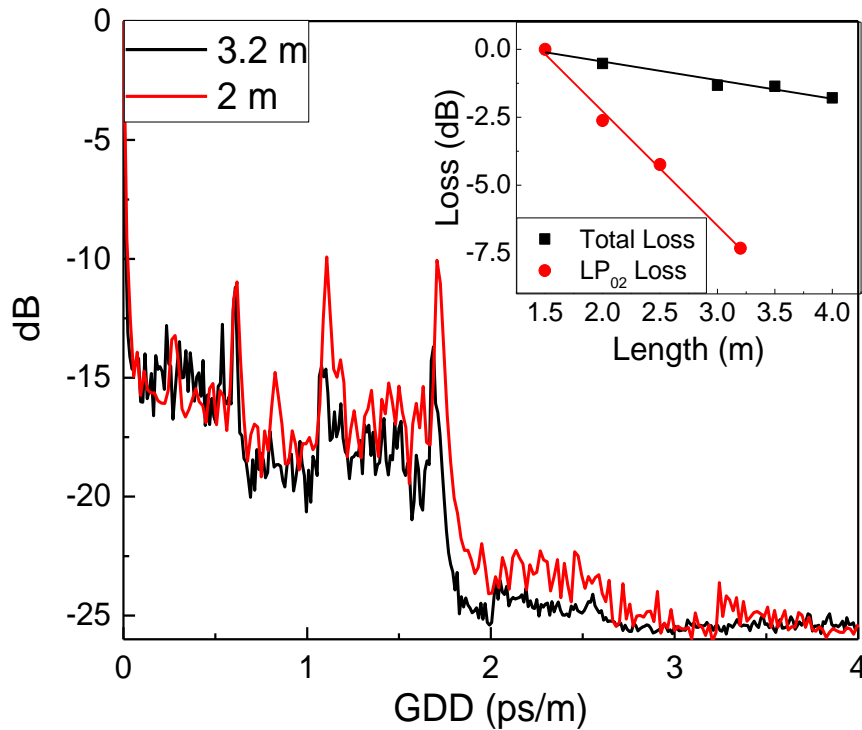


Figure 63. Fourier spectra of two lengths of non-touching ring HCF. (inset) Loss cut back measurements.

When the length of this fiber was cut to 0.5 m, the power in the HOMs increased significantly, and several more modes appeared at higher GDDs. At this short length of ARHCF, only approximately 50% of the light was guided in the fundamental mode, while the rest was divided among 5 higher order modes.

In addition to calculating the fundamental mode loss as a function of wavelength, Fig. 60 (b), the loss of the first HOMs was also calculated using COMSOL at the wavelength of 1550 nm. The loss of  $LP_{11}$  was found to be 0.6 dB/m, which is similar to the experimentally measured total loss of this fiber, 0.68 dB/m integrating from 1400 nm to 1600 nm. This agrees with the  $S^2$  measurement, where no significant change in the amplitude of the  $LP_{11}$  peak was observed as the fiber was cut from 3.2 m to 1.5 m. The loss of the  $LP_{02}$  mode at 1550 nm was calculated to be 3.7 dB/m. Again, this is comparable to the measured loss obtained from the  $S^2$  measurement, approximately 4.2 dB/m. Our simulation shows that the loss values calculated from  $S^2$  agree with the theoretical predications. The only major difference was the loss of the fundamental mode, which simulation calculated to be just 0.13 dB/m at 1550 nm. The measured loss is higher than this theoretical value due to imperfections in the drawn fiber which increase the overall attenuation.

The measurements on this fiber show that HOMs are in fact supported and can propagate in the core of the ARHCF. While at a length of 3.35 m more than 98% of the power is in the fundamental mode, this low HOM content can still have a significant impact depending on the application of the ARHCF. This HOM content can be further mitigated by either bending the fiber, or by using longer lengths.

Next, an ARHCF with touching capillaries that form a closed boundary core was investigated. An SEM image of the fiber is shown in the inset of Fig. 64. The core is 48  $\mu\text{m}$  in diameter (measured between the inner edges of two opposing capillaries), the capillaries are 30  $\mu\text{m}$  along the long axis, the thickness of the capillaries is 770 nm, and the outer diameter of the fiber is 150  $\mu\text{m}$ . The transmission spectra for 4 m of this fiber is shown in Fig. 64. Due to the locations of the resonances of this fiber, it was investigated in the region from 1100 nm – 1300 nm by  $S^2$  imaging. The average propagation loss measured in this wavelength range was 1.1 dB/m. A 4 m long piece of the ARHCF was measured straight and bent at various bending diameters.

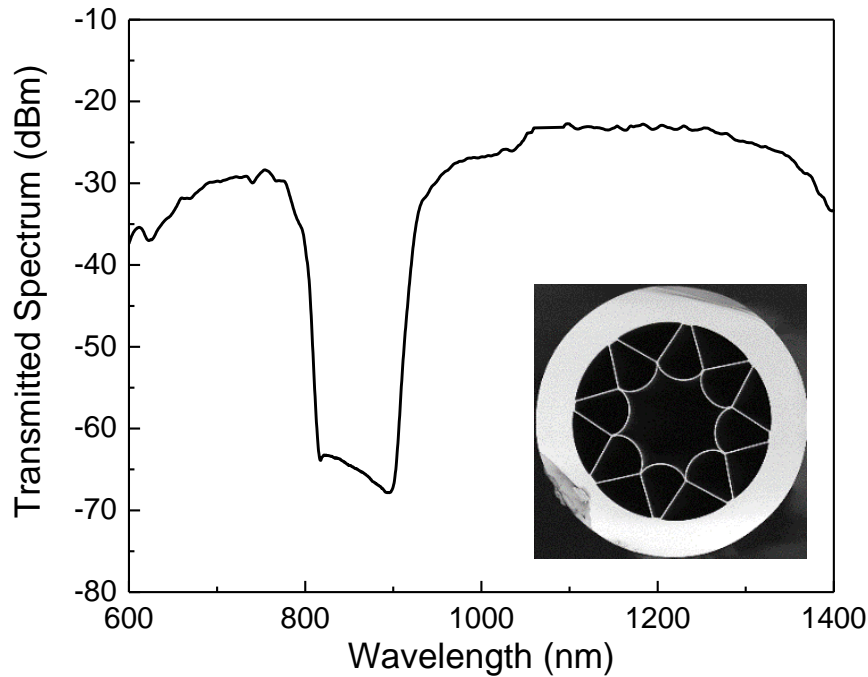


Figure 64. Transmitted white light spectrum of 4m of the touching ring HCF. (inset) SEM image of fiber facet.

Figure 65 shows the corresponding Fourier spectra of the straight fiber and bent to a diameter of 75 cm. Only one peak was visible, and the reconstructed  $LP_{11}$ -like mode image is shown above it. As the fiber is bent, the GDD of the  $LP_{11}$  mode shifts to smaller values, similarly to the non-touching ring ARHCF discussed above. In addition to shifting in GDD, the intensity of the peak decreases with decreasing bending diameter, showing the coupling of the  $LP_{11}$  mode to cladding modes of the fiber. The dependence of the power in  $LP_{11}$  is shown in the inset of Fig. 65 as a function of the bending diameter. With 4 m straight, the power in the  $LP_{11}$  mode was very low, approximately 0.01%. As the fiber is bent to a diameter of 35 cm, this power decreases to 0.001%.

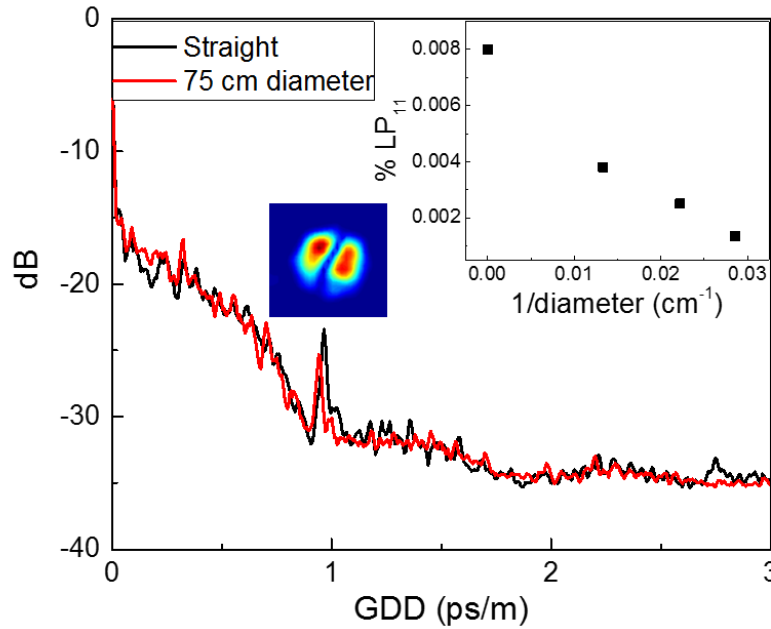


Figure 65. Fourier spectra of straight and bent touching ring HCF, with mode image above the corresponding peak. (inset) Power in  $LP_{11}$  as a function of bending diameter.

The length dependence of the HOM content was also determined with a cut back  $S^2$  measurement. As expected, Fig. 66 shows an increase in the peak intensity of the  $LP_{11}$  mode as the fiber is cut to a shorter length. Shown in the inset of Fig. 66 is a comparison of the total loss measured in a cut back measurement (black squares), and the loss of power in  $LP_{11}$  obtained from the  $S^2$  measurement (red circles). The estimated loss of the  $LP_{11}$  mode (red line in the inset) is 3.7 dB/m, which is much higher than the total propagation loss of 1.1 dB/m. At a length of only 1 m, the power in  $LP_{11}$  was still relatively low, at a value of about 0.9%.

We have to the best of our knowledge experimentally measured the mode content of ARHCFs using spatially and spectrally resolved imaging for the first time. Both fibers analyzed showed some HOM content, with the majority of the light being guided in the fundamental mode.

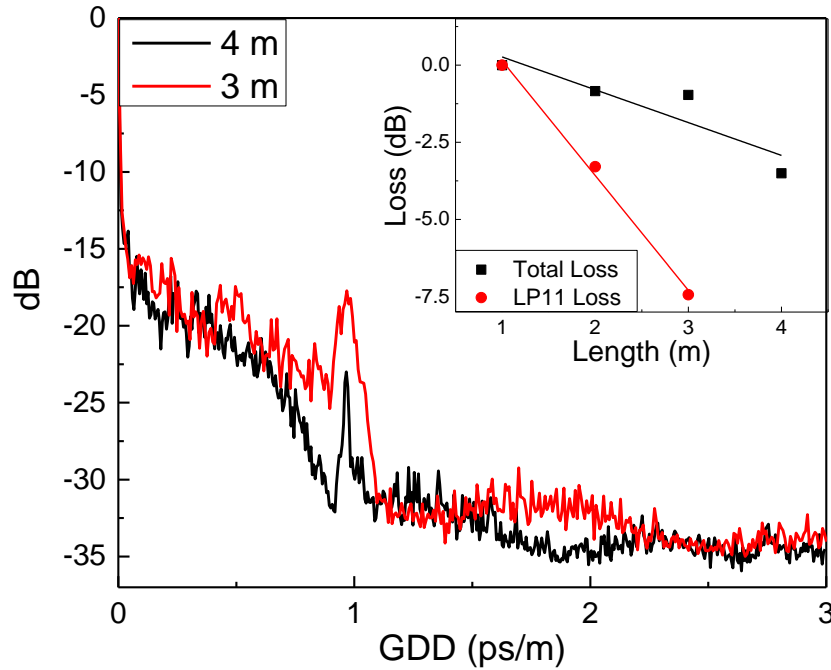


Figure 66. Fourier spectra of two lengths of touching ring HCF. (inset) Loss cut back measurements.

The HOM content found in the core of the closed boundary design fiber was significantly lower than that measured in the non-touching ring fiber. At a straight length of 3 m, the non-touching ring fiber contained about 1.3% HOM content, while the touching design only contained 0.1% of  $LP_{11}$ . Both fibers showed that, in general, the HOMs had higher bending loss and propagation loss than the fundamental mode, enabling possible mitigation of these modes through bending or using longer lengths of ARHCF. While the fundamental mode losses of the fibers shown here ( $\sim 1$  dB/m) and the HOM losses ( $\sim 4$  dB/m) allow for sufficiently single mode operation after a few meters of ARHCF, much lower fundamental mode losses and higher HOM extinction ratios have been shown to be possible. Recently, the experimentally measured propagation losses of ARHCF with similar designs reached values lower than 0.1 dB/m in the same wavelength regimes [93]. Also, simulations have shown HOM extinction ratios over 50 for a touching ring HCF [118] and 500 for a nested anti-resonant nodeless HCF [94].



As fabrication of the ARHCFs improved at CREOL, mode analysis measurements continue on the various designs. An improvement has been made to the  $S^2$  analysis code in MatLab in order to smooth Fourier spectra. This was done through zeropadding, or simply adding a number of zeros to the end of the measured transmission spectra before taking the Fourier transform.

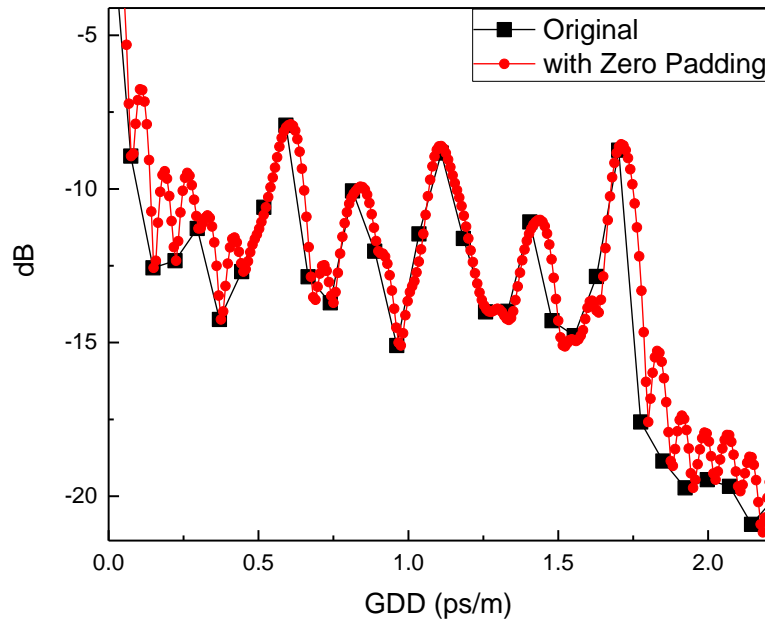


Figure 67. Comparison of Fourier spectra before and after zeropadding was implemented.

In doing this, the number of data points in the Fourier spectra increased, and the peaks corresponding to the HOMs were smoothed. This increases the accuracy when measuring the mode power. An example of the improvement from adding zeropadding is shown in Fig. 67.

## Summary and Outlook

Hollow core fibers based on the anti-resonant effect have been introduced, and their guiding mechanism and benefits over previous hollow core designs have been analyzed. A specific sensing application has been discussed, and a design for that application has been optimized in COMSOL, showing a customized transmission window for a Raman gas sensor.

Additionally, many fabricated ARHCF designs have been characterized for their propagation loss. An analysis on the dependence of the fiber design on the measured loss has agreed with the predicted improvements from variations in the cladding structure. To date, the lowest propagation loss measured has been with a seven ring, open boundary core design, and a value of  $\sim 0.2$  dB/m has been obtained around the wavelength of 800 nm. With the same design and a higher quality glass, the loss appeared to drop lower than 0.1 dB/m from 700-1100nm from an initial measurement.

Finally, two ARHCFs have been analyzed in detail using spatially and spectrally resolved imaging, in order to understand their HOM content, and how that changes as a function of fiber length and bending radius. This is the first detailed experimental analysis of HOM content in ARHCF. Both fibers were shown to have some small percentage of HOM content at lengths of a few meters, but these HOM could be decreased by simply using longer lengths or bending the ARHCF.

The work shown here has helped in understanding the dependence of the ARHCF design parameters on both the propagation loss and mode content of the fibers. All measurements agree well with simulations, and will allow for further improvements in future designs for various

applications. One specific application that we are working towards, the Raman air sensor for astronaut suits, shows great potential as only a small change in the current ARHCF designs will greatly improve both the coupling efficiency and the transmission bandwidth from the currently used system at Mesa Photonics.

## CHAPTER 4: CONCLUSION

In this dissertation, several different designs of specialty optical fiber were explored for uses in sensing applications. A complete investigation of coupled multicore fiber for various sensing applications has been presented. The benefits of this sensor configuration, such as high overall transmission, high sensitivity, sharp spectral features, and simple fabrication were explored and compared to traditional fiber sensors. The optimization of the MCF design was completed in simulation and verified by experiment, resulting in a publication in Optics Letters [58]. Spectral features were measured to be as deep as 35 dB, device loss was measured to be only 0.05 dB per splice, and 126 sensors were successfully fabricated and characterized by two students in two days. This sensor design has been patented by UCF and is in the process of being commercialized by a startup company, Multicore Photonics.

Sensitivity measurements were performed on the MCF sensors for temperature, strain, and bending. The MCF sensors were shown to be able to withstand temperatures up to 1000°C, making them suitable to be harsh environment sensors. Additionally, a simple method for increasing the sensitivity of the MCF to longitudinal force was shown to multiple the sensitivity of the MCF sensor by a factor of seven. Also, a configuration for decoupling force and temperature was presented and has been published in Photonics Technology Letters [65]. Finally, a developing all-fiber device, a photonic lantern, was used in conjunction with the MCF in order to increase sensitivity, add directional sensitivity, and lower the cost of the sensor interrogation for bending measurements. This combined device was published in Optics Letters [77].

A new design for the MCF was proposed, adding large air holes into the fiber in order to increase sensitivity to pressure and acoustic waves. Initial bands of fiber have been drawn, and the first SMS devices were spliced. Sensitivity to temperature, strain, bending, and acoustic waves has been measured. Initial results show drastic increases in sensitivity to bending and acoustic waves, compared to the solid MCF. The spectra of the SMS devices show that the design of the air hole MCF needs to be further optimized in order to obtain cleaner, more easily tracked MMI, but the increase in sensitivity measured to date shows great potential for many applications.

Additionally, ARHCF in various designs have been explored. In simulation, an ARHCF for a Raman air sensor was optimized for a specific wavelength range. Also, the dependence of the design of the cladding structure on the propagation loss was analyzed through a series of cutback measurements on fiber fabricated at CREOL. These measurements showed an improvement in the loss for an open boundary design, seven cladding rings, and higher quality material. Finally, the mode content of ARHCF was investigated using  $S^2$  imaging. A comparison between measurement and simulation showed good agreement, and understanding of possible ways to mitigate HOM content was developed. These measurements will help to improve future designs of ARHCF for applications such as high power delivery, UV and Mid IR transmission, gas sensing, and in-fiber lasers.

The work presented here shows significant progress in the field of sensing using specialty optical fibers. Sensors based on coupled MCF have shown great promise, and now can be further developed, i.e. harsh environment packaging, in order to enter commercial viability. The air hole

MCF sensors have shown great promise in their extreme sensitivity, but need further fiber design and splicing development in order to become reliable sensors. The work shown on ARHCF has pushed forward the development in CREOL's ability to fabricate these complex and highly desirable fibers. The capability to design and fabricate these fibers has opened up many possibilities for future applications, including unique in-fiber sensors.

## **APPENDIX: PUBLICATIONS**

### Journal Publications

1. **Amy Van Newkirk**, J. E. Antonio-Lopez, James Anderson, Roberto Alvarez-Aguirre, Zeinab Sanjabi Eznavah, Gisela Lopez-Galmiche, Rodrigo Amezcua-Correa, Axel Schülzgen, "Modal Analysis of Anti-Resonant Hollow Core Fibers using S<sup>2</sup> Imaging", Opt. Lett. (submitted May 2016).
2. Joel Villatoro, **Amy Van Newkirk**, Jose Antonio-Lopez, Joseba Zubia, Axel Schülzgen, and Rodrigo Amezcua Correa, "Ultrasensitive vector bending sensor based on multicore optical fiber," Opt. Lett. 41, 832-835 (2016).
3. **A. Van Newkirk**, J. E. Antonio-Lopez, A. Velazquez-Benitez, J. Albert, R. Amezcua-Correa, and A. Schülzgen, "Bending sensor combining multicore fiber with a mode-selective photonic lantern," Opt. Lett. 40, 5188–5191 (2015).
4. **A. Van Newkirk**, J. E. Antonio-Lopez, G. Salceda-Delgado, M. U. Piracha, R. Amezcua-Correa, and A. Schülzgen, "Multicore Fiber Sensors for Simultaneous Measurement of Force and Temperature," IEEE Photonics Technol. Lett. 27, 1523–1526 (2015).
5. G. Salceda-Delgado, **A. Van Newkirk**, J. E. Antonio-Lopez, A. Martinez-Rios, A. Schülzgen, and R. Amezcua Correa, "Compact fiber-optic curvature sensor based on super-mode interference in a seven-core fiber," Opt. Lett. 40, 1468–1471 (2015).
6. **A. Van Newkirk**, E. Antonio-Lopez, G. Salceda-Delgado, R. Amezcua-Correa, and A. Schülzgen, "Optimization of multicore fiber for high-temperature sensing," Opt. Lett. 39, 4812 (2014).
7. G. Freihofer, D. Fugon-Dessources, E. Ergin, **A. Van Newkirk**, A. Gupta, S. Seal, A. Schülzgen, and S. Raghavan, "Piezospectroscopic measurements capturing the evolution of plasma-spray coating stresses with substrate loads.," ACS Appl. Mater. Interfaces (2014).

### Conference Presentations

1. **Amy Van Newkirk**, J. E. Antonio-Lopez, James Anderson, Roberto Alvarez-Aguirre, Rodrigo Amezcua-Correa, Axel Schülzgen, "Higher Order Modes in Anti-Resonant Hollow Core Fibers", in Advanced Photonics (OSA, 2016), p. SoM3F.4.
2. **Amy Van Newkirk**, J. E. Antonio-Lopez, James Anderson, Roberto Alvarez-Aguirre, Zeinab Sanjabi Eznavah, Rodrigo Amezcua-Correa, Axel Schülzgen, "Modal Analysis of Anti-



Resonant Hollow Core Fibers”, in CLEO: 2016 (OSA 2016), p. Stu4P.7.

3. Joel Villatoro, Enrique Antonio-Lopez, **Amy Van Newkirk**, Joseba Zubia, Axel Schülzgen, Rodrigo Amezcua-Correa, “Supersensitive Sensors based on Multicore Optical Fibres”, Proc. SPIE 9886, Micro-structured and Specialty Optical Fibres, 9886-8 (2016).
4. **A. Van Newkirk**, A. M. Velázquez-Benítez, J. E. Antonio-Lopez, J. Albert, R. Amezcua Correa, and A. Schülzgen, "3D Bending Sensor Combining Multicore Fiber with a Mode-Selective Photonic Lantern," in Workshop on Specialty Optical Fibers and Their Applications (OSA, 2015), p. WT4A.6.
5. A. Schülzgen, **A. Van Newkirk**, J. Anderson, G. Salceda-Delgado, Z. S. Eznaveh, J. E. Antonio-Lopez, C. Xia, G. Li, R. G. van Uden, F. M. Huijskens, H. de Waardt, T. A. Koonen, C. Okonkwo, and R. Amezcua Correa, "Multicore Fibers," in Workshop on Specialty Optical Fibers and Their Applications (OSA, 2015), p. WF3A.1.
6. A. Schülzgen, J. Anderson, C. Jollivet, **A. Van Newkirk**, K. Schuster, and S. Grimm, "Multi-Core Fiber Lasers," in Frontiers in Optics 2015 (OSA, 2015), p. LTu2H.2.
7. **A. Van Newkirk**, E. Antonio-Lopez, G. Salceda-Delgado, M. U. Piracha, R. Amezcua-Correa, and A. Schülzgen, "Simultaneous Measurement of Strain and Temperature using High Sensitivity Multicore Fiber Sensors," in CLEO: 2015 (OSA, 2015), p. SM1L.4.
8. B. Pati, wenyen Tian, **A. Van Newkirk**, and A. Schülzgen, "High Power WDM with Narrow Wavelength Separations," in CLEO: 2015 (OSA, 2015), p. STu1N.3.
9. **A. Van Newkirk**, J. E. Antonio-Lopez, G. Salceda-Delgado, M. U. Piracha, R. Amezcua-Correa, and A. Schülzgen, “Multicore Fiber Strain Sensor with Increased Sensitivity,” Proc. SPIE 9480, Fiber Optic Sensors and Applications XII, 9480-20 (2015).
10. C. Jollivet, **A. Van Newkirk**, J. Anderson, K. Schuster, S. Grimm, and A. Schülzgen, "Advances in Multi-Core Fiber Lasers," in Latin America Optics and Photonics Conference (OSA, 2014), p. LM1D.3.
11. **A. Van Newkirk**, G. Salceda-Delgado, J. E. Antonio-Lopez, R. Amezcua-Correa, and A. Schülzgen, "Multicore Optical Fiber Point Sensors - OSA Technical Digest (online)," in Frontiers in Optics 2014 (Optical Society of America, 2014), p. FTu4B.3.
12. **A. Van Newkirk**, E. Antonio-Lopez, G. Salceda-Delgado, R. Amezcua-Correa, and A. Schülzgen, "Supermode Interference in Multicore Fiber Optimized for use in Sensing Applications - OSA Technical Digest (online)," in Advanced Photonics (Optical Society of America, 2014), p. SoW2B.4.

13. G. Salceda, **A. Van Newkirk**, J. E. Antonio-Lopez, A. Schülzgen, and R. Amezcua-Correa, "Optical Fiber curvature sensors based on single mode - 7 core - single mode fiber structures - OSA Technical Digest (online)," in Advanced Photonics (Optical Society of America, 2014), p. SeW3C.2.
14. J. E. Antonio-Lopez, G. Salceda-Delgado, **A. Van Newkirk**, A. Schülzgen, and R. Amezcua-Correa, "Multiplexed High Temperature Sensor Based on Multicore Fiber - OSA Technical Digest (online)," in Advanced Photonics (Optical Society of America, 2014), p. SeW4C.2.
15. **A. Van Newkirk**, Z. Sanjabi Eznavah, E. Antonio-Lopez, G. Salceda-Delgado, A. Schülzgen, and R. Amezcua-Correa, "High Temperature Sensor based on Supermode Interference in Multicore Fiber," in CLEO: 2014 (OSA, 2014), p. SM2N.7.
16. P. Hofmann, K. Al Yahyaei, C. Jollivet, **A. Van Newkirk**, R. Amezcua-Correa, E. Antonio-Lopez, D. Ott, M. SeGall, I. Divliansky, L. Glebova, L. Glebov, and A. Schülzgen, "Highly Photosensitive Fiber Fabricated from Photo-Thermo-Refractive Glass," 38th International Conference and Exposition on Advanced Ceramics and Composites (Invited), paper #: ICACC-FS2-025-2014, Daytona Beach, (USA) 2014.
17. G. Freihofer, A. Jones, D. Fugon, **A. Van Newkirk**, A. Schülzgen, A. Gupta, S. Seal, H. Tat, and S. Raghavan, "Optical Stress Sensing Alumina Nanocomposite Coatings for Aerospace Structures," Scitech 2014, paper ID: 1735156, Washington DC (USA) 2014.
18. **A. Van Newkirk**, P. Hofmann, C. Voigtländer, S. Nolte, N. Peyghambarian, and A. Schülzgen, "Monolithic Phosphate Glass Fiber Lasers with Gratings Inscribed by fs-Laser Pulses," in Frontiers in Optics 2013, D. Delyett, Jr., P. and Gauthier, ed. (OSA, 2013), p. LTh4F.4.
19. W. Gysi, K. Lautenslager, G. Freihofer, A. S. Jones, C. Jollivet, **A. Van Newkirk**, A. Schülzgen, and S. Raghavan, "GOALI: Developing Piezospectroscopic Sensing Systems in Adhesives and Coatings," NSF CMMI Engineering Research and Innovation Conference 2012, paper: E144, Boston (USA) 2012.

## REFERENCES

1. K. C. Kao and G. A. Hockham, "Dielectric-fibre surface waveguides for optical frequencies," *Proc. Inst. Electr. Eng.* **113**, 1151 (1966).
2. F. P. Kapron, "RADIATION LOSSES IN GLASS OPTICAL WAVEGUIDES," *Appl. Phys. Lett.* **17**, 423 (1970).
3. S. Personick, "Fiber optic communication - A technology coming of age," *IEEE Commun. Soc. Mag.* **16**, 12–20 (1978).
4. D. Gloge and E. A. J. Marcatili, "Multimode Theory of Graded-Core Fibers," *Bell Syst. Tech. J.* **52**, 1563–1578 (1973).
5. J. C. Knight, T. A. Birks, P. S. J. Russell, and D. M. Atkin, "All-silica single-mode optical fiber with photonic crystal cladding," *Opt. Lett.* **21**, 1547 (1996).
6. F. Jansen, F. Stutzki, H.-J. Otto, M. Baumgartl, C. Jauregui, J. Limpert, and A. Tünnermann, "The influence of index-depressions in core-pumped Yb-doped large pitch fibers.," *Opt. Express* **18**, 26834–42 (2010).
7. W. Belardi and J. C. Knight, "Effect of core boundary curvature on the confinement losses of hollow antiresonant fibers.," *Opt. Express* **21**, 21912–7 (2013).
8. J. B. MacChesney, P. B. O'Connor, and H. M. Presby, "A new technique for the preparation of low-loss and graded-index optical fibers," *Proc. IEEE* **62**, 1280–1281 (1974).
9. E. Snitzer, "Proposed Fiber Cavities for Optical Masers," *J. Appl. Phys.* **32**, 36 (1961).
10. C. J. Koester and E. Snitzer, "Amplification in a Fiber Laser," *Appl. Opt.* **3**, 1182 (1964).
11. K. O. Hill, Y. Fujii, D. C. Johnson, and B. S. Kawasaki, "Photosensitivity in optical fiber waveguides: Application to reflection filter fabrication," *Appl. Phys. Lett.* **32**, 647 (1978).
12. E. H. Turner and R. H. Stolen, "Fiber Faraday circulator or isolator," *Opt. Lett.* **6**, 322 (1981).
13. M. Eisenmann and E. Weidel, "Single-mode fused biconical couplers for wavelength division multiplexing with channel spacing between 100 and 300 nm," *J. Light. Technol.* **6**, 113–119 (1988).
14. T. Theeg, H. Sayinc, J. Neumann, L. Overmeyer, and D. Kracht, "Pump and signal

- combiner for bi-directional pumping of all-fiber lasers and amplifiers.," *Opt. Express* **20**, 28125–41 (2012).
15. T. E. Dimmick, G. Kakarantzas, T. A. Birks, and P. S. J. Russell, "Carbon dioxide laser fabrication of fused-fiber couplers and tapers," *Appl. Opt.* **38**, 6845 (1999).
  16. T. A. Birks, I. Gris-Sánchez, S. Yerolatsitis, S. G. Leon-Saval, and R. R. Thomson, "The photonic lantern," *Adv. Opt. Photonics* **7**, 107 (2015).
  17. H. Ishiwatari, M. Ikedo, and F. Tateishi, "An optical cable for a CO<sub>2</sub> laser scalpel," *J. Light. Technol.* **4**, 1273–1279 (1986).
  18. A. Constable, J. Kim, J. Mervis, F. Zarinetchi, and M. Prentiss, "Demonstration of a fiber-optical light-force trap," *Opt. Lett.* **18**, 1867 (1993).
  19. A. D. Kersey, "A Review of Recent Developments in Fiber Optic Sensor Technology," *Opt. Fiber Technol.* **2**, 291–317 (1996).
  20. A. D. Kersey, M. A. Davis, H. J. Patrick, M. LeBlanc, K. P. Koo, C. G. Askins, M. A. Putnam, and E. J. Friebele, "Fiber grating sensors," *J. Light. Technol.* **15**, 1442–1463 (1997).
  21. A. Hongo, S. Kojima, and S. Komatsuzaki, "Applications of fiber Bragg grating sensors and high-speed interrogation techniques," *Struct. Control Heal. Monit.* **12**, 269–282 (2005).
  22. S. J. Mihailov, "Fiber Bragg Grating Sensors for Harsh Environments," *Sensors* **12**, 1898–1918 (2012).
  23. K. O. Hill and G. Meltz, "Fiber Bragg grating technology fundamentals and overview," *J. Light. Technol.* **15**, 1263–1276 (1997).
  24. W. Jin, "Multiplexed FBG sensors and their applications," in *Advanced Photonic Sensors and Applications*, R. A. Lieberman, A. K. Asundi, and H. Asanuma, eds. (International Society for Optics and Photonics, 1999), pp. 468–479.
  25. C. R. Liao and D. N. Wang, "Review of femtosecond laser fabricated fiber Bragg gratings for high temperature sensing," *Photonic Sensors* **3**, 97–101 (2013).
  26. J. Canning, M. Stevenson, S. Bandyopadhyay, and K. Cook, "Extreme Silica Optical Fibre Gratings," *Sensors* **8**, 6448–6452 (2008).
  27. T. Elsmann, T. Habisreuther, M. W. Rothhardt, and H. Bartelt, "High Temperature Sensing with Fiber Bragg Gratings in Sapphire Fibers," in *Advanced Photonics* (Optical

Society of America, 2014), p. BTu5B.2.

28. A. J. Rogers, "Polarization-optical time domain reflectometry: a technique for the measurement of field distributions.," *Appl. Opt.* **20**, 1060–74 (1981).
29. J. N. Ross, "Birefringence measurement in optical fibers by polarization-optical time-domain reflectometry.," *Appl. Opt.* **21**, 3489–95 (1982).
30. A. Hartog, "A distributed temperature sensor based on liquid-core optical fibers," *J. Light. Technol.* **1**, 498–509 (1983).
31. H. Kogelnik and T. Li, "Laser Beams and Resonators," *Appl. Opt.* **5**, 1550–1567 (1966).
32. T. Horiguchi, T. Kurashima, and Y. Koyamada, "Measurement of temperature and strain distribution by Brillouin frequency shift in silica optical fibers," in *SPIE 1797, Distributed and Multiplexed Fiber Optic Sensors II*, 2, J. P. Dakin and A. D. Kersey, eds. (International Society for Optics and Photonics, 1993), pp. 2–13.
33. T. Kurashima, T. Horiguchi, and M. Tateda, "Distributed-temperature sensing using stimulated Brillouin scattering in optical silica fibers," *Opt. Lett.* **15**, 1038 (1990).
34. X. Bao and L. Chen, "Recent progress in distributed fiber optic sensors.," *Sensors (Basel)*. **12**, 8601–39 (2012).
35. Q. Sun, H. Luo, H. Luo, M. Lai, D. Liu, and L. Zhang, "Multimode microfiber interferometer for dual-parameters sensing assisted by Fresnel reflection," *Opt. Express* **23**, 12777 (2015).
36. B. Sun, Y. Huang, S. Liu, C. Wang, J. He, C. Liao, G. Yin, J. Zhao, Y. Liu, J. Tang, J. Zhou, and Y. Wang, "Asymmetrical in-fiber Mach-Zehnder interferometer for curvature measurement.," *Opt. Express* **23**, 14596–602 (2015).
37. S. Rota-Rodrigo, M. López-Amo, J. Kobelke, K. Schuster, J. L. Santos, and O. Frazão, "Multimodal Interferometer Based on a Suspended Core Fiber for Simultaneous Measurement of Physical Parameters," *J. Light. Technol.* **33**, 2468–2473 (2015).
38. L. Xiaojuan, F. Shenggui, G. Liping, and H. Kezhen, "Narrow linewidth Yb-doped fiber laser at 1120nm," *Appl. Opt.* **52**, 1829–1831 (2013).
39. W. Lin, B. Song, Y. Miao, H. Zhang, D. Yan, B. Liu, and Y. Liu, "Liquid-filled photonic-crystal-fiber-based multimodal interferometer for simultaneous measurement of temperature and force," *Appl. Opt.* **54**, 1309 (2015).
40. Zhengyu Huang, Yizheng Zhu, Xiaopei Chen, and Anbo Wang, "Intrinsic Fabry-Pe/spl

- acute/rot fiber sensor for temperature and strain measurements," *IEEE Photonics Technol. Lett.* **17**, 2403–2405 (2005).
41. J. Mathew, O. Schneller, D. Polyzos, D. Havermann, R. M. Carter, W. N. MacPherson, D. P. Hand, and R. R. J. Maier, "In-Fiber Fabry–Perot Cavity Sensor for High-Temperature Applications," *J. Light. Technol.* **33**, 2419–2425 (2015).
  42. C. C. Cutler, S. A. Newton, and H. J. Shaw, "Limitation of rotation sensing by scattering," *Opt. Lett.* **5**, 488 (1980).
  43. P.-A. Nicati and P. Robert, "Stabilized Sagnac Optical Fiber Current Sensor Using One Phase And Two Amplitude Modulations," in *Optical Fiber Sensors* (OSA, 1992), p. F35.
  44. M. R. Layton and J. A. Bucaro, "Optical fiber acoustic sensor utilizing mode-mode interference.," *Appl. Opt.* **18**, 666–70 (1979).
  45. W. Eickhoff, "Temperature sensing by mode-mode interference in birefringent optical fibers," *Opt. Lett.* **6**, 204 (1981).
  46. A. Kumar, R. K. Varshney, S. Antony C, and P. Sharma, "Transmission characteristics of SMS fiber optic sensor structures," *Opt. Commun.* **219**, 215–219 (2003).
  47. A. Mehta, W. Mohammed, and E. G. Johnson, "Multimode interference-based fiber-optic displacement sensor," *IEEE Photonics Technol. Lett.* **15**, 1129–1131 (2003).
  48. E. Li, X. Wang, and C. Zhang, "Fiber-optic temperature sensor based on interference of selective higher-order modes," *Appl. Phys. Lett.* **89**, 091119 (2006).
  49. Jianzhong Zhang and Shijun Peng, "A Compact SMS Refractometer Based on HF Corrosion Scheme," in *2010 Symposium on Photonics and Optoelectronics* (IEEE, 2010), pp. 1–4.
  50. S. M. Tripathi, A. Kumar, R. K. Varshney, Y. B. P. Kumar, E. Marin, and J.-P. Meunier, "Strain and Temperature Sensing Characteristics of Single-Mode–Multimode–Single-Mode Structures," *J. Light. Technol.* **27**, 2348–2356 (2009).
  51. S. Silva, J. L. Santos, F. X. Malcata, J. Kobelke, K. Schuster, and O. Frazão, "Optical refractometer based on large-core air-clad photonic crystal fibers.," *Opt. Lett.* **36**, 852–4 (2011).
  52. A. Zhou, G. Li, Y. Zhang, Y. Wang, C. Guan, J. Yang, and L. Yuan, "Asymmetrical Twin-Core Fiber Based Michelson Interferometer for Refractive Index Sensing," *J. Light. Technol.* **29**, 2985–2991 (2011).

53. J. R. Guzman-Sepulveda and D. A. May-Arrioja, "In-fiber directional coupler for high-sensitivity curvature measurement.," *Opt. Express* **21**, 11853–61 (2013).
54. R. M. Silva, M. S. Ferreira, J. Kobelke, K. Schuster, and O. Frazão, "Simultaneous measurement of curvature and strain using a suspended multicore fiber," *Opt. Lett.* **36**, 3939–3941 (2011).
55. J. R. Guzman-Sepulveda, D. Lopez-Cortes, I. Hernandez-Romano, W. Margulis, and D. A. May-Arrioja, "Refractive Index Sensor using a Two-Core Optical Fiber," in (*Optical Society of America*, 2012), p. JW2A.114.
56. C. Xia, N. Bai, I. Ozdur, X. Zhou, and G. Li, "Supermodes for optical transmission.," *Opt. Express* **19**, 16653–64 (2011).
57. A. Yariv, "Coupled-mode theory for guided-wave optics," *IEEE J. Quantum Electron.* **9**, 919–933 (1973).
58. A. Van Newkirk, E. Antonio-Lopez, G. Salceda-Delgado, R. Amezcua-Correa, and A. Schülzgen, "Optimization of multicore fiber for high-temperature sensing," *Opt. Lett.* **39**, 4812 (2014).
59. C. Guan and L. Yuan, "Supermodes Analysis for Linearly Distributed Multicore Fiber," in *2009 Symposium on Photonics and Optoelectronics* (IEEE eXpress Conference Publishing, 2009), pp. 1–4.
60. C. Jollivet, A. Mafi, D. Flamm, M. Duparré, K. Schuster, S. Grimm, and A. Schülzgen, "Mode-resolved gain analysis and lasing in multi-supermode multi-core fiber laser," *Opt. Express* **22**, 30377 (2014).
61. F. C. Favero, R. Spittel, F. Just, J. Kobelke, M. Rothhardt, and H. Bartelt, "A miniature temperature high germanium doped PCF interferometer sensor," *Opt. Express* **21**, 30266 (2013).
62. J. Demas, M. D. W. Grogan, T. Alkeskjold, and S. Ramachandran, "Sensing with optical vortices in photonic-crystal fibers.," *Opt. Lett.* **37**, 3768–70 (2012).
63. J. E. Antonio-Lopez, Z. S. Eznavah, P. LiKamWa, A. Schülzgen, and R. Amezcua-Correa, "Multicore fiber sensor for high-temperature applications up to 1000°C.," *Opt. Lett.* **39**, 4309–12 (2014).
64. D. B. Leviton and B. J. Frey, "Temperature-dependent absolute refractive index measurements of synthetic fused silica," *11* (2008).
65. A. Van Newkirk, J. E. Antonio-Lopez, G. Salceda-Delgado, M. U. Piracha, R. Amezcua-

- Correa, and A. Schulzgen, "Multicore Fiber Sensors for Simultaneous Measurement of Force and Temperature," *IEEE Photonics Technol. Lett.* **27**, 1523–1526 (2015).
66. X. Zhong, Y. Wang, J. Qu, C. Liao, S. Liu, J. Tang, Q. Wang, J. Zhao, K. Yang, and Z. Li, "High-sensitivity strain sensor based on inflated long period fiber grating," *Opt. Lett.* **39**, 5463 (2014).
  67. S. K. Mondal, U. Tiwari, G. C. Poddar, V. Mishra, N. Singh, S. C. Jain, S. N. Sarkar, K. D. Chattopadhyaya, and P. Kapur, "Single fiber Bragg grating sensor with two sections of different diameters for longitudinal strain and temperature discrimination with enhanced strain sensitivity.," *Rev. Sci. Instrum.* **80**, 103106 (2009).
  68. B. Guan and H. Tam, "Simultaneous strain and temperature measurement using a superstructure fiber Bragg grating," ... *Technol. Lett. IEEE* **12**, 675–677 (2000).
  69. J. Jung, H. Nam, J. H. Lee, N. Park, and B. Lee, "Simultaneous Measurement of Strain and Temperature by use of a Single-Fiber Bragg Grating and an Erbium-Doped Fiber Amplifier," *Appl. Opt.* **38**, 2749 (1999).
  70. Y. Liu and L. Wei, "Low-cost high-sensitivity strain and temperature sensing using graded-index multimode fibers," *Appl. Opt.* **46**, 2516 (2007).
  71. G. Salceda-Delgado, A. Van Newkirk, J. E. Antonio-Lopez, A. Martinez-Rios, A. Schülzgen, and R. Amezcua Correa, "Compact fiber-optic curvature sensor based on super-mode interference in a seven-core fiber," *Opt. Lett.* **40**, 1468–1471 (2015).
  72. G. Salceda, A. Van Newkirk, J. E. Antonio-Lopez, A. Schulzgen, and R. Amezcua-Correa, "Optical Fiber curvature sensors based on single mode - 7 core - single mode fiber structures - OSA Technical Digest (online)," in *Advanced Photonics* (Optical Society of America, 2014), p. SeW3C.2.
  73. P. Saffari, T. Allsop, A. Adebayo, D. Webb, R. Haynes, and M. M. Roth, "Long period grating in multicore optical fiber: an ultra-sensitive vector bending sensor for low curvatures.," *Opt. Lett.* **39**, 3508–11 (2014).
  74. C. Waltermann, A. Doering, M. Köhring, M. Angelmahr, and W. Schade, "Cladding waveguide gratings in standard single-mode fiber for 3D shape sensing," *Opt. Lett.* **40**, 3109 (2015).
  75. D. Barrera, I. Gasulla, and S. Sales, "Multipoint Two-Dimensional Curvature Optical Fiber Sensor Based on a Nontwisted Homogeneous Four-Core Fiber," *J. Light. Technol.* **33**, 2445–2450 (2015).
  76. R. G. Duncan, M. E. Froggatt, S. T. Kreger, R. J. Seeley, D. K. Gifford, A. K. Sang, and



- M. S. Wolfe, "High-accuracy fiber-optic shape sensing," in *Sensor Systems and Networks: Phenomena, Technology, and Applications for NDE and Health Monitoring 2007* (2007), p. 65301S.
77. A. Van Newkirk, J. E. Antonio-Lopez, A. Velazquez-Benitez, J. Albert, R. Amezcua-Correa, and A. Schülzgen, "Bending sensor combining multicore fiber with a mode-selective photonic lantern," *Opt. Lett.* **40**, 5188–5191 (2015).
  78. S. G. Leon-Saval, T. A. Birks, J. Bland-Hawthorn, and M. Englund, "Multimode fiber devices with single-mode performance," *Opt. Lett.* **30**, 2545 (2005).
  79. A. M. Velazquez-Benitez, J. C. Alvarado, G. Lopez-Galmiche, J. E. Antonio-Lopez, J. Hernández-Cordero, J. Sanchez-Mondragon, P. Sillard, C. M. Okonkwo, and R. Amezcua-Correa, "Six mode selective fiber optic spatial multiplexer.," *Opt. Lett.* **40**, 1663–6 (2015).
  80. B. Ercan, R. Ryf, J. Bland-Hawthorn, J. R. S. Gil, S. G. Leon-Saval, and N. K. Fontaine, "Mode-selective dissimilar fiber photonic-lantern spatial multiplexers for few-mode fiber," in *39th European Conference and Exhibition on Optical Communication (ECOC 2013)* (Institution of Engineering and Technology, 2013), pp. 1221–1223.
  81. J. Villatoro, A. Van Newkirk, E. Antonio-Lopez, J. Zubia, A. Schülzgen, and R. Amezcua-Correa, "Ultrasensitive vector bending sensor based on multicore optical fiber.," *Opt. Lett.* **41**, 832–5 (2016).
  82. Chuang Wu, Bai-Ou Guan, Zhi Wang, and Xinhuan Feng, "Characterization of Pressure Response of Bragg Gratings in Grapefruit Microstructured Fibers," *J. Light. Technol.* **28**, 1392–1397 (2010).
  83. D. Chen, G. Hu, M. L. V. Tse, and H. Y. Tam, "Design of a dual-core dual-hole fiber for hydrostatic pressure sensing," *Opt. Commun.* **285**, 2615–2619 (2012).
  84. M. Hou, Y. Wang, S. Liu, J. Guo, Z. Li, and P. Lu, "Sensitivity-Enhanced Pressure Sensor With Hollow-Core Photonic Crystal Fiber," *J. Light. Technol.* **32**, 4035–4039 (2014).
  85. R. Amezcua-Correa, A. Schülzgen, and J. E. Antonio-Lopez, "Multicore optical fiber apparatus, methods, and applications," U.S. patent WO2015163963A2 (December 17, 2015).
  86. W. Belardi and J. C. Knight, "Hollow antiresonant fibers with reduced attenuation.," *Opt. Lett.* **39**, 1853–6 (2014).
  87. W. Belardi and J. C. Knight, "Hollow antiresonant fibers with low bending loss.," *Opt.*

- Express **22**, 10091–6 (2014).
88. W. Belardi, "Design and Properties of Hollow Antiresonant Fibers for the Visible and Near Infrared Spectral Range," J. Light. Technol. **33**, 4497–4503 (2015).
  89. F. Yu and J. Knight, "Negative Curvature Hollow Core Optical Fiber," IEEE J. Sel. Top. Quantum Electron. **22**, 1–1 (2015).
  90. A. Hartung, J. Kobelke, A. Schwuchow, J. Bierlich, J. Popp, M. A. Schmidt, and T. Frosch, "Low-loss single-mode guidance in large-core antiresonant hollow-core fibers," Opt. Lett. **40**, 3432 (2015).
  91. E. N. Fokoua, S. R. Sandoghchi, Y. Chen, G. T. Jasion, N. V. Wheeler, N. K. Baddela, J. R. Hayes, M. N. Petrovich, D. J. Richardson, and F. Poletti, "Accurate modelling of fabricated hollow-core photonic bandgap fibers," Opt. Express **23**, 23117 (2015).
  92. J. C. Knight, "Photonic Band Gap Guidance in Optical Fibers," Science (80-. ). **282**, 1476–1478 (1998).
  93. F. Yu and J. C. Knight, "Spectral attenuation limits of silica hollow core negative curvature fiber.," Opt. Express **21**, 21466–71 (2013).
  94. F. Poletti, "Nested antiresonant nodeless hollow core fiber," Opt. Express **22**, 23807 (2014).
  95. A. N. Kolyadin, A. F. Kosolapov, A. D. Pryamikov, A. S. Biriukov, V. G. Plotnichenko, and E. M. Dianov, "Light transmission in negative curvature hollow core fiber in extremely high material loss region.," Opt. Express **21**, 9514–9 (2013).
  96. A. Hartung, J. Kobelke, A. Schwuchow, K. Wondraczek, J. Bierlich, J. Popp, T. Frosch, and M. A. Schmidt, "Double antiresonant hollow core fiber--guidance in the deep ultraviolet by modified tunneling leaky modes.," Opt. Express **22**, 19131–40 (2014).
  97. P. Uebel, M. C. Günendi, M. H. Frosz, G. Ahmed, N. N. Edavalath, J.-M. Ménard, and P. S. J. Russell, "Broadband robustly single-mode hollow-core PCF by resonant filtering of higher-order modes," Opt. Lett. **41**, 1961 (2016).
  98. M. Michieletto, J. K. Lyngsø, C. Jakobsen, J. Lægsgaard, O. Bang, and T. T. Alkeskjold, "Hollow-core fibers for high power pulse delivery," Opt. Express **24**, 7103 (2016).
  99. G. Tsiminis, K. J. Rowland, E. P. Schartner, N. A. Spooner, T. M. Monro, and H. Ebendorff-Heidepriem, "Single-ring hollow core optical fibers made by glass billet extrusion for Raman sensing," Opt. Express **24**, 5911 (2016).

100. P. S. J. Russell, P. Hölzer, W. Chang, A. Abdolvand, and J. C. Travers, "Hollow-core photonic crystal fibres for gas-based nonlinear optics," *Nat. Photonics* **8**, 278–286 (2014).
101. M. R. Abu Hassan, F. Yu, W. J. Wadsworth, and J. C. Knight, "Cavity-based mid-IR fiber gas laser pumped by a diode laser," *Optica* **3**, 218 (2016).
102. F. Benabid, J. C. Knight, G. Antonopoulos, and P. S. J. Russell, "Stimulated Raman scattering in hydrogen-filled hollow-core photonic crystal fiber.," *Science* **298**, 399–402 (2002).
103. F. Couny, F. Benabid, and P. S. Light, "Large-pitch kagome-structured hollow-core photonic crystal fiber," *Opt. Lett.* **31**, 3574 (2006).
104. C. M. Smith, N. Venkataraman, M. T. Gallagher, D. Müller, J. A. West, N. F. Borrelli, D. C. Allan, and K. W. Koch, "Low-loss hollow-core silica/air photonic bandgap fibre.," *Nature* **424**, 657–9 (2003).
105. A. D. Pryamikov, A. S. Biriukov, A. F. Kosolapov, V. G. Plotnichenko, S. L. Semjonov, and E. M. Dianov, "Demonstration of a waveguide regime for a silica hollow--core microstructured optical fiber with a negative curvature of the core boundary in the spectral region  $> 3.5 \mu\text{m}$ ., " *Opt. Express* **19**, 1441–8 (2011).
106. Y. Y. Wang, N. V Wheeler, F. Couny, P. J. Roberts, and F. Benabid, "Low loss broadband transmission in hypocycloid-core Kagome hollow-core photonic crystal fiber.," *Opt. Lett.* **36**, 669–71 (2011).
107. R. Amezcua-Correa, N. G. R. Broderick, M. N. Petrovich, F. Poletti, and D. J. Richardson, "Optimizing the usable bandwidth and loss through core design in realistic hollow-core photonic bandgap fibers," *Opt. Express* **14**, 7974 (2006).
108. M. S. Habib, O. Bang, and M. Bache, "Low-loss single-mode hollow-core fiber with anisotropic anti-resonant elements.," *Opt. Express* **24**, 8429–36 (2016).
109. F. Poletti, N. V. Wheeler, M. N. Petrovich, N. Baddela, E. Numkam Fokoua, J. R. Hayes, D. R. Gray, Z. Li, R. Slavík, and D. J. Richardson, "Towards high-capacity fibre-optic communications at the speed of light in vacuum," *Nat. Photonics* **7**, 279–284 (2013).
110. P. J. Roberts, F. Couny, H. Sabert, B. J. Mangan, D. P. Williams, L. Farr, M. W. Mason, A. Tomlinson, T. A. Birks, J. C. Knight, and P. S. J. Russell, "Ultimate low loss of hollow-core photonic crystal fibres," *Opt. Express* **13**, 236 (2005).
111. J. W. Nicholson, A. D. Yablon, S. Ramachandran, and S. Ghalmi, "Spatially and spectrally resolved imaging of modal content in large-mode-area fibers," *Opt. Express* **16**, 7233 (2008).

112. C. Jollivet, D. Flamm, M. Duparré, and A. Schülzgen, "Detailed Characterization of Optical Fibers by Combining  $S^2$  Imaging With Correlation Filter Mode Analysis," *J. Light. Technol.* **32**, 1068–1074 (2014).
113. J. W. Nicholson, A. D. Yablon, J. M. Fini, and M. D. Mermelstein, "Measuring the Modal Content of Large-Mode-Area Fibers," *IEEE J. Sel. Top. Quantum Electron.* **15**, 61–70 (2009).
114. J. Bromage, J. M. Fini, C. Dorrer, and J. D. Zuegel, "Characterization and optimization of Yb-doped photonic-crystal fiber rod amplifiers using spatially resolved spectral interferometry.," *Appl. Opt.* **50**, 2001–7 (2011).
115. F. Kong, K. Saitoh, D. Mcclane, T. Hawkins, P. Foy, G. Gu, and L. Dong, "Mode area scaling with all-solid photonic bandgap fibers.," *Opt. Express* **20**, 26363–72 (2012).
116. C. Jollivet, B. Samson, L. Leick, L. Shah, M. Richardson, and A. Schülzgen, "Comparative study of light propagation and single-mode operation in large-mode area fibers designed for 2- $\mu$ m laser applications," *Opt. Eng.* **54**, 011006 (2014).
117. H.-J. Otto, F. Jansen, F. Stutzki, C. Jauregui, J. Limpert, and A. Tunnermann, "Improved Modal Reconstruction for Spatially and Spectrally Resolved Imaging (S2)," *J. Light. Technol.* **31**, 1295–1299 (2013).
118. C. Wei, R. A. Kuis, F. Chenard, C. R. Menyuk, and J. Hu, "Higher-order mode suppression in chalcogenide negative curvature fibers.," *Opt. Express* **23**, 15824–32 (2015).